

© 2021 Kenneth E Swartz

TOPOLOGY OPTIMIZATION OF MANUFACTURABLE PHOTONIC CRYSTALS WITH
COMPLETE BANDGAPS

BY

KENNETH E SWARTZ

DISSERTATION

Submitted in partial fulfillment of the requirements
for the degree of Doctor of Philosophy in Mechanical Engineering
in the Graduate College of the
University of Illinois Urbana-Champaign, 2021

Urbana, Illinois

Doctoral Committee:

Professor Daniel Tortorelli, Chair
Assistant Professor Kai James, Director of Research
Professor Jianming Jin
Assistant Professor Kathryn Matlack
Dr. Daniel White, Lawrence Livermore National Laboratory

ABSTRACT

Periodic structures consisting of dielectric material, i.e. photonic crystals, are capable of prohibiting the transmission of electromagnetic waves within frequency ranges referred to as bandgaps. This principle was first demonstrated with alternating slabs of material and later demonstrated with three-dimensional (3D) structures capable of reflecting waves from any incident angle. A number of potential applications for photonic bandgap structures exist, including waveguides, integrated circuits, fiber optics, and photonic cavities. Additionally, many other optical devices could benefit from the perfect-mirror behavior of photonic crystals.

The design of photonic crystals for complete bandgap has challenged researchers for the past three decades. Bandgap structures are often quite complicated and therefore difficult to design heuristically. Thus, the application of automated design tools, such as topology or shape optimization, is very attractive. Unfortunately, bandgap analysis is very computationally intensive, and it is difficult to employ effective low-dimensional design parameterizations capable of generating bandgap structures. Until recently, computational power was insufficient to design 3D structures with complete bandgaps. The development of computing clusters has reduced this burden significantly, although computational cost remains a challenge.

A major obstacle when numerically designing for bandgap, or any other design metric derived from eigenvalues, is the presence of degenerate eigenmodes. Optimal bandgap structures often possess many planes of symmetry; this is helpful to reduce the overall cost of the required dispersion analysis, but it often leads to wave frequencies that have multiple propagation directions, the physical result of degenerate eigenmodes. Herein lies the challenge; we would like to use gradient-based optimization algorithms to design bandgap structures, but the presence of degenerate eigenmodes renders our design metric non-smooth. Solving this conundrum by leveraging symmetric polynomials was a major contribution of this work. Further, an efficient sensitivity analysis and a successive mesh refinement strategy were developed to augment the design framework.

Finally, it was observed that bandgap structures often exhibit poor stiffness properties, sometimes even making the structures unable to be physically realized. A series of physics-based, nonlinear constraints were developed to ensure the algorithmically-generated structures are manufacturable. These constraints were demonstrated by designing a series of photonic crystals that were fully self-supporting without the presence of enclosed void space. Additionally, the trade-off between bandgap and bulk stiffness was investigated. The proposed design framework is the first of its kind; a technique able to leverage traditional, gradient-based nonlinear programming solvers to generate 3D bandgap structures with manufacturing constraints.

ACKNOWLEDGEMENTS

First and foremost I must thank my parents for their unwavering support throughout my life. They encouraged me in all of my endeavors, be it athletics, academics, or travel & hobbies. They pushed me to pursue education from the beginning, and so it goes without saying that I wouldn't be writing this dissertation if it weren't for the values they imposed on me. Most importantly, they taught me to always apply myself and instilled in me the discipline to lead a successful life.

I had a number of great teachers throughout elementary, middle, and high school, however, it was Mr. Richard Bazyn who most influenced my decision to pursue engineering. His high school calculus and physics classes prepared me for the rigors of UIUC as well as, if not better than, my peers who attended top-notch college-prep schools in Chicago. His teaching expertise of these subjects served me well throughout my undergraduate engineering studies.

My first research mentor, Lance Hibbeler, was instrumental in my decision to pursue graduate studies. He taught me the proper way to perform research and I find his lessons useful to this day.

My Master's advisor, Armand Beaudoin, was a catalyst in transforming me from a student to an independent researcher. He pushed me out of my comfort zone and taught me the skills to become self sufficient. In fact, his career advice and recommendation to take a design optimization class at UIUC with Dan Tortorelli and Kai James heavily influenced my decision to pursue a PhD.

Kai James has been an excellent teacher and research advisor throughout my graduate studies. He taught my first course on design optimization, and I subsequently served as TA for the course for two semesters under his direction. I learned much about design optimization from Kai, and it was truly a privilege to work for an advisor who was so invested in the success of his students.

Dan Tortorelli has considerably influenced my engineering career. He taught me three courses at UIUC, and has served as a research advisor throughout my PhD. He offered exceptional training in advanced mathematics and design optimization and pushed me to advance my skill set by learning electromagnetics and parallel computing. Moreover, he offered me the opportunity to collaborate with LLNL which has supplied me with incredible resources and spurred me to move across the country and start an exciting life in California.

Dan White served as my graduate fellowship advisor for the last two years. He was an excellent mentor, both technically and professionally, as I acclimated to working with LLNL. His technical expertise in electromagnetics and finite elements paired with his long and successful career at LLNL provided me with an excellent resource for advice.

Seth Watts has been an excellent mentor during my time collaborating with LLNL. He often has very pertinent advice since he also started graduate school at UIUC before working with LLNL.

TABLE OF CONTENTS

LIST OF FIGURES	v
LIST OF TABLES	vi
CHAPTER 1: INTRODUCTION	1
1.1 Design of photonic bandgap structures	3
1.2 Manufacturing and stiffness constraints for photonic crystals	5
CHAPTER 2: TOPOLOGY OPTIMIZATION FOR PHOTONIC BANDGAP	8
2.1 Formulation	8
2.2 Results and discussion	26
2.3 Conclusions	34
CHAPTER 3: MANUFACTURING AND STIFFNESS CONSTRAINTS FOR TOPOLOGY OPTIMIZED PERIODIC STRUCTURES	35
3.1 Constraint formulations	35
3.2 Constraint capability comparison	51
3.3 Optimization test problem	54
3.4 Photonic crystal design with manufacturing constraints	61
3.5 Photonic bandgap design with tunable bulk modulus	65
3.6 Conclusions	69
CHAPTER 4: ADDITIVE MANUFACTURING OF BANDGAP STRUCTURES	70
4.1 Photonic bandgap validation	70
4.2 Testing additive manufacturing constraints	75
CHAPTER 5: CONCLUSIONS	83
5.1 Future work	86
REFERENCES	88

LIST OF FIGURES

2.1	Irreducible Brillouin zones of unit cells with orthorhombic symmetry	13
2.2	Representative dispersion plot for 2D $\kappa \in \partial\mathcal{B}$	14
2.3	Example 2D design parameterization with orthorhombic symmetry	16
2.4	Cone filter kernel in 2D at various locations	17
2.5	Uniformly refined unit cells	25
2.6	Nested mesh refinement for complete 2D bandgap	28
2.7	Post-processed photonic crystal with complete 2D bandgap between modes 5-6	28
2.8	Photonic crystal with complete 3D bandgap between modes 2-3	31
2.9	Photonic crystal with complete 3D bandgap between modes 5-6	32
2.10	Photonic crystal with complete 3D bandgap between modes 6-7	33
3.1	A comparison of volume fraction interpolations	37
3.2	Example behavior when a single unit cell is analyzed with VTM	40
3.3	Example behavior when a 2^2 unit cell array is analyzed with VTM	40
3.4	Locations of essential boundary conditions when computing θ_{swc}	45
3.5	Example unit cells for constraint evaluation comparison	51
3.6	Optimal $\tilde{\nu}$ solutions for θ_{EVS}	55
3.7	Optimal $\tilde{\nu}$ solutions for θ_{EVS} with θ_{vtv} constraint	56
3.8	Optimal $\tilde{\nu}$ solutions for θ_{ISM}	56
3.9	Optimal $\tilde{\nu}$ solutions for θ_{ISM} with θ_{vts} constraint	57
3.10	Optimal $\tilde{\nu}$ solutions for θ_{ISM} with θ_{eig} constraint	58
3.11	Optimal $\tilde{\nu}$ solutions for θ_{ISM} with θ_{swc} constraint	58
3.12	Optimal $\tilde{\nu}$ solutions for θ_{ISM} with θ_{κ} constraint	59
3.13	Optimal $\tilde{\nu}$ solutions for θ_{ISM} with θ_{γ} constraint	59
3.14	Optimal $\tilde{\nu}$ solutions for θ_{ISM} with θ_{κ} ($\mu_{\kappa}=0.01$) and A^U constraints	60
3.15	Optimal $\tilde{\nu}$ solutions for θ_{ISM} with θ_{κ} ($\mu_{\kappa}=0.01$) and A^L constraints	60
3.16	Optimal $\tilde{\nu}$ solutions for θ_{ISM} with θ_{κ} ($\mu_{\kappa}=0.01$) and A^D constraints	61
3.17	Applying θ_{vtv} constraint to remove EVS from mode 5-6 bandgap structure	62
3.18	Applying θ_{vtv} constraint to remove EVS from mode 6-7 bandgap structure	63
3.19	Applying various constraints to remove ISM	64

3.20	Applying various constraints to ensure structures are self-supporting	65
3.21	Applying κ and VTM constraints to ensure structures are manufacturable	66
3.22	Applying γ and VTM constraints to ensure structures are manufacturable	67
3.23	2D Bandgap-midgap ratio θ_ω vs. bulk modulus κ	68
3.24	3D Bandgap-midgap ratio θ_ω vs. bulk modulus κ	68
4.1	Relationship between unit cell size and electromagnetic frequency	71
4.2	Frequency vs. unit cell size	72
4.3	3D printing preview of photonic crystal	72
4.4	Failed attempt at 3D printing photonic crystals	73
4.5	Performance of structure from Figure 2.9 vs. ϵ_r of base material	74
4.6	Applying θ_{viv} constraint to remove EVS from mode 6-7 bandgap structure	75
4.7	.stl files used for 3D printing	76
4.8	Successful 3D bandgap prototype printed with FormLabs SLA machine	77
4.9	FDM 3D Printer	78
4.10	Failed 3D bandgap prototype printed with FDM machine	78
4.11	Software preview of bandgap designs	79
4.12	Bed of copper powder	80
4.13	Example binder application layer	80
4.14	Removing loose powder with vacuum	81
4.15	Snapshots of powder removal post-processing	81
4.16	Removing powder with pressurized air	82

LIST OF TABLES

2.1	Numerical Parameters	27
2.2	Summary of complete 2D bandgap optimizations (gaps 1-4)	29
2.3	Summary of complete 2D bandgap optimizations (gaps 5-8)	30
3.1	Constraint Evaluations	52

CHAPTER 1: INTRODUCTION

The engineering design process has long been hindered by the arduous process of trial and error. Designs are first conceived, then they are tested, and finally a decision is made about whether or not the design will suffice for the task at hand. If the design is deemed unsuitable, then the designer re-enters this time consuming loop by suggesting possible alterations before a new candidate structure is considered. The techniques for improving designs are best described as guidelines, and in reality most ideas stem from intuition and designer experience. Unfortunately, it is difficult to teach these concepts, and so it is difficult to train novice design engineers how to most efficiently arrive at suitable structures for the myriad of applications modern engineers face.

Engineers have become much more proficient at generating effective designs with the advent of computers. Rather than time consuming and costly experiments, computer simulations rapidly speed up the design testing procedure. The trial and error process has been considerably accelerated, but the underlying problem remains; hard and fast rules for how to improve designs are scarce. Herein lies the potential for structural optimization to shift the paradigm of the engineering design process. Algorithms can be developed to remove design decisions from the human designer, which allow structures to be improved towards a mathematically provable best design.

Once the process of testing out candidate designs entered the digital world, it was only a matter of time before the design process became fully automated. While we have not achieved this yet, it seems to be the way of the future. Engineers in the future will only prescribe how they wish a structure to perform, rather than explicitly prescribing the geometry and/or material selection of the design. Algorithms will handle the burden of selecting designs in ways that surpass the capability of human brains. The resulting structures will in some cases astonish us with their ingenious use of space, yet in some cases they will leave us unsurprised as we rediscover concepts that nature has presented us with long ago. In either situation, the world we create around ourselves will begin rapidly changing as we adopt automated design principles.

Structural optimization started as a simple process of optimizing a set of parameters that dictated the size of predetermined features in a design. For example, a truss structure with a set geometry could be optimized by selecting the radius of each member to maximize the overall stiffness of the structure. While this technique is quite powerful, the designs are limited by the initial geometry selection. On the contrary, topology optimization is able to produce nearly any possible structure with a sufficiently refined design parameterization. This technique has been intensely studied since it was proposed just over 30 years ago, and it will be the topic of this work. For completeness, I will mention that shape optimization is also a very relevant design technique that is able to place a material interface in the optimal location. Although shape optimization is a powerful tool with many applications, especially where boundary location is imperative for simulation accuracy, it will not be discussed further here since this work exclusively utilizes topology optimization.

Topology optimization uses a very simple principle to define engineering structures. A list of parameters indicates whether or not material exists at a discrete set of locations within a design domain. These parameters are varied until the optimization algorithm can determine a set of indicators that cannot be improved by local perturbations to the design state. Once this is achieved, the structure is explicitly defined by each indicator, denoting the presence or lack of material at that spatial location. While simple in theory, this process has proven itself to be extremely powerful in practice. Initially, most topology optimization problems aimed to design the stiffest or lightest structure, subject to external loads under linear elastic assumptions. In reality, however, we know that engineers face much more complicated design problems with more demanding design requirements and simulation necessities. Thus, to continue advancing the engineering practice towards a fully-automated design process we must further our topology optimization capabilities. To this end, a framework is proposed that is capable of designing periodic structures such that they totally reflect light waves within specified frequency ranges. This ability will empower a new generation of tools in the optics engineering field. Further, a series of design constraints are formulated to ensure these periodic structures are practical; namely, that they are fully self-supporting and manufacturable with modern additive manufacturing techniques.

1.1 Design of photonic bandgap structures

Photonic bandgap structures forbid electromagnetic wave propagation of a given frequency range, also known as the bandgap [1]. The first photonic bandgap structures were one-dimensional periodic structures [2], however, the bandgap engineering field progressed little until higher-dimensional bandgap structures were discovered a century later [3, 4]. Early experiments demonstrated 3D photonic bandgaps in crystals made of dielectric spheres with face-centered cubic [5] and body-centered cubic [6] symmetries, as well as in crystals made of dielectric rods [7]. Additionally, a diamond structure of dielectric spheres was designed and its complete 3D photonic bandgap was numerically simulated [8]. Since these groundbreaking results, three decades of research has followed on the design and analysis of photonic bandgap structures. Novel applications include low-loss waveguides [9, 10, 11, 12], integrated circuits [13], perfect mirrors [14], photonic cavities [11, 15], photonic bandgap fibers [16], and a number of other exciting optical applications [1].

A material made of a periodic, architected micro-structure is referred to as a “metamaterial”. The bulk, or effective, material properties of metamaterials are controlled by the underlying material properties, but also and more interestingly, by the geometry of the microstructure. A technique known as homogenization was developed to predict the effective elastic properties of metamaterials by analyzing just a single unit cell [17]. Further, topology optimization [18, 19], which seeks to determine the optimal material distribution for a specific task, is readily applied to solve the inverse homogenization problem [20, 21], i.e. to generate micro-structures that exhibit optimal, or prescribed, effective properties. Seemingly impossible effective material properties have been observed by optimizing metamaterials, such as simultaneous negative bulk modulus and mass density [22] as well as negative Poisson’s ratio [23].

Metamaterials have also been designed for effective electromagnetic properties, such as magnetic permeability and electric permittivity, although much less research has been performed in this realm. So called “left-handed” metamaterials have been designed to exhibit negative effective permeability and permittivity [24]. These electromagnetic metamaterials are periodic structures that

exhibit their effective bulk properties at an operating frequency with a corresponding wavelength that is much larger than the unit cell size [25]. Photonic crystals are similarly periodic structures, however, they obtain their performance by leveraging diffraction [25] and are therefore designed to operate at frequencies with a wavelength that is similar in size to the unit cell. Numerical inverse design, referred to as inverse homogenization via topology optimization, is readily applied to design the periodic unit cells of both metamaterials and photonic crystals.

Many previous studies have applied inverse problem techniques to the design of photonic crystals [26]. A major issue plaguing numerical design of photonic bandgap structures is the non-smoothness of the objective function due to degenerate eigenvalues [27]. The first successful 3D bandgap design optimization naturally avoided eigenvalue degeneracy by using a very low-dimensional design space [28], however, a number of techniques have since been employed to circumvent this issue. 2D photonic crystals exhibiting bandgaps were designed using a generalized gradient ascent [29, 30] algorithm that leveraged directional derivatives, or subgradients, computed by the generalized gradient technique for degenerate eigenvalues [31]. The generalized gradient ascent was later extended to a level-set design parameterization [32], and similarly a regularized descent method was used to design optical waveguides via shape optimization [33]. Alternatively, semidefinite programming, which alleviates the need for eigenvalue sensitivities, was applied to design 2D photonic crystals [34] and further extended to the robust design of 3D photonic crystals to accommodate uncertainties in fabrication [35]. Topology optimization, i.e. inverse unit cell design, has also been used to design structures with mechanical, or phononic, bandgaps [36], and even more interestingly with both phononic *and* photonic bandgaps [37]. Genetic [38] and evolutionary [39] topology optimization methods have also been applied to design photonic crystals. These techniques do not require design sensitivities, but do require many more iterations to converge than gradient based-algorithms and they cannot ensure optimality. For these reasons, gradient-free algorithms are not recommended for solving topology optimization problems [40]. At the other extreme, theoretical techniques for bandgap design that do not require iterative techniques were developed [41, 42]. Interested readers are directed to review articles [43, 44].

The numerical techniques described in this work are only applicable to non-magnetic materials, and therefore we direct readers to [45, 46, 47, 48, 49] for studies on magnetic photonic crystals. Design optimization has not yet been applied to 3D magnetic photonic crystals. Further, we assume lossless materials and direct readers to in [1, 50, 51] for information on lossy photonic structures.

This work alleviates the differentiability issues of repeated eigenvalues by leveraging research on symmetry polynomials of eigenvalues [52]. The presented smoothing technique allows photonic crystal design via traditional gradient-based nonlinear programming (NLP) solvers. The use of a smooth NLP algorithm is advantageous, because although non-smooth NLP algorithms [53] could be used in principle, their success has not been demonstrated on photonic crystal design in practice. Our work also uses a 3D design parameterization, which is necessary to generate structures with complete 3D bandgaps; it also proved very effective for optimizing structures with large complete 2D bandgaps. We also improved the computational efficiency of a “voxel” based design parameterization by using a nested mesh refinement technique. Length-scale control is implemented to ensure manufacturability by employing a periodic volume fraction filter that respects the orthorhombic symmetry of our unit cell. Multi-level parallelism and an efficient sensitivity analysis are exploited to execute these large computational tasks in a reasonable wall clock time. We validate our framework by designing novel structures with complete 2D and 3D bandgaps.

1.2 Manufacturing and stiffness constraints for photonic crystals

The design of periodic unit cells with inverse homogenization [20] using topology optimization [18] has been widely studied. For example, it is used to design metamaterials with seemingly nonphysical effective properties, such as negative Poisson’s ratio [54, 55, 56] and simultaneous negative bulk modulus and mass density [22]. Inverse homogenization is also used to tune metamaterials to match prescribed properties [57] and to obtain theoretically optimal properties [58]. The method is becoming more common in three dimensions (3D) [56] as computing power continues to advance, and the interest in lattice materials continues to increase [59]. Moreover it is not limited to the realm of mechanics; designs for thermal expansion [60], thermal conductivity [61],

fluid permeability [62], and magnetic permeability [63] have also been generated, and multifunctional designs are becoming increasingly popular [61, 64]. Interested readers are directed to an exhaustive review of micro-architected design [21].

As mentioned above, topology optimization has been used to design the periodic unit cells of phononic and photonic crystals [65]. Early studies designed two-dimensional (2D) phononic [36] and photonic crystals [32, 34], and more recently 3D photonic crystals [35, 39]. Bandgap optimizations present an obvious need for material connectivity constraints. Indeed in stiffness optimizations, disconnected regions of material never appear as they increase mass but not stiffness. However, in bandgap optimization problems it has been demonstrated that disconnected structures are often beneficial [32, 34]. Such designs with islands of solid material (ISM) are problematic as they cannot be manufactured since they are not self-supporting. Additionally, enclosed void space (EVS), also common to bandgap optimized designs [35], cannot be easily manufactured.

Many design formulations have been presented to ensure manufacturability in density-based topology optimization [66, 67]. For example, techniques have been proposed to limit the overhang angle of a structure to alleviate the need for support material in additive manufacturing (AM) [68, 69, 70, 71, 72, 73]. Additionally, the virtual temperature method (VTM) [74] prevents EVS which is difficult to manufacture with most AM processes. We present various constraints that can be integrated into topology optimization frameworks to ensure that optimal microstructures are without ISM and EVS. Our techniques do not require changing the design parameterization or applying a filter. Further, several of them are inherently linked to mechanical stiffness so we will investigate the effect of adding stiffness requirements to photonic bandgap structures. We will thus be able to generate manufacturable photonic crystal structures with prescribed levels of stiffness and probe the trade-off between these two often conflicting objectives.

In Chapter 3 we extend the VTM [74] to prevent ISM by flipping the material properties in Section 3.1.1. Then, we further extend the VTM to eliminate both EVS and ISM from periodic structures in Section 3.1.1. We alternatively prevent ISM by enforcing a mechanical eigenvalue constraint described in Section 3.1.2 and ensure self-supporting structures by enforcing a

self-weight compliance constraint described in Section 3.1.3. Finally, we compute the homogenized [17], or effective, constitutive tensor of our unit cells from which we derive bulk stiffness, shear stiffness, and isotropy constraints in Section 3.1.4. The proposed constraints are evaluated on a series of contrived unit cells to demonstrate their behavior in Section 3.2, where guidelines for the appropriate constraint choices are presented to meet particular design goals. A simple optimization test problem is presented to display the efficacy of each constraint for unit cell design in Section 3.3, and designs of self-supporting, manufacturable photonic crystals further serve to exemplify the proposed constraints in Section 3.4. Finally, novel 3D photonic bandgap structures with prescribed minimum bulk stiffness levels are presented to illustrate a feasible bandgap-bulk stiffness design space in Section 3.5.

CHAPTER 2: TOPOLOGY OPTIMIZATION FOR PHOTONIC BANDGAP

This chapter describes a framework for designing photonic crystals via topology optimization. Only design performance with respect to bandgap is considered here, i.e. manufacturability constraints are left to Chapter 3. The framework describes techniques to alleviate the non-smoothness caused by degenerate eigenvalues, while also providing an efficient sensitivity analysis and mesh refinement technique to significantly reduce the computational burden. The traditional “density” method of topology optimization is used to ensure adequate design freedom to obtain complete bandgaps. Confidence in the proposed method was gained by reproducing previously published bandgap structures. Further, novel bandgap structures were generated using the new techniques. Orthorhombic symmetry is considered throughout, although the techniques easily generalize to other symmetry groups. A key aspect of the proposed framework is the ability to leverage traditional gradient-based nonlinear programming solvers. This advantage will be highlighted in Chapter 3, where constraints are used to improve the designs presented in Chapter 2 by ensuring they are manufacturable. The work presented in this chapter has been published in *Optics Express* [75].

2.1 Formulation

The techniques used to generate the results in Section 2.2 are described in detail here. The governing equations, solution basis, objective formulation, design parameterization, sensitivity analysis, filtering technique, and mesh refinement strategy are all described thoroughly with appropriate references presented for further study, if desired. Note that specific values which would be required to reproduce the results are given near their corresponding results in Section 2.2.

2.1.1 Maxwell's eigenvalue problem

Time-harmonic electromagnetism in a source-free, isotropic, lossless medium is governed by the four Maxwell equations [1, 76]

$$\nabla \times \mathbf{E}(\mathbf{x}) = i\omega\mu_0\mu_r(\mathbf{x}) \mathbf{H}(\mathbf{x}) \quad (2.1)$$

$$\nabla \times \mathbf{H}(\mathbf{x}) = -i\omega\varepsilon_0\varepsilon_r(\mathbf{x}) \mathbf{E}(\mathbf{x}) \quad (2.2)$$

$$\nabla \cdot (\varepsilon_r(\mathbf{x}) \mathbf{E}(\mathbf{x})) = 0 \quad (2.3)$$

$$\nabla \cdot (\mu_r(\mathbf{x}) \mathbf{H}(\mathbf{x})) = 0, \quad (2.4)$$

where $\nabla \times$ and $\nabla \cdot$ are the curl and divergence operators with respect to position \mathbf{x} , respectively, \mathbf{E} is the electric field, \mathbf{H} is the magnetic field, ω is the frequency, μ_0 is the magnetic permeability in a vacuum, μ_r is the relative magnetic permeability, ε_0 is the electric permittivity in a vacuum, ε_r is the relative electric permittivity, and i is the imaginary unit. Bold-faced font will be used to denote vector entities throughout. This paper will focus on non-magnetic materials, i.e. $\mu_r(\mathbf{x}) = 1$, and therefore we omit $\mu_r(\mathbf{x})$ hereafter. Equations (2.1) and (2.2) are easily combined into

$$\nabla \times \left(\frac{1}{\varepsilon_r(\mathbf{x})} \nabla \times \mathbf{H}(\mathbf{x}) \right) = \left(\frac{\omega}{c} \right)^2 \mathbf{H}(\mathbf{x}), \quad (2.5)$$

where it is noted that the speed of light $c = \frac{1}{\mu_0\varepsilon_0}$ was substituted, and we reiterate that our media are assumed to be lossless and therefore ε_r is strictly real. Further, since we are assuming isotropic media we express the permittivity as a scalar quantity, although the solution technique easily generalizes to anisotropic media wherein the permittivity is tensor-valued and thus $\frac{1}{\varepsilon_r(\mathbf{x})}$ becomes ε_r^{-1} . Equation (2.5) is an ordinary eigenvalue problem with eigenpairs $\left(\left(\frac{\omega}{c} \right)^2, \mathbf{H} \right)$, however, it is impor-

tant to remember that solutions to Equation (2.5) must also satisfy Equations (2.3) and (2.4) to be physically valid. A similar eigenvalue problem for the electric field \mathbf{E} could have been formulated, although a generalized eigenvalue problem would have been obtained. The choice of solution field, i.e. \mathbf{H} or \mathbf{E} , is further discussed in Sec. 2.1.2

Bloch's theorem [77, 78] allows the magnetic field in a periodic medium to be expressed over a single unit cell as

$$\mathbf{H}(\mathbf{x}) = \mathbf{H}_p(\mathbf{x}) e^{i\boldsymbol{\kappa}\cdot\mathbf{x}}, \quad (2.6)$$

where \mathbf{H}_p is a periodic function with the same periodicity as the medium and $\boldsymbol{\kappa}$ is a wave vector. Substituting Equation (2.6) into Equation (2.5) yields the ordinary eigenvalue problem

$$\mathbf{A}_{\boldsymbol{\kappa}}\mathbf{H}_p(\mathbf{x}) = (\nabla + i\boldsymbol{\kappa}) \times \frac{1}{\varepsilon_r(\mathbf{x})} (\nabla + i\boldsymbol{\kappa}) \times \mathbf{H}_p(\mathbf{x}) = \left(\frac{\omega}{c}\right)^2 \mathbf{H}_p(\mathbf{x}), \quad (2.7)$$

which is solved over a single unit cell for the pair $\left(\left(\frac{\omega}{c}\right)^2, \mathbf{H}_p\right)$. From Equations (2.6) and (2.7) we see that \mathbf{H} is a wave that propagates with frequency ω in the direction $\boldsymbol{\kappa}$. In bandgap structures there exists intervals $[\omega_1, \omega_2]$, i.e. bandgaps, in which no waves propagate.

2.1.2 Planewave expansion

A finite dimensional basis is used to approximate \mathbf{H} and solve Equation (2.7) numerically. There are a number of possible bases, each with their own advantages and limitations [79]. Perhaps the most common basis in numerical methods is a finite element basis [80], which has the advantage of easily enforcing the required solution continuity through the use of vector finite elements, e.g. H-curl finite elements enforce tangential vector continuity [81]. Due to their immense applicability and popularity across many disciplines, open source finite element codes are widely available, such as the modular finite element methods (MFEM) library [82]. The main disadvantage of a finite element basis is the difficulty of enforcing the transversality requirements [79]. As mentioned in Sec. 2.1.1, all computed solutions of Equation (2.7) must also satisfy Equations (2.3) and (2.4) to be physically valid. Solving Equation (2.7) numerically without a transversality constraint will yield

many zero-valued eigenvalues [79] which do not satisfy Equations (2.3) and (2.4), These spurious solutions could be removed after the calculation, but this technique would be quite computationally wasteful. A much better choice is the use of a planewave basis, which has become the standard practice for photonic band analyses since it was first presented two decades ago [79].

A planewave basis is used to approximate \mathbf{H}_p as

$$\mathbf{H}_p(\mathbf{x}) = \sum_{m=1}^N \mathbf{h}_m e^{i\mathbf{G}_m \cdot \mathbf{x}} \quad (2.8)$$

where \mathbf{G}_m are the reciprocal lattice vectors of the unit cell and \mathbf{h}_m are the unknown degrees of freedom (DOF) in wavevector space [79]. Substituting Equation (2.8) into Equation (2.6) and inspecting the resulting Equation (2.4) reveals a major advantage of the planewave basis. We see that the transversality requirement reduces to

$$\nabla \cdot \left(\sum_{m=1}^N \mathbf{h}_m e^{i(\mathbf{G}_m + \boldsymbol{\kappa}) \cdot \mathbf{x}} \right) = 0, \quad (2.9)$$

which further reduces to

$$\mathbf{h}_m \cdot (\mathbf{G}_m + \boldsymbol{\kappa}) = 0. \quad (2.10)$$

Since $\mathbf{G}_m + \boldsymbol{\kappa}$ is known, the above Equation (2.10) constraint on \mathbf{h}_m is easily enforced by expressing

$$\mathbf{h}_m = h_m^1 \mathbf{e}_1 + h_m^2 \mathbf{e}_2 \quad (2.11)$$

where \mathbf{e}_1 and \mathbf{e}_2 are orthogonal unit vectors that are perpendicular to $\mathbf{G}_m + \boldsymbol{\kappa}$, and solving for the unknown DOF h_m^1 and h_m^2 . The transversality constraint would not be so easily enforced had Equation (2.5) been formulated for the electric field \mathbf{E} , due to the presence of $\boldsymbol{\epsilon}_r(\mathbf{x})$ in Equation (2.3). By choosing \mathbf{H} as the solution field, satisfying $\nabla \cdot \mathbf{H}(\mathbf{x}) = 0$ effectively satisfies Equation (2.4), since $\mu_r(\mathbf{x}) = 1$, and Equation (2.3) will automatically be satisfied by expressing \mathbf{h}_m via Equation (2.11) [79].

Bandgap optimizations only require calculation of a few of the lowest modes, and thus for large

problems an iterative eigenvalue solver is significantly more efficient than a direct solver. Fortunately, the linear operator in Equation (2.7) is symmetric positive-definite [1], and as such iterative methods, e.g. locally optimal block preconditioned conjugate gradient (LOBPCG) [83], may be used. A key feature of iterative methods is that they only require matrix-vector products, rather than explicit matrices. In other words, the linear operator of Equation (2.7) is never computed and stored, only its action on vectors is required. To further hasten calculations, the dimension of the basis N , and therefore the cutoff magnitude of G_m , is selected such that a discrete Fourier transform (DFT) can be used to transform between planewave and spatial representations [79]. This does of course restrict the lattice unit cells to those which can be represented by rectangular prisms, due to the uniform spatial discretization required for a DFT. Ultimately, the matrix-vector products are computed in $O(n \log n)$ time using the technique described in [79], the curl operations become cross products in wave vector space ($O(n)$) and the inverse permittivity is applied locally ($O(n)$) once a DFT ($O(n \log n)$) transforms solutions between wavevector and physical space. The limiting factor becomes the two DFTs required for every matrix-vector product, although this calculation is quite efficient using the Fastest Fourier Transform in the West (FFTW) library [84]. To further improve the computational efficiency, the calculations are parallelized; the curls computed in wavevector space are embarrassingly parallel, while the DFTs performed by FFTW are parallelized along one spatial dimension. A further advantage of the planewave basis is the availability of an accurate preconditioner [79], which is crucial for rapid convergence of LOBPCG.

An open-source planewave expansion library, Maxwell Photonic Bands (MPB), is available, although the method was implemented from scratch in this work to facilitate the design sensitivity calculations. The implementation used in this study was based on the originally presented framework [79], although permittivity smoothing was excluded. This omission eases the sensitivity calculations, and any inaccuracies incurred by it are mitigated by refining the computational grid [79], which is done in our nested mesh refinement. Further, the generalization of permittivity smoothing to handle anisotropic materials [79] was not required.

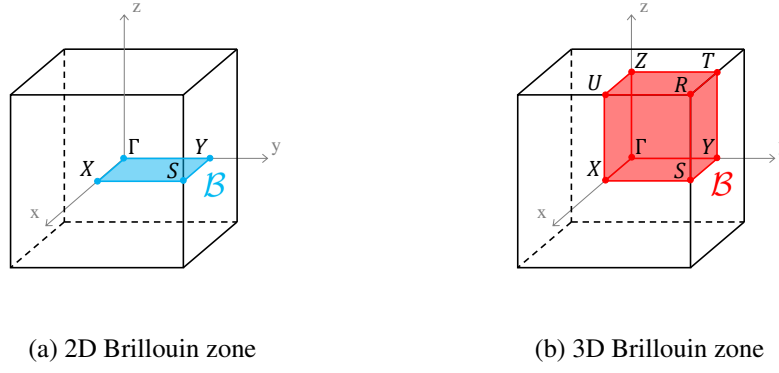


Figure 2.1 Irreducible Brillouin zones of unit cells with orthorhombic symmetry

2.1.3 Photonic bandgap calculation

To predict the presence of a complete photonic bandgap, the propagating modes must be computed from Equation (2.7) for all unique wave vectors $\boldsymbol{\kappa}$ in reciprocal lattice space [1]. Fortunately, the region of non-redundant wave vectors, i.e. the irreducible Brillouin zone (IBZ) denoted as $\mathcal{B} : \mathbb{R}^3$, is reduced for lattices possessing domain symmetries [85]. This work will consider, without loss of generality, orthorhombic crystals, due to their ease of computational implementation. \mathcal{B} is simply a square, i.e. 1/4th of the unit cell cross-section, in 2D and an octant, i.e. 1/8th of the unit cell, in 3D with orthorhombic symmetry [85], cf. Fig. 2.1. To be clear, all design parameterizations are 3D, but they will be optimized for both complete 2D bandgaps, where $\boldsymbol{\kappa}$ is restricted to lie in the $x - y$ plane, and complete 3D bandgaps where no such restriction is enforced. Note that a topology optimization scheme to overcome the difficulty of non-rectangular symmetry cells has been developed [35], although it is not needed here.

The bandgap-midgap ratio between bands m and $m + 1$ is defined as

$$\theta_\omega = \frac{\Delta\omega}{\bar{\omega}} = \frac{\min \omega_{m+1}(\boldsymbol{\kappa}) - \max \omega_m(\boldsymbol{\kappa})}{\frac{1}{2} (\min \omega_{m+1}(\boldsymbol{\kappa}) + \max \omega_m(\boldsymbol{\kappa}))} \quad \forall \boldsymbol{\kappa} \in \mathcal{B}, \quad (2.12)$$

where \mathcal{B} is the appropriate irreducible Brillouin zone for the unit cell. The bandgap-midgap ratio's scale invariance makes it preferable over the absolute bandgap $\Delta\omega$ as a performance metric [1]. Indeed, invariance ensures the lattice size of a photonic crystal may be scaled to shift the bandgap,

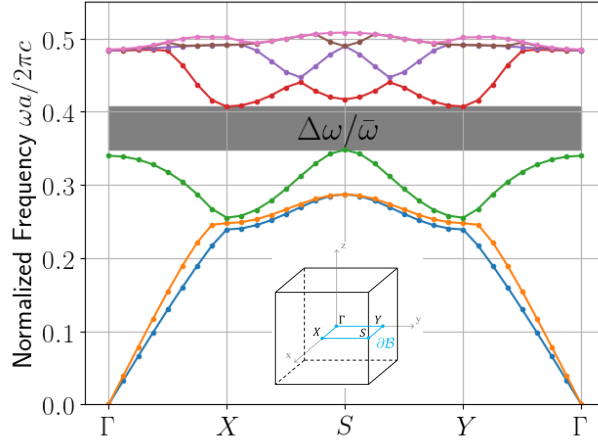


Figure 2.2 Representative dispersion plot for 2D $\kappa \in \partial\mathcal{B}$

i.e. $\bar{\omega}$, without changing θ_ω . Note that θ_ω lacks differentiability from both the min/max operations and the potential for degenerate eigenvalues. These matters are addressed in Sec. 2.1.7. Fig. 2.2 displays an example dispersion plot with a gap between modes $m = 3$ and $m + 1 = 4$, with the gray region denoting the bandgap $[\omega_1, \omega_2]$. Notice that only the edges of \mathcal{B} , denoted as $\partial\mathcal{B}$, are included in the plot, since band extrema are rarely located on the interior of \mathcal{B} [35]. A statistical analysis of band extrema location discovered that this assumption works best for crystals with high symmetry [86]. Therefore, only $\partial\mathcal{B}$ is included in our objective function calculation, but a full \mathcal{B} discretization is computed *a posteriori* to ensure our designs truly have a bandgap.

Previous work suggested that optimizing

$$\theta_\lambda = \frac{\min \lambda_{m+1}(\boldsymbol{\kappa}) - \max \lambda_m(\boldsymbol{\kappa})}{\frac{1}{2} (\min \lambda_{m+1}(\boldsymbol{\kappa}) + \max \lambda_m(\boldsymbol{\kappa}))} \quad \forall \boldsymbol{\kappa} \in \partial\mathcal{B}, \quad (2.13)$$

where $\lambda = \left(\frac{\omega}{c}\right)^2$, is equivalent to optimizing Equation (2.12) and results in better optimization performance [35]. Thus, all optimizations in this work use Equation (2.13) as the objective function, however, dispersion plots will be presented displaying the normalized frequency $\frac{\omega a}{2\pi c}$ for a unit cell of size a , as is customary. Fortunately, the eigenvalue computations at each wavevector are embarrassingly parallel, producing efficient strong scaling of the Brillouin scan. Note that the dependence of θ_λ on design variables was omitted here, but will be reconsidered in Sec. 2.1.8.

2.1.4 Topology optimization

Topology optimization distributes material in a design domain to generate optimal structures [18]. Traditionally, the structure Ω is defined by a material indicator function $\chi : \mathbb{R}^h \rightarrow \{0, 1\}$ such that $\Omega = \{\mathbf{x} \in \mathbb{R}^h \mid \chi(\mathbf{x}) = 1\}$, i.e. indicator values of $\chi(\mathbf{x}) = 1$ correspond to the presence of solid material and values of $\chi(\mathbf{x}) = 0$ correspond to void space at location \mathbf{x} . The resulting integer programming problem is ill-posed due to a lack of inherent length scale [87]. A restriction method, such as a perimeter constraint [88], provides a minimum length scale and results in a well-posed problem, but the difficulty of the integer programming formulation remains. Convexifying the design space by replacing the binary-valued material indicator with the continuous volume fraction $\nu : \mathbb{R}^h \rightarrow [0, 1]$ enables the use of efficient, gradient-based optimization algorithms, and the use of alternative restriction techniques, such as a slope constraint [89] and filtration [90]. Unfortunately, designs now contain intermediate material regions where $\nu(\mathbf{x}) \in (0, 1)$, as opposed to purely void and solid regions where $\nu(\mathbf{x}) = 0$ and $\nu(\mathbf{x}) = 1$, respectively. Often times additional measures must be taken to limit the extent of the intermediate volume fraction regions. For example, employing a material interpolation scheme [91, 92, 93] that penalizes the stiffness-to-weight ratio at locations where $\nu(x) \in (0, 1)$ in conjunction with a mass constraint [19] works well in the standard compliance topology optimization problems. Fortunately, photonic bandgap optimization problems are well-posed whence they do not require length scale control and when replacing the indicator function with the volume fraction to convexify the design space they naturally tend to binary designs, alleviating the need for material penalization schemes.

2.1.5 Design parameterization

The design variables d_i in this work are the values of the volume fraction over a set of “voxels” which discretize the unit cell, and thus the volume fraction field is piece-wise uniform. As mentioned in Sec. 2.1.3, orthorhombic symmetry will be considered throughout this work. This symmetry is enforced by allowing only the design in the symmetry cell to change freely, i.e. by allowing each voxel in the symmetry cell to have its own volume fraction. The full unit cell design

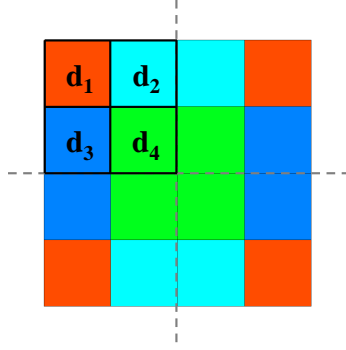


Figure 2.3 Example 2D design parameterization with orthorhombic symmetry, dashed lines mark symmetry planes

is obtained by mapping the symmetry cell design throughout the unit cell, as demonstrated by the 2D example in Fig. 2.3.

The well-known “checker-boarding” phenomenon often observed in structural topology optimization due to the inherent ill-posedness of the problem [87] is naturally avoided when optimizing bandgap structures, as evidenced by numerical results [35, 36, 38, 39] and theoretical considerations [41, 42]. Nonetheless, a filtration technique is employed here to impose a minimum length scale to ensure manufacturability and to hasten convergence of the optimization. To this end, the “cone filter” presented in [90] is extended to periodic unit cells with imposed domain symmetry. The filter works by replacing the volume fraction with a smoothed, i.e. filtered, volume fraction field $\tilde{\nu}$. In this way a highly oscillatory ν , which yields small scale features, is replaced by a smooth $\tilde{\nu}$. The cone filter uses a mesh-independent weighting of volume fraction that varies linearly with distance r such that

$$\tilde{\nu}(\mathbf{x}) = \int_{B_r(\mathbf{x})} K(\mathbf{x} - \mathbf{y}) \nu(\mathbf{y}) \, d\Omega_{\mathbf{y}} \quad (2.14)$$

where K is the linear kernel and $B_r(\mathbf{x})$ is a ball of radius r centered at \mathbf{x} . Upon discretization we obtain the discrete filtered volume fractions of the voxels \tilde{d}_i from

$$\tilde{d}_i = W_{ij} d_j, \quad (2.15)$$

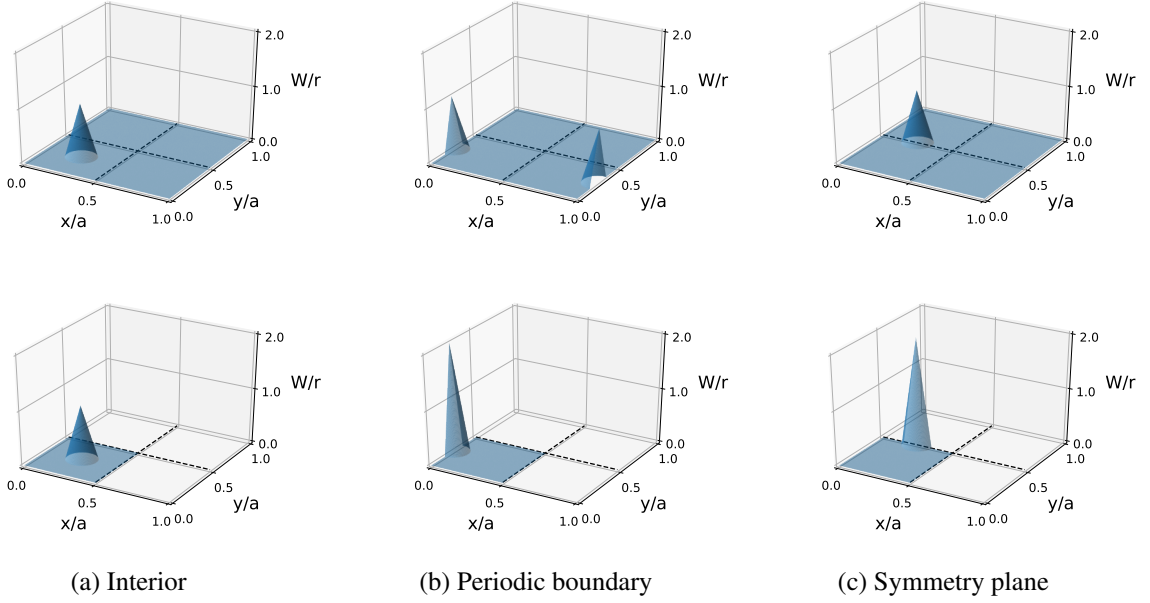


Figure 2.4 Cone filter kernel $B_r(\mathbf{x})K(\mathbf{x} - \mathbf{y})$ in 2D at various locations displayed in unit cell (top row) and symmetry cell (bottom row), dashed lines mark symmetry planes

where

$$W_{ij} = \frac{\tilde{W}_{ij}}{\sum_i \tilde{W}_{ij}}, \quad (2.16)$$

with

$$\tilde{W}_{ij} = \max(0, r - \|\mathbf{x}_i - \mathbf{x}_j\|_2), \quad (2.17)$$

in which \mathbf{x}_i is the centroid of voxel i and $\|\cdot\|_2$ is Euclidean distance. Note that the entries are “normalized” such that the sum of each row of \mathbf{W} equals 1. Extending this filter to a periodic domain is achieved by computing $\|\mathbf{x}_i - \mathbf{x}_j\|_2$ as the minimum distance between \mathbf{x}_i and all valid positions of \mathbf{x}_j in neighboring unit cells. Further, domain symmetry is accounted for by computing W_{ij} at each voxel centroid in the unit cell, and then adding all contributions to their corresponding voxel in the symmetry cell. These operations are demonstrated in 2D by Fig. 2.4 and easily generalize to 3D. Note that the symmetry operations lead to “double counting” the contribution of elements near a symmetry cell boundary. The minimum length scale is roughly enforced by the selection of r ; smaller values allow for smaller features.

2.1.6 Material interpolation

The solid phase volume fraction ν affects the design as we use a linear material interpolation scheme for the relative permittivity while solving Equation (2.7), i.e.

$$\varepsilon_r(\mathbf{x}) = \varepsilon_0 + \tilde{\nu}(\mathbf{x})(\varepsilon_1 - \varepsilon_0), \quad (2.18)$$

where $\tilde{\nu}(\mathbf{x})$ is the filtered volume fraction so that the relative permittivity $\varepsilon_r(\mathbf{x})$ is that of the solid phase ε_1 when $\tilde{\nu}(\mathbf{x}) = 1$ and that of the vacuum ε_0 when $\tilde{\nu}(\mathbf{x}) = 0$, respectively. Previous work has reported that when designing for maximal bandgaps using this interpolation, optimal structures naturally tend to binary designs, i.e. $\tilde{\nu}(\mathbf{x}) \approx 0$ or $\tilde{\nu}(\mathbf{x}) \approx 1$, in both 2D [10] and 3D [35, 39] applications, which follows intuition that high dielectric contrast leads to large bandgaps [1]. Convergence to binary structures was also observed in 2D phononic bandgap topology optimization [36]. In agreement with previous works, our optimized structures naturally converged to binary designs eliminating the need for a nonlinear material interpolation scheme.

2.1.7 Objective function smoothing

As previously mentioned, the bandgap-midgap ratio defined in Equation (2.13) lacks the differentiability required to use gradient-based optimization solvers, such as the method of moving asymptotes (MMA) [94] or interior point methods, e.g. IPOPT [95]. There are two distinct sources of non-smoothness, but fortunately both can be alleviated with the same technique. Repeated, or degenerate, eigenvalues are a well known issue plaguing eigenvalue optimization problems [27]. Consider a symmetric, matrix \mathbf{A} which depends on design variables \mathbf{d} . If \mathbf{A} has eigenpairs (λ, ϕ) which satisfy $\mathbf{A}\phi = \lambda\phi$, the simple eigenvalues λ can be differentiated with respect to a particular design parameter d_i as [27]

$$\frac{D\lambda}{Dd_i} = \frac{1}{\phi^T \phi} \phi^T \frac{\partial \mathbf{A}}{\partial d_i} \phi, \quad (2.19)$$

where D denotes a total derivative and ∂ denotes a partial derivative. It becomes clear that Equation (2.19) admits infinitely many solutions in the case of repeated eigenvalues, wherein there are an infinite number of valid eigenvectors ϕ in a hyper-plane with dimensionality equal to the eigenvalue's multiplicity [27]; as such, the derivative is not defined. Albeit, it is possible to compute directional eigenvalue derivatives using the generalized gradient method [31], however, most nonlinear programming algorithms cannot work with directional derivatives.

It was proven that a symmetric polynomial of eigenvalues, λ_i for $i = 1, \dots, n$, is a differentiable function, provided the set is isolated, i.e. $\dots \leq \lambda_0 < \lambda_1 \leq \dots \leq \lambda_n < \lambda_{n+1} \leq \dots$ [52]. Inspection of the inequalities reveals that the symmetric polynomial remains smooth even if the isolated set contains degenerate eigenvalues. This is an extremely powerful result that can be used to remove the eigenvalue degeneracy issue from topology optimization. Specifically, a “ p -norm” function defined on a vector \mathbf{a} as

$$l_p(\mathbf{a}) = \left(\sum_i a_i^p \right)^{\frac{1}{p}}, \quad (2.20)$$

is a symmetric polynomial raised to an exponent. We note that the usual p -norm absolute value is ignored since we assume $a_i > 0$. Thus, approximating the mode m eigenvalue

$$\lambda_m(\boldsymbol{\kappa}) \approx \tilde{\lambda}_m(\boldsymbol{\kappa}) = \left(\sum_{i=1}^m \lambda_i(\boldsymbol{\kappa})^p \right)^{\frac{1}{p}}, \quad (2.21)$$

and the mode $m + 1$ eigenvalue

$$\lambda_{m+1}(\boldsymbol{\kappa}) \approx \tilde{\lambda}_{m+1}(\boldsymbol{\kappa}) = \left(\sum_{i=m+1}^M \lambda_i(\boldsymbol{\kappa})^{-p} \right)^{\frac{1}{-p}}, \quad (2.22)$$

where M is sufficiently large to capture all repeated eigenvalues of $\lambda_{m+1}(\boldsymbol{\kappa})$, yields smooth approximations provided $\lambda_m \neq \lambda_{m+1}$. Although $\lambda_m \neq \lambda_{m+1}$ is not guaranteed across the entire design domain, the assumption is justified since it must hold for our bandgap designs. Note that our smooth approximation further requires $\lambda_M \neq \lambda_{M+1}$, although any errors introduced if $\lambda_M = \lambda_{M+1}$ are negligible in the sensitivity analysis provided $\lambda_M^p \gg \lambda_{m+1}^p$. So clearly, the accuracy of Equations (2.21)

and (2.22) is also controlled by the value of p , which must be sufficiently large to obtain a reasonable approximation, although poor optimization convergence is likely if p is too large. Substituting the approximations from Equations (2.21) and (2.22) into Equation (2.13) produces

$$\theta_\lambda \approx \frac{\min \tilde{\lambda}_{m+1}(\boldsymbol{\kappa}) - \max \tilde{\lambda}_m(\boldsymbol{\kappa})}{\frac{1}{2} (\min \tilde{\lambda}_{m+1}(\boldsymbol{\kappa}) + \max \tilde{\lambda}_m(\boldsymbol{\kappa}))} \quad \forall \boldsymbol{\kappa} \in \partial\mathcal{B}, \quad (2.23)$$

which effectively alleviates the non-differentiability caused by eigenvalue degeneracy.

Equation (2.23) still lacks the necessary differentiability for gradient-based optimization due to the min/max operations. Equation (2.20) is therefore applied to smoothly approximate these operations as

$$\max \tilde{\lambda}_m(\boldsymbol{\kappa}) \approx \tilde{\lambda}_1 = \left(\sum_{i=1}^{N_\kappa} \tilde{\lambda}_m(\boldsymbol{\kappa}_i)^p \right)^{\frac{1}{p}} \quad \boldsymbol{\kappa} \in \partial\mathcal{B} \quad (2.24)$$

$$\min \tilde{\lambda}_{m+1}(\boldsymbol{\kappa}) \approx \tilde{\lambda}_2 = \left(\sum_{i=1}^{N_\kappa} \tilde{\lambda}_{m+1}(\boldsymbol{\kappa}_i)^{-p} \right)^{\frac{1}{-p}} \quad \boldsymbol{\kappa} \in \partial\mathcal{B}, \quad (2.25)$$

where N_κ is the number of wave vectors chosen along $\partial\mathcal{B}$. Substituting Equations (2.24) and (2.25) into Equation (2.23) reveals the differentiable bandgap-midgap ratio approximation

$$\theta_\lambda \approx \tilde{\theta}_\lambda = \frac{\tilde{\lambda}_2 - \tilde{\lambda}_1}{\frac{1}{2} (\tilde{\lambda}_2 + \tilde{\lambda}_1)}. \quad (2.26)$$

2.1.8 Sensitivity analysis

As previously noted, the bandgap-midgap ratio will be influenced by the solid material volume fraction, which is parameterized by a set of design variables \mathbf{d} . Thus, the derivative of Equation (2.26) is required with respect to each design parameter d_i to perform efficient gradient-based optimization. The chain rule is used to compute each derivative according to

$$\frac{D\tilde{\theta}_\lambda}{Dd_i} = \frac{\partial\tilde{\theta}_\lambda}{\partial\tilde{\lambda}_1} \frac{D\tilde{\lambda}_1}{Dd_i} + \frac{\partial\tilde{\theta}_\lambda}{\partial\tilde{\lambda}_2} \frac{D\tilde{\lambda}_2}{Dd_i}, \quad (2.27)$$

which requires

$$\frac{\partial \tilde{\theta}_\lambda}{\partial \tilde{\lambda}_1} = \frac{-4\tilde{\lambda}_2}{(\tilde{\lambda}_2 + \tilde{\lambda}_1)^2} \quad (2.28)$$

and

$$\frac{\partial \tilde{\theta}_\lambda}{\partial \tilde{\lambda}_2} = \frac{4\tilde{\lambda}_1}{(\tilde{\lambda}_2 + \tilde{\lambda}_1)^2}. \quad (2.29)$$

To compute the total derivatives $\frac{D\tilde{\lambda}_1}{Dd_i}$ and $\frac{D\tilde{\lambda}_2}{Dd_i}$, the derivative of Equation (2.20) for a design dependent input vector \mathbf{a} is evaluated via the chain rule as

$$\frac{Dl_p(\mathbf{a})}{Dd_i} = \sum_j \frac{\partial l_p(\mathbf{a})}{\partial a_j} \frac{Da_j}{Dd_i}, \quad (2.30)$$

where

$$\frac{\partial l_p(\mathbf{a})}{\partial a_j} = \left(\sum_k a_k^p \right)^{\frac{1}{p}-1} a_j^{p-1}. \quad (2.31)$$

Equation (2.30) is applied to evaluate the derivatives of Equations (2.24) and (2.25), and then again applied to evaluate the derivatives of Equations (2.21) and (2.22), which are required for the chain rule applications. As discussed in Sec. 2.1.7, we see that the errors in the derivative computations of Equations (2.22) and (2.25) due to $\lambda_M = \lambda_{M+1}$ are small if $\lambda_M^p \gg \lambda_{m+1}^p$. Note that in the smooth minimum approximations we employ a negative exponent, i.e. $-p$, and therefore a_j^{-p-1} , cf. Equation (2.31), becomes very small for large a_j and large p .

At this point, only the derivatives of the eigenvalues $\frac{D\lambda}{Dd_i}$ remain. Despite the possibility for degenerate eigenvalues, Equation (2.19) may be utilized with assured smoothness through the use of symmetric polynomials [52]. Computing Equation (2.19) requires the discretized matrix-vector product $\frac{\partial A}{\partial d_i} \phi$, which may be computed using the matrix-free technique described in Sec. 2.1.2 with the caveat of multiplying by $\frac{D}{Dd_i} \left(\frac{1}{\varepsilon(\mathbf{x})} \right)$, rather than $\frac{1}{\varepsilon(\mathbf{x})}$, after transforming the solution via DFT to physical space. This technique may be feasible for a small number of design variables, but will likely become computationally prohibitive for the large number of design variables used in topology optimization. Fortunately, a more efficient technique to compute the $\frac{D\lambda}{Dd_i}$ exists when design variables have local support, which is the case in topology optimization. To see this we

examine a weak formulation of the eigenvalue problem, which is obtained by integrating the dot product of Equation (2.5) with an arbitrary weighting function \mathbf{w} over the computational domain Ω as

$$\int_{\Omega} \mathbf{w}(\mathbf{x}) \cdot \left(\nabla \times \left(\frac{1}{\varepsilon_r(\mathbf{x})} \nabla \times \mathbf{H}(\mathbf{x}) \right) \right) d\Omega = \int_{\Omega} \mathbf{w}(\mathbf{x}) \cdot \lambda \mathbf{H}(\mathbf{x}) d\Omega. \quad (2.32)$$

The vector identity

$$\nabla \cdot (\mathbf{a} \times \mathbf{b}) = \mathbf{b} \cdot (\nabla \times \mathbf{a}) - \mathbf{a} \cdot (\nabla \times \mathbf{b}) \quad (2.33)$$

is then applied to move a derivative from the solution field \mathbf{H} to the weighting function \mathbf{w} . Indeed, substituting $\mathbf{a} = \frac{1}{\varepsilon_r} \nabla \times \mathbf{H}$ and $\mathbf{b} = \mathbf{w}$ converts Equation (2.32) to

$$\begin{aligned} \int_{\Omega} \nabla \cdot \left(\left(\frac{1}{\varepsilon_r(\mathbf{x})} \nabla \times \mathbf{H}(\mathbf{x}) \right) \times \mathbf{w}(\mathbf{x}) \right) d\Omega + \int_{\Omega} \left(\frac{1}{\varepsilon_r(\mathbf{x})} \nabla \times \mathbf{H}(\mathbf{x}) \right) \cdot (\nabla \times \mathbf{w}(\mathbf{x})) d\Omega \\ = \lambda \int_{\Omega} \mathbf{w}(\mathbf{x}) \cdot \mathbf{H}(\mathbf{x}) d\Omega, \end{aligned} \quad (2.34)$$

and applying the divergence theorem to the first integral yields

$$\begin{aligned} \int_{\partial\Omega} \hat{\mathbf{n}}(\mathbf{x}) \cdot \left(\left(\frac{1}{\varepsilon_r(\mathbf{x})} \nabla \times \mathbf{H}(\mathbf{x}) \right) \times \mathbf{w}(\mathbf{x}) \right) d\Omega + \int_{\Omega} \left(\frac{1}{\varepsilon_r(\mathbf{x})} \nabla \times \mathbf{H}(\mathbf{x}) \right) \cdot (\nabla \times \mathbf{w}(\mathbf{x})) d\Omega \\ = \lambda \int_{\Omega} \mathbf{w}(\mathbf{x}) \cdot \mathbf{H}(\mathbf{x}) d\Omega, \end{aligned} \quad (2.35)$$

where $\hat{\mathbf{n}}$ is the outward facing normal vector. Finally, the periodic boundary condition annihilates the boundary integral leaving the eigenvalue problem of finding the admissible \mathbf{H} such that

$$\int_{\Omega} \frac{1}{\varepsilon_r(\mathbf{x})} (\nabla \times \mathbf{H}(\mathbf{x})) \cdot (\nabla \times \mathbf{w}(\mathbf{x})) d\Omega = \lambda \int_{\Omega} \mathbf{w}(\mathbf{x}) \cdot \mathbf{H}(\mathbf{x}) d\Omega. \quad (2.36)$$

for all admissible \mathbf{w} . Here we see that upon discretization, Equation (2.36) is of the form $\mathbf{A}\mathbf{H} = \lambda\mathbf{H}$. Taking the variation of Equation (2.36) yields

$$\begin{aligned} \int_{\Omega} \delta \left(\frac{1}{\varepsilon_r(\mathbf{x})} \right) (\nabla \times \mathbf{H}(\mathbf{x})) \cdot (\nabla \times \mathbf{w}(\mathbf{x})) d\Omega + \int_{\Omega} \frac{1}{\varepsilon_r(\mathbf{x})} (\nabla \times \delta \mathbf{H}(\mathbf{x})) \cdot (\nabla \times \mathbf{w}(\mathbf{x})) d\Omega \\ = \delta \lambda \int_{\Omega} \mathbf{w}(\mathbf{x}) \cdot \mathbf{H}(\mathbf{x}) d\Omega + \lambda \int_{\Omega} \mathbf{w}(\mathbf{x}) \cdot \delta \mathbf{H}(\mathbf{x}) d\Omega. \end{aligned} \quad (2.37)$$

where we use Equation (2.36) to cancel the $\delta\mathbf{w}$ terms, since $\delta\mathbf{w}$ is admissible. Assigning the arbitrary weighting function $\mathbf{w} = \mathbf{H}$ yields

$$\begin{aligned} & \int_{\Omega} \delta \left(\frac{1}{\varepsilon_r(\mathbf{x})} \right) (\nabla \times \mathbf{H}(\mathbf{x})) \cdot (\nabla \times \mathbf{H}(\mathbf{x})) \, d\Omega + \int_{\Omega} \frac{1}{\varepsilon_r(\mathbf{x})} (\nabla \times \delta\mathbf{H}(\mathbf{x})) \cdot (\nabla \times \mathbf{H}(\mathbf{x})) \, d\Omega \\ & = \delta\lambda \int_{\Omega} \mathbf{H}(\mathbf{x}) \cdot \mathbf{H}(\mathbf{x}) \, d\Omega + \lambda \int_{\Omega} \mathbf{H}(\mathbf{x}) \cdot \delta\mathbf{H}(\mathbf{x}) \, d\Omega, \end{aligned} \quad (2.38)$$

which reduces to

$$\int_{\Omega} \delta \left(\frac{1}{\varepsilon_r(\mathbf{x})} \right) (\nabla \times \mathbf{H}(\mathbf{x})) \cdot (\nabla \times \mathbf{H}(\mathbf{x})) \, d\Omega = \delta\lambda \int_{\Omega} \mathbf{H}(\mathbf{x}) \cdot \mathbf{H}(\mathbf{x}) \, d\Omega, \quad (2.39)$$

where we again used the fact that Equation (2.36) holds for the admissible $\mathbf{w} = \delta\mathbf{H}$. Solving for $\delta\lambda$ leaves the expression

$$\delta\lambda = \left(\int_{\Omega} \mathbf{H}(\mathbf{x}) \cdot \mathbf{H}(\mathbf{x}) \, d\Omega \right)^{-1} \int_{\Omega} (\nabla \times \mathbf{H}(\mathbf{x})) \cdot \delta \left(\frac{1}{\varepsilon_r(\mathbf{x})} \right) (\nabla \times \mathbf{H}(\mathbf{x})) \, d\Omega. \quad (2.40)$$

Upon evaluating $\delta\lambda$ with respect to a variation in the voxel i filtered volume fraction \tilde{d}_i , we obtain

$$\frac{D\lambda}{D\tilde{d}_i} = \left(\int_{\Omega} \mathbf{H}(\mathbf{x}) \cdot \mathbf{H}(\mathbf{x}) \, d\Omega \right)^{-1} \int_{\Omega} (\nabla \times \mathbf{H}(\mathbf{x})) \cdot \frac{D}{D\tilde{d}_i} \left(\frac{1}{\varepsilon_r(\mathbf{x})} \right) (\nabla \times \mathbf{H}(\mathbf{x})) \, d\Omega. \quad (2.41)$$

We notice here that upon discretization Equation (2.41) is of the same form as Equation (2.19). Equation (2.41) is advantageous for the eigenvalue derivative computation because the second integral is only non-zero over the voxel i corresponding to filtered design variable \tilde{d}_i . The key to using this technique with a plane wave basis is to compute $\nabla \times \mathbf{H}$ in wave vector space and then obtain the physical vectors from a DFT. Also, many eigenvalue solvers scale the eigenvectors such that $\int_{\Omega} \mathbf{H}(\mathbf{x}) \cdot \mathbf{H}(\mathbf{x}) \, d\Omega = 1$, so this global integral may not need to be computed. The execution time will likely be many orders of magnitude (problem size dependent) faster than treating local design variables as if they were global and using Equation (2.19). Finally, the chain rule is

completed by evaluating the derivative of the permittivity in the voxel i , i.e.

$$\frac{D}{D\tilde{d}_i} \left(\frac{1}{\varepsilon_r} \right) = \frac{-1}{\varepsilon_r^2} \frac{D\varepsilon_r}{D\tilde{d}_i}, \quad (2.42)$$

where $\frac{D\varepsilon_r}{D\tilde{d}_i}$ is obtained by differentiating Equation (2.18) as

$$\frac{D\varepsilon_r}{D\tilde{d}_i} = (\varepsilon_1 - \varepsilon_0). \quad (2.43)$$

The above procedure is used to obtain derivatives of $\tilde{\theta}_\lambda$ with respect to filtered volume fractions \tilde{d}_i , however, we must supply derivatives with respect to the design variables d_j to the NLP algorithm. Differentiating Equation (2.15) provides the required relation

$$\frac{D\tilde{d}_i}{Dd_j} = W_{ij}, \quad (2.44)$$

so that we may finally compute

$$\frac{D\tilde{\theta}_\lambda}{Dd_j} = \frac{D\tilde{\theta}_\lambda}{D\tilde{d}_i} \frac{D\tilde{d}_i}{Dd_j} = \frac{D\tilde{\theta}_\lambda}{D\tilde{d}_i} W_{ij}. \quad (2.45)$$

The steps outlined above are used to compute the sensitivity of the objective function with respect to the volume fraction of each voxel in the unit cell. However, since only the volume fractions of voxels in the symmetry cell are free design variables, the sensitivity contributions from each voxel in the unit cell must be appropriately allocated to its corresponding voxel in the symmetry cell. For a 3D design parameterization with orthorhombic symmetry, the sensitivity contributions from the 8 symmetry reflected voxels in the unit cell are summed to compute the sensitivity with respect to the volume fraction of their corresponding symmetry cell voxel.

2.1.9 Nested mesh refinement

The full dispersion analysis required to predict a photonic bandgap becomes a computationally expensive endeavor as the solution basis and the discretization of $\partial\mathcal{B}$ are both refined. Parallel

calculations speed the analysis considerably; each eigenvalue calculation can be parallelized along one-dimension of the unit cell, while the scan of the Brillouin zone boundary $\partial\mathcal{B}$ is embarrassingly parallel, as noted in Sec. 2.1.3. Unfortunately, the calculation wall clock time can still exceed a few hours on an advanced supercomputer when the number of design variables exceeds 10^3 , despite leveraging multi-level parallelism. To further reduce the computational cost of our 3D studies, a nested mesh refinement technique is developed.

Nonlinear programming is used to solve the bound-constrained optimization problem

$$\begin{aligned} & \underset{d}{\text{maximize}} && \tilde{\theta}_\lambda \\ & \text{subject to} && 0 \leq d_j \leq 1, \end{aligned} \tag{2.46}$$

where $\tilde{\theta}_\lambda$ is defined in Equation (2.26). Note that modes m , and thus $m+1$, are selected *a priori*. We use a reduced space approach whereby the Maxwell equations are strictly enforced and accounted for in the sensitivity analysis presented in Sec. 2.1.8. The discrete representation of the symmetry cell begins as a coarse grid of only 2^3 voxels whose volume fractions are randomly assigned. This symmetry cell is subsequently reflected within the unit cell to enforce orthorhombic symmetry, corresponding to an analysis grid of 4^3 voxels. We then solve the topology optimization problem on this coarse grid. Upon convergence, the optimized design field is uniformly refined, cf. Fig. 2.5, and a subsequent optimization begins from the converged coarse design. Note that this uniform refinement does not change the physical structure (sans filtering), but rather subdivides each voxel in the symmetry cell into 8 sub-voxels, whose volume fractions serve as design variables in the

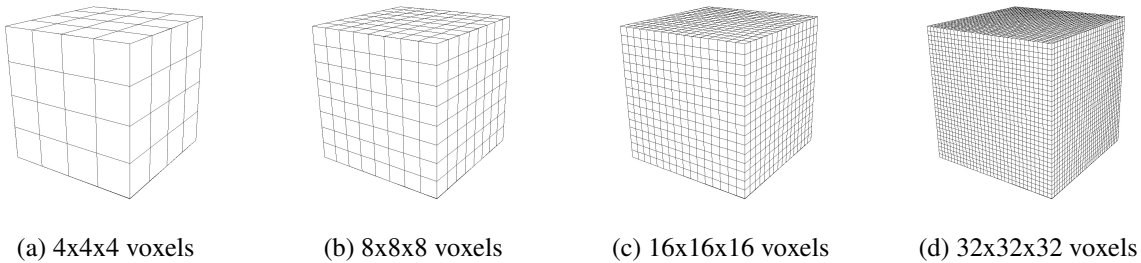


Figure 2.5 Uniformly refined unit cells

refined topology optimization problem. This process continues until the design grid has been sufficiently refined to resolve the desired feature size. It is also recommended to refine the grid at least twice to achieve reasonable bandgap predictions.

2.1.10 Post-processing

A post-processing analysis of the optimized design is performed for two reasons. The first is to interpret structures consisting purely of binary designs, and the second is to verify that the photonic bandgap predicted by considering only a discrete set of vectors κ on the Brillouin zone boundary $\partial\mathcal{B}$ is valid, i.e. that there are no wave vectors κ in the interior of \mathcal{B} that will propagate with a frequency that lies in the bandgap. Therefore, designs are thresholded by rounding volume fractions to 0 or 1 such that voxels with intermediate volume fractions are removed and a binary structure remains. The entire irreducible Brillouin zone, i.e. the interior \mathcal{B} and boundary $\partial\mathcal{B}$, is then considered by analyzing this binary structure at wave vectors κ from a uniformly spaced sampling to ensure that the predicted bandgaps are valid. This uniform sampling of \mathcal{B} consisted of 11 samples per spatial dimensions, for a total of 1331 κ vectors. Fortunately, in all cases it was determined that the bandgap predicted by scanning the boundary $\partial\mathcal{B}$ was consistent with the bandgap predicted by scanning the entirety of \mathcal{B} . Further, the thresholded binary designs were often superior due to their sharper material contrast.

2.2 Results and discussion

2.2.1 Complete 2D bandgaps

The techniques described in Sec. 2.1 were applied to design 3D photonic crystals with complete 2D bandgaps. The relevant numerical parameters that remain constant throughout this work are listed in Tab. 2.1. Structures with complete 2D bandgaps were designed by solving Equation (2.46) with a 2D Brillouin zone such that $\partial\mathcal{B}$ is restricted to the $x - y$ plane, with a κ spacing of $\frac{2\pi}{8a}$. The first 8 possible gaps are considered, which begin between modes 2 and 3, since it is impossible to split modes 1 and 2 due their shared frequency of 0 at $\kappa = \mathbf{0}$. Note that M from Equation 2.22 was

Description	Symbol	Value
void space relative permittivity	ϵ_0	1.0
solid material relative permittivity	ϵ_1	13.0
p -norm exponent	p	30
$\partial\mathcal{B}$ discretization	$\Delta\kappa$	$\frac{2\pi}{8a}$
eigenvalue tolerance	ϵ_λ	1e-5
NLP tolerance	ϵ_θ	1e-5

Table 2.1 Numerical Parameters

selected such that 4 modes above the desired bandgap were computed, i.e. $M = m + 4$; this was sufficient in all cases to ensure differentiability of the p -norm, i.e. such that $\lambda_M^p \gg \lambda_{m+1}^p$. The filter radius r is selected *a priori* to limit feature size. Since r remains constant throughout the mesh refinements, the filter will have no effect until the voxel spacing Δx is smaller than r . Thus, the filter is “activated” at some point in the mesh refinement process. It was observed in practice that proper selection of r is paramount to achieving a bandgap structure. If r is too large then the design may not have the necessary freedom to create a bandgap, while if r is too small fine-scale features appear which are difficult to fabricate and optimizations take longer to converge. Specifically, the best results were obtained when r was selected in the range $\frac{a}{32} < r < \frac{a}{8}$, which always activates the filter before attempting the fourth optimization on the 32^3 voxel unit cell.

The initial and optimal volume fractions, along with their corresponding dispersion plots, for each step in the nested mesh refinement process are displayed in Fig. 2.6 for a structure exhibiting a 2D bandgap between modes 5 and 6. A filter radius of $r = 0.05a$ was selected. Note that the initial design for the coarsest resolution is random. It is apparent that each design in the nested mesh refinement process converges to roughly the same design as its predecessor. Geometric features that cannot be fully resolved by the coarse discretizations appear with intermediate volume fractions, but as the mesh is refined the designs tend toward binary, aside from the interface smearing due to the filtering. As seen here, once a filter radius is selected to enforce a minimum feature size, mesh refinements must occur until features with those sizes can be fully resolved, resulting in a binary design without strictly enforcing this binary behavior.

An interesting observation is that the design performance is often over-estimated on the coarse

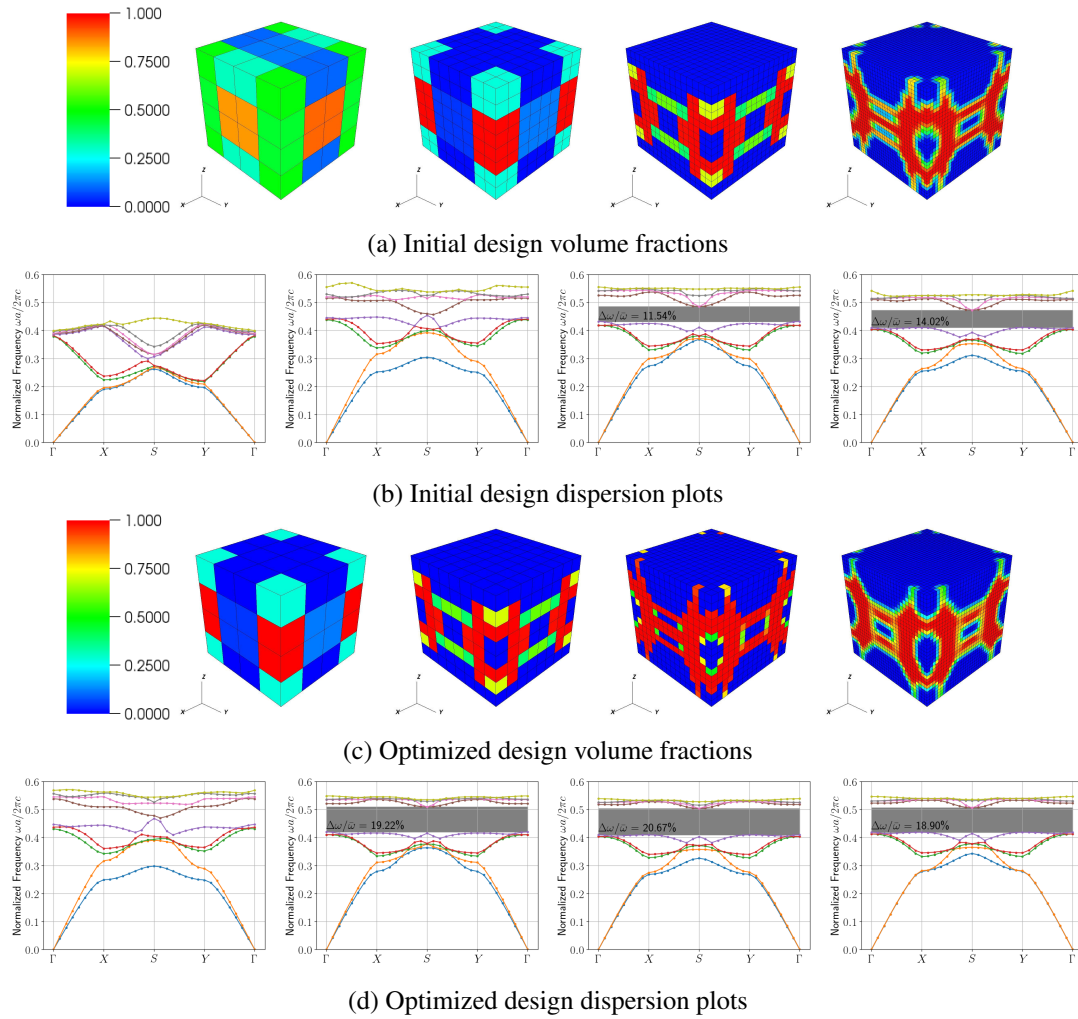


Figure 2.6 Nested mesh refinement for complete 2D bandgap

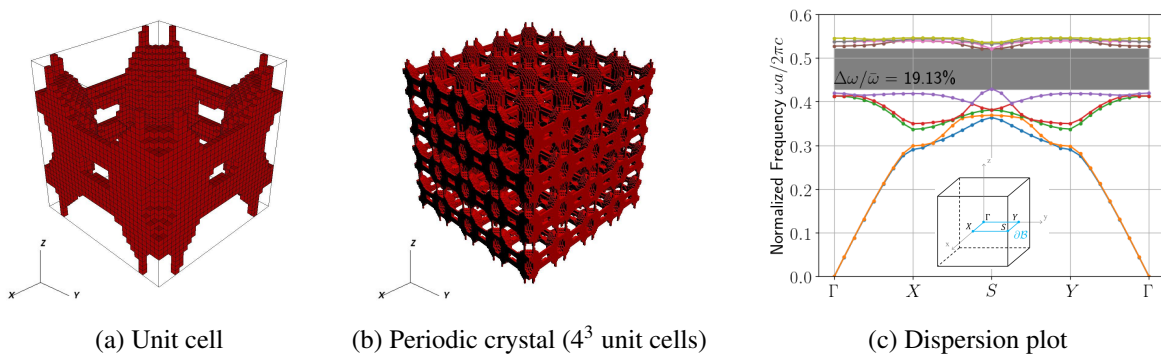


Figure 2.7 Post-processed photonic crystal with complete 2D bandgap between modes 5-6

grid. Fortunately, this effect is reduced in each mesh refinement step as the simulations become more accurate. Not surprisingly, design performance is decreased when the filter is activated, cf. Fig. 2.6. Note that this filter activation refers to a uniform mesh refinement that causes $\Delta x < r$, i.e. the design variables do not change. This follows intuition that a photonic bandgap prefers stark material contrast, which is reduced when the filter smears the material interface. Despite these effects, the increased design freedom due to mesh refinement usually improves performance.

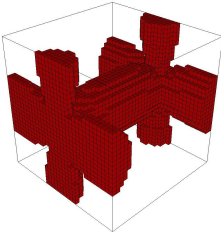
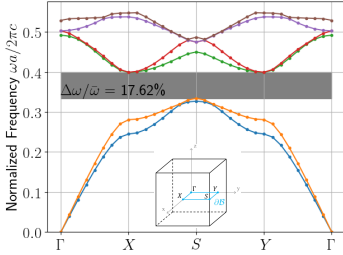
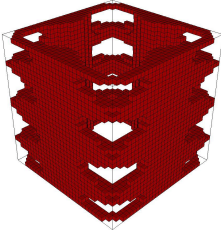
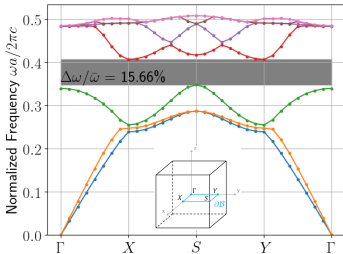
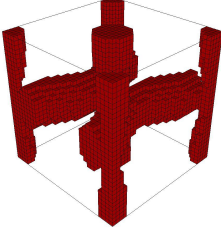
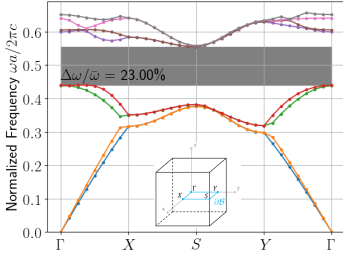
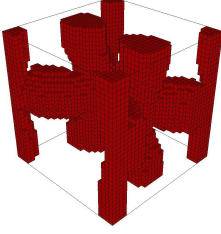
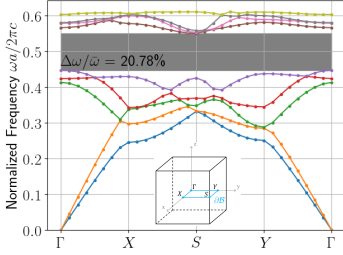
Modes (m-m+1)	Best structure	Dispersion plot	Bandgap probability
2-3			$\frac{26}{30} = 86.7\%$
3-4			$\frac{10}{30} = 33.3\%$
4-5			$\frac{7}{30} = 23.3\%$
5-6			$\frac{27}{30} = 90.0\%$

Table 2.2 Summary of complete 2D bandgap optimizations (gaps 1-4)

The post-processed unit cell and its corresponding periodic photonic crystal are illustrated in Fig. 2.7, along with the dispersion plot from this binary design. Images of post-processed, i.e. binary, designs throughout this work display only the solid material to better examine the structure. The full \mathcal{B} scan described in Sec. 2.1.10 was also performed to verify the bandgap performance predicted by the $\partial\mathcal{B}$ scan.

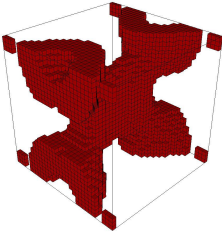
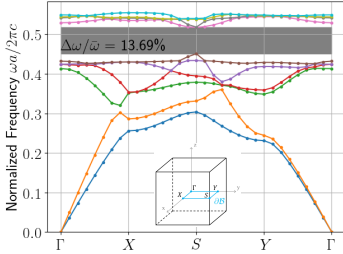
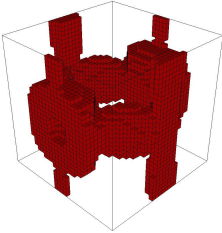
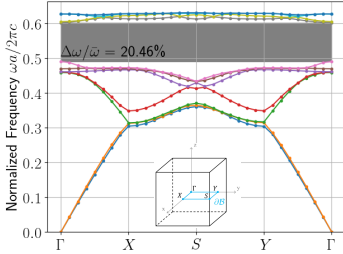
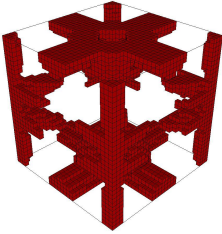
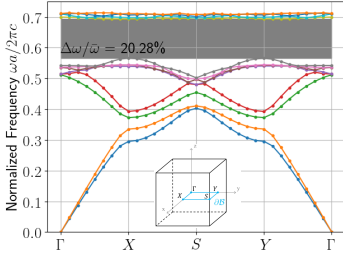
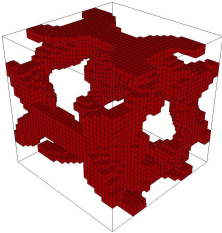
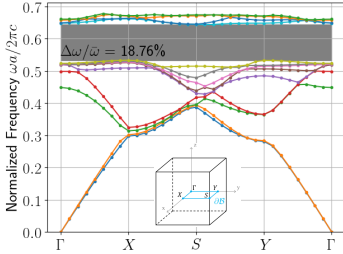
Modes (m-m+1)	Best structure	Dispersion plot	Bandgap probability
6-7			$\frac{1}{30} = 3.3\%$
7-8			$\frac{3}{30} = 10.0\%$
8-9			$\frac{12}{30} = 40.0\%$
9-10			$\frac{2}{30} = 6.67\%$

Table 2.3 Summary of complete 2D bandgap optimizations (gaps 5-8)

Tabs. 2.2 and 2.3 present the best 2D photonic bandgap structures obtained from 30 random initial designs for each of the first 8 possible bandgaps. The post-processed performance of the best structures are also presented, along with the percentage of random initial designs that yield bandgap structures. Although a formal study was not performed, our experience shows that increasing the κ spacing above $\frac{2\pi}{8a}$ results in a smaller percentage of initial designs yielding bandgap structures.

2.2.2 Complete 3D Bandgaps

Designing photonic crystals with complete 3D bandgaps is considerably more difficult than with complete 2D bandgaps. Similar to the 2D bandgap study, 30 random initial designs were used for each of the first 8 possible bandgaps, yet only 3 unique photonic crystals with complete 3D bandgaps were obtained using the same $r = 0.05a$ filter radius. The optimal designs at each mesh resolution for the three successful 3D bandgap designs are displayed in Figs. 2.8-2.10, along with their post-processed unit cells and dispersion plots. Many of the random initial designs converged to the same optimal structure; specifically, 19/30 converged to the design pictured in Fig. 2.8 for $m = 2$, 6/30 converged to the design pictured in Fig. 2.9 for $m = 5$, and 7/30 converged to the design pictured in Fig. 2.10 for $m = 6$.

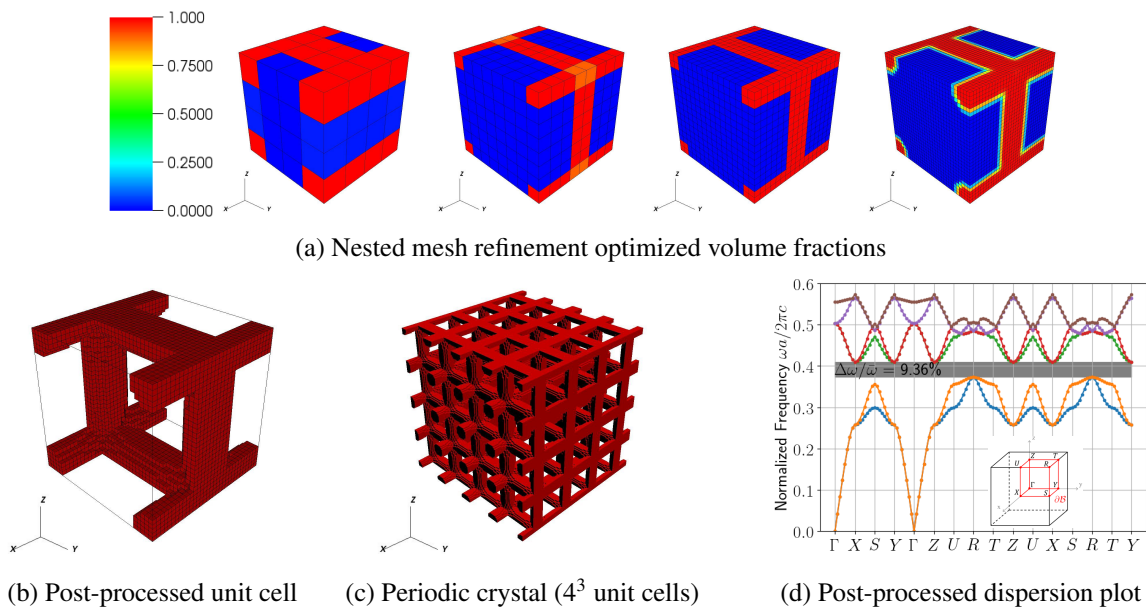


Figure 2.8 Photonic crystal with complete 3D bandgap between modes 2-3

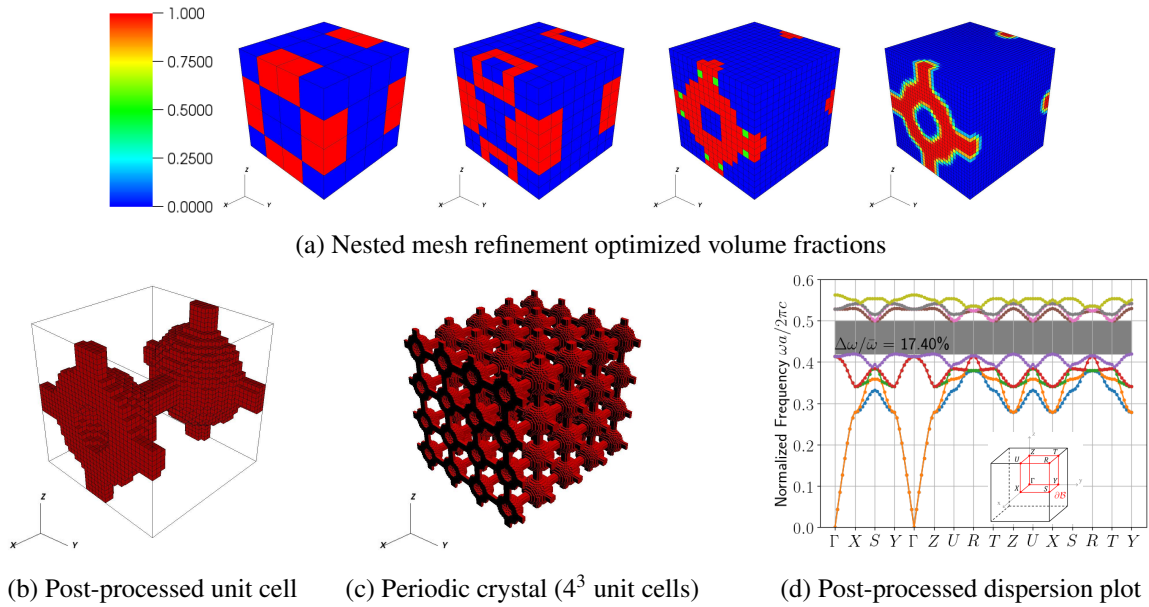


Figure 2.9 Photonic crystal with complete 3D bandgap between modes 5-6

It is interesting to note that the design in Fig. 2.9 is very similar to a previously published optimal design [35]. This further validates the presented implementation. Also, it lends confidence to the possibility that global optimum are obtainable by the nested mesh refinement strategy, since [35] used a fixed grid throughout the optimization. Additionally, it is promising that the semidefinite programming reformulation in [35] produced the same result as the interior point NLP algorithm employed here, implying a consistency between methods and further justifying our lack of permittivity smoothing. An advantage of the proposed method over the semidefinite programming method is the ability to easily incorporate other design parameterizations and nonlinear constraints.

The structure displayed in Fig. 2.10 has not, to the knowledge of the authors, been previously published. Although the performance does not exceed that of known structures, it is important to have the capability to find new bandgap structures that may be more robust to defects, or have better multi-functional properties. Extending the presented framework to other unit cell symmetries or attempting to split higher modes with a more refined mesh could very well produce novel bandgap structures with better performance than what has previously been produced.

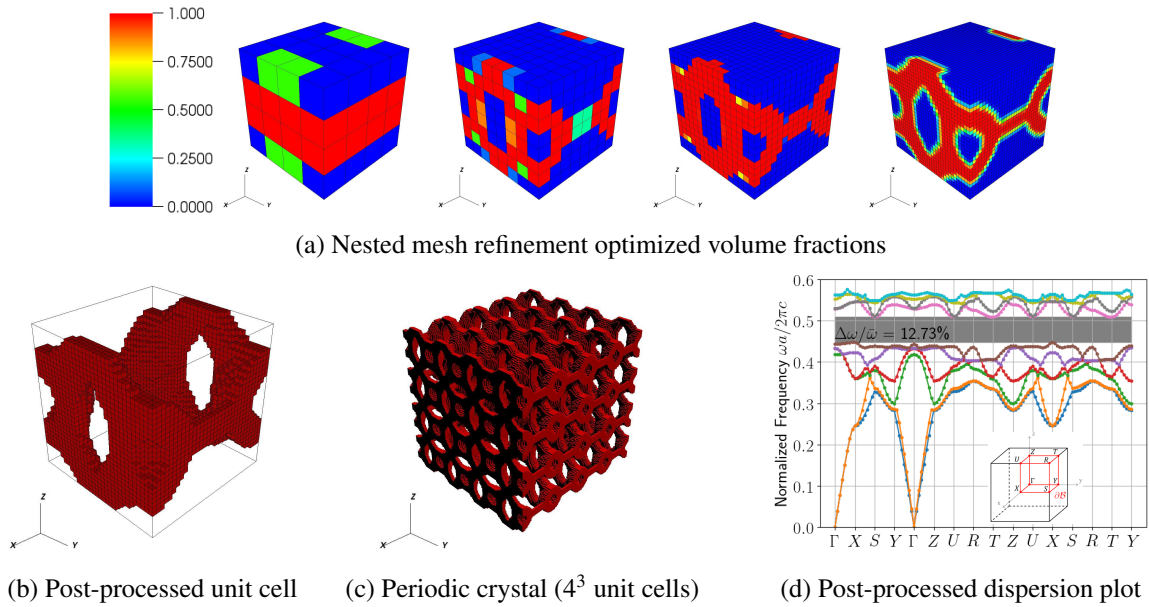


Figure 2.10 Photonic crystal with complete 3D bandgap between modes 6-7

2.2.3 Computational expense

Photonic crystal design for complete bandgap is a computationally expensive endeavor. The discrete eigenvalue analyses resulting from the fully-vectorial formulation consist of real and imaginary parts with two DOF per voxel, producing a discrete system with $4n^3$ DOF for an analysis grid with n voxels along each spatial dimension of the unit cell. For context, the eigenvalue problems derived from the 32^3 grids have 131,072 DOF. Further, it is generally required to compute the lowest ≈ 10 eigenvalues, and it was necessary to analyze 32 and 92 κ vectors along $\partial\mathcal{B}$ to design for complete 2D and 3D bandgaps, respectively. The NLP algorithm generally converged within ≈ 300 design iterations on each of the four nested mesh refinement grids for a total of $\approx 38,400$ and $\approx 110,400$ eigenvalue analyses when designing for complete 2D and 3D bandgaps, respectively. The 2D bandgap optimizations were solved on 512 processors, while the 3D bandgap optimizations were solved on 1,472 processors, both requiring ≈ 4 hours of execution time. Nested mesh refinement significantly reduced the number of iterations required, although the time savings were not computed since convergence to a bandgap structure from a random initial design at the 32^3 grid resolution could not be obtained within the 24 hour time limit of the Lawrence Livermore National Laboratory (LLNL) computing cluster used throughout.

2.3 Conclusions

Topology optimization has successfully been applied to design 3D photonic crystals with complete 2D and 3D bandgaps. A technique for smoothing the bandgap-midgap ratio utilizes the symmetric architecture of a “ p -norm” function to remove non-smoothness caused by eigenvalue degeneracies and min/max operations, allowing the usual gradient-based nonlinear programming solvers to be employed.

Nested mesh refinement alleviates the computational burden from the high dimensional design spaces required to optimize 3D bandgap structures. Optimal designs naturally converge to binary structures after sufficient mesh refinement, and a periodic cone filter is successfully applied to enforce a minimum length scale in the optimized designs.

The presented framework is general enough to design photonic crystals with any domain symmetry, provided the unit cell is a rectangular prism. Three-dimensional photonic crystals with orthorhombic symmetry were designed with complete 2D bandgaps between each of the first 8 possible mode pairs, and complete 3D bandgaps between 3 different mode pairs. The sizes of the bandgaps presented here are competitive with the largest described in the literature.

CHAPTER 3: MANUFACTURING AND STIFFNESS CONSTRAINTS FOR TOPOLOGY OPTIMIZED PERIODIC STRUCTURES

This chapter describes a series of constraints that ensure structures are fully self-supporting and lack islands of solid material (ISM) and enclosed void space (EVS). These constraints are general enough to be added to any topology optimization framework since they do not rely on changing the design parameterization or filtering design variables. First, the formulation for each constraint is provided along with sensitivity analyses. Then, the constraints are compared and contrasted by evaluating each on a series of example unit cells so that guidelines may be presented for effective constraint combinations. Further, a geometry-based test problem is used to study the behavior of each constraint and aid in constraint limit selection. Finally, results from Chapter 2 are re-visited in order to ensure the photonic crystal designs are manufacturable and to study the trade-off between stiffness and bandgap performance. The work presented in this chapter has been submitted for publication in *Structural and Multidisciplinary Optimization*.

3.1 Constraint formulations

The constraints presented in this chapter are all physics-based. Thus, the governing partial differential equation (PDE) for each constraint is presented here, and the required sensitivity analyses are derived as well. The material interpolations are described in detail since they were crucial to obtaining convergence when the constraints were employed in a design optimization.

3.1.1 Virtual temperature method

The virtual temperature method (VTM) [74], equivalently formulated as the virtual scalar field method [96], was proposed as a technique to prevent EVS in topology optimized designs. A

virtual “temperature” field is computed which satisfies the steady-state heat conduction equation

$$\begin{aligned}\nabla \cdot (k(\mathbf{x}) \nabla T(\mathbf{x})) + Q(\mathbf{x}) &= 0 \quad \text{for } \mathbf{x} \in \Omega \\ T(\mathbf{x}) &= 0 \quad \text{for } \mathbf{x} \in \partial\Omega,\end{aligned}\tag{3.47}$$

where k is the conductivity, Q is a heat source, and T is the virtual temperature field at spatial coordinate \mathbf{x} . Although we are designing a periodic structure, the domain Ω considered for this constraint only consists of a single unit cell and we do not enforce periodic boundary conditions. This point is elaborated on in Section 3.1.1.

This technique works by placing both the heat source and highly conductive material in the void phase, while placing insulating material in the solid material. Thus, a much larger maximum domain temperature is observed when a region of void space is disconnected from the domain boundary $\partial\Omega$ since the heat source is not be able to dissipate as it would if all of the void space was in contact with $\partial\Omega$. Specifically, the conductivity is computed as a function of the solid phase volume fraction $\tilde{v} \in [0, 1]$ according to a SIMP-like [91] interpolation

$$k(\tilde{v}) = \varepsilon_e k_0 + (1 - \tilde{v})^q (k_0 - \varepsilon_e k_0),\tag{3.48}$$

so that $k = k_0$ for $\tilde{v} = 0$ and $k = \varepsilon_e k_0$ for $\tilde{v} = 1$, i.e., we place highly conductive material k_0 in the $\tilde{v} = 0$ void phase and insulating material ($\varepsilon_e \ll 1$) in the $\tilde{v} = 1$ solid phase. We should note that these VTM material properties are not physical, e.g. we would not expect void space to be more conductive than solid material. Also, we are using an ersatz representation of void space and denoting the ratio of the void space properties to the solid phase properties by ε_e .

Selecting exponent values $q > 1$ serves to penalize intermediate volume fractions $\tilde{v} \in (0, 1)$ by reducing their conductivity-to-heat source ratios. This is directly analogous to the SIMP method for compliance minimization [91] wherein the stiffness of intermediate volume fraction material is reduced relative to its mass so that optimal solutions contain only $\tilde{v} = 0$ or $\tilde{v} = 1$. Here, the conductivity of intermediate volume fraction material is reduced relative to its heat source so that

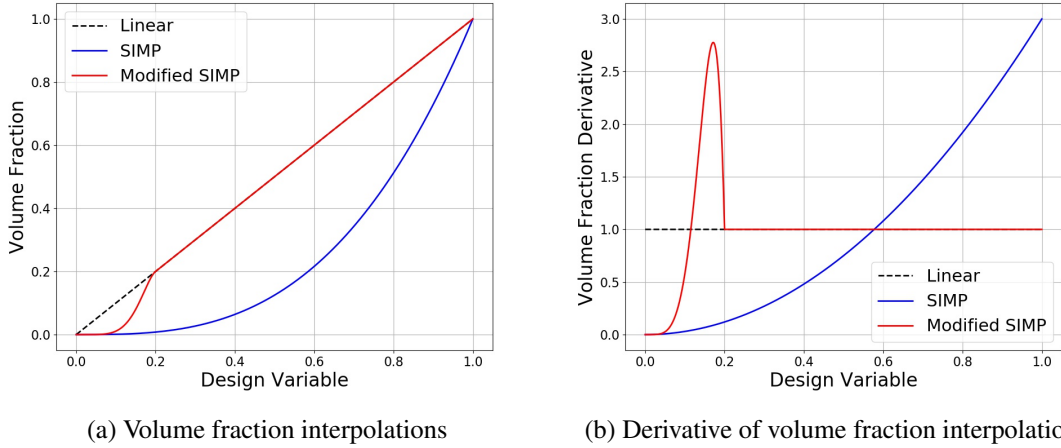


Figure 3.1 A comparison of volume fraction interpolations

optimal solutions prefer $\tilde{\nu} = 0$ or $\tilde{\nu} = 1$, since the intermediate volume fraction is inefficient at lowering the domain temperature.

The heat source should only be present in the void phase and hence it is a function of $\tilde{\nu}$. However, it was observed in practice that using a linear interpolation, i.e. $Q(\tilde{\nu}) = (1 - \tilde{\nu}) Q_0$ where Q_0 is the heat source value of the void phase, caused nonphysical behavior, e.g. negative temperatures, in regions with intermediate volume fraction. Fortunately, a modified SIMP interpolation scheme originally developed to remove spurious eigenmodes caused by low volume fraction elements [97] was able to resolve this issue. Figure 3.1 presents interpolations and their derivatives. We can see that very low volume fractions are heavily penalized with the modified SIMP, but importantly the interpolation is C^1 continuous. We invert the modified SIMP interpolation so that the heat source in high volume fractions is penalized, i.e.

$$Q(\tilde{\nu}) = \begin{cases} (c_1 (1 - \tilde{\nu})^r + c_2 (1 - \tilde{\nu})^{r+1}) Q_0 & \tilde{\nu} \geq \tilde{\nu}_U \\ (1 - \tilde{\nu}) Q_0 & \tilde{\nu} < \tilde{\nu}_U \end{cases} \quad (3.49)$$

where $r > q$, $\tilde{\nu}_U$ is a volume fraction upper bound, and the constants c_1 and c_2 are selected to ensure the material interpolation scheme remains C^1 continuous. To enforce this continuity we require that both expressions in Equation (3.49) produce the same value of $Q(\tilde{\nu}_U)$ and $Q'(\tilde{\nu}_U)$ from

which we obtain

$$c_1 = r(1 - \tilde{\nu}_U)^{1-r} \quad (3.50)$$

and

$$c_2 = (1 - r)(1 - \tilde{\nu}_U)^{-r}. \quad (3.51)$$

Note that for any choice of $\tilde{\nu}_U \in (0, 1)$ we will obtain $Q = Q_0$ for $\tilde{\nu} = 0$ and $Q = 0$ for $\tilde{\nu} = 1$. The boundary condition on $\partial\Omega$ allows heat to escape from Ω . Thus, EVS is easily identified by the presence of regions with high temperatures. We compute the maximum temperature in the domain using the differentiable p -norm function

$$\theta_{vt} = \left(\int_{\Omega} T(\mathbf{x})^p \, d\Omega \right)^{\frac{1}{p}}, \quad (3.52)$$

from which we formulate an optimization constraint as

$$\theta_{vt} \leq \mu_{vt} \bar{\theta}_{vt}, \quad (3.53)$$

where μ_{vt} is a user-selected constant and $\bar{\theta}_{vt}$ is computed by Equation (3.52) after solving Equation (3.47) with $\tilde{\nu}(\mathbf{x}) = 0$ for all $\mathbf{x} \in \Omega$ so that the constraint limit is not problem dependent.

Henceforth we will use the subscript vtv when Equation (3.53) is applied with the conductive material and heat source placed in the void phase as described above, and we will use the subscript vtS when Equation (3.53) is applied with the conductive material and heat source placed in the solid material as described in Section 3.1.1.

Extending the VTM to identify ISM

The VTM presented in Section 3.1.1 provides a quantitative means of identifying and preventing EVS. We propose a simple extension of this method to identify and prevent ISM. By simply

inverting the interpolations in Equations (3.48) and (3.49) to

$$k(\tilde{v}) = \varepsilon_e k_0 + \tilde{v}^q (k_0 - \varepsilon_e k_0) \quad (3.54)$$

and

$$Q(\tilde{v}) = \begin{cases} (c_1 \tilde{v}^r + c_2 \tilde{v}^{r+1}) Q_0 & \tilde{v} \leq \tilde{v}_L \\ \tilde{v} Q_0 & \tilde{v} > \tilde{v}_L \end{cases} \quad (3.55)$$

respectively, we place the the conductive material and heat source in the solid rather than the void region. Repeating our continuity requirements we obtain

$$c_1 = r \tilde{v}_L^{1-r} \quad (3.56)$$

and

$$c_2 = (1 - r) \tilde{v}_L^{-r}. \quad (3.57)$$

In this way the maximum temperature will be large when we have regions of solid material not connected to a boundary. We can simultaneously restrict EVS and ISM by solving Equation (3.47) twice; once using Equations (3.48) and (3.49) and again using Equations (3.54) and (3.55) and constraining the maximum value of each temperature field.

Extending to periodic domains

To the authors' knowledge the VTM has only been applied to finite domains, although the effect of boundary conditions has been explored [42]. We propose a technique to use VTM to prevent EVS and ISM in periodic structures. Consider a 2D microstructure consisting of solid material and a square array of circular voids. If we apply the VTM to the unit cell pictured in Figure 3.2a, we would identify EVS. However, if we apply the VTM to the unit cell pictured in Figure 3.2b, we will not identify EVS even though both unit cells represent the same periodic structure. Thus, we have an unacceptable problem; the behavior of our constraint function depends on the unit cell choice.

To alleviate this issue, we will propose a solution wherein we simply consider a 2^d array of unit cells, where d is the spatial dimension of our design problem. Indeed, consider the unit cell arrays highlighted in Figures 3.3a and 3.3b. Although the number of “hot” regions will be different, the behavior of the constraint will be consistent, i.e. EVS will be identified in either case. In fact, any array of 2^d unit cells allows the VTM to appropriately identify EVS and ISM.

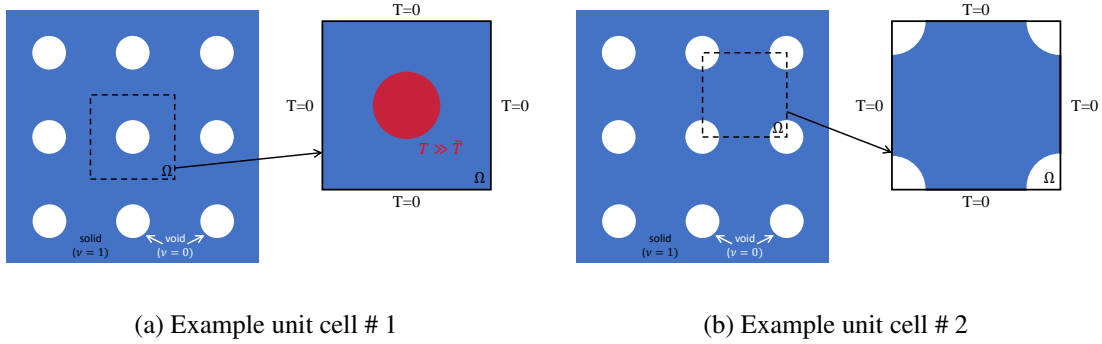


Figure 3.2 Example behavior when a single unit cell is analyzed with VTM

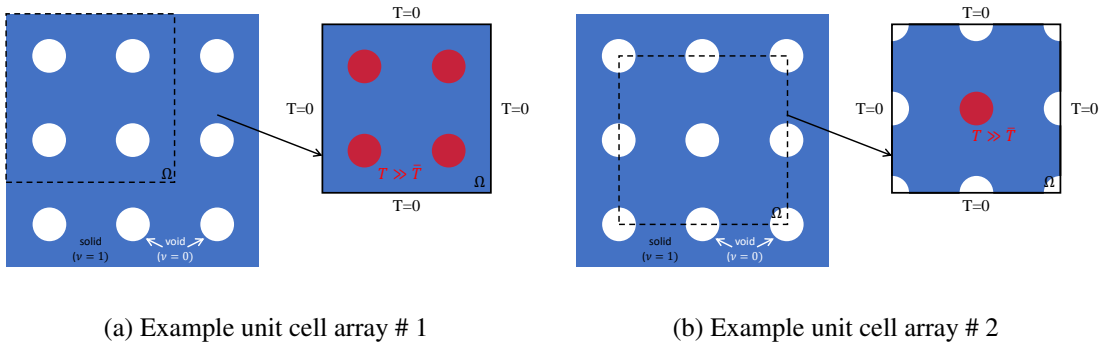


Figure 3.3 Example behavior when a 2^2 unit cell array is analyzed with VTM

Sensitivity analysis

We must compute the sensitivities of our constraint functions with respect to design variables to solve our design optimization problem via nonlinear programming (NLP). Here we derive the sensitivities of our constraint functions with respect to the volume fraction field \tilde{v} . However, we emphasize that other design parameterizations could be employed, e.g. projection methods [98] or B-splines [99].

We evaluate the variation of Equation (3.52) to obtain

$$\delta\theta_{\text{vt}} = \left(\int_{\Omega} T(\mathbf{x})^p \, d\Omega \right)^{\frac{1}{p}-1} \int_{\Omega} T(\mathbf{x})^{p-1} \delta T(\mathbf{x}) \, d\Omega, \quad (3.58)$$

where we notice the implicit sensitivity δT is problematic to compute analytically. We use the adjoint method to address this issue wherein we restate Equation(3.47) in its weak form, i.e. we find $T \in \mathcal{H} = \{T \in H^1; T = 0 \text{ on } \partial\Omega\}$ for an H^1 Hilbert space such that

$$- \int_{\Omega} \nabla w(\mathbf{x}) \cdot k(\mathbf{x}) \nabla T(\mathbf{x}) \, d\Omega + \int_{\Omega} w(\mathbf{x}) Q(\mathbf{x}) \, d\Omega = 0 \quad (3.59)$$

for all $w \in \mathcal{H}$. Differentiating the above gives the problem of finding $\delta T \in \mathcal{H}$ satisfying

$$- \int_{\Omega} \nabla w(\mathbf{x}) \cdot \delta k(\mathbf{x}) \nabla T(\mathbf{x}) \, d\Omega - \int_{\Omega} \nabla w(\mathbf{x}) \cdot k(\mathbf{x}) \nabla \delta T(\mathbf{x}) \, d\Omega + \int_{\Omega} w(\mathbf{x}) \delta Q(\mathbf{x}) \, d\Omega = 0 \quad (3.60)$$

for all $w \in \mathcal{H}$. We now add Equation (3.60), i.e. zero, to Equation (3.58) to obtain

$$\begin{aligned} \delta\theta_{\text{vt}} = & \left(\int_{\Omega} T(\mathbf{x})^p \, d\Omega \right)^{\frac{1}{p}-1} \int_{\Omega} T(\mathbf{x})^{p-1} \delta T(\mathbf{x}) \, d\Omega \\ & - \int_{\Omega} \nabla w(\mathbf{x}) \cdot \delta k(\mathbf{x}) \nabla T(\mathbf{x}) \, d\Omega - \int_{\Omega} \nabla w(\mathbf{x}) \cdot k(\mathbf{x}) \nabla \delta T(\mathbf{x}) \, d\Omega + \int_{\Omega} w(\mathbf{x}) \delta Q(\mathbf{x}) \, d\Omega, \end{aligned} \quad (3.61)$$

and notice that upon solving for $w \in \mathcal{H}$ such that

$$\int_{\Omega} \nabla \delta T(\mathbf{x}) \cdot k(\mathbf{x}) \nabla w(\mathbf{x}) \, d\Omega = \left(\int_{\Omega} T(\mathbf{x})^p \, d\Omega \right)^{\frac{1}{p}-1} \int_{\Omega} \delta T(\mathbf{x}) T(\mathbf{x})^{p-1} \, d\Omega \quad (3.62)$$

for all $\delta T \in \mathcal{H}$ we can remove δT from Equation (3.61). Subsequently substituting this w into Equation (3.61) yields

$$\delta\theta_{\text{vt}} = - \int_{\Omega} \nabla w(\mathbf{x}) \cdot \delta k(\mathbf{x}) \nabla T(\mathbf{x}) \, d\Omega + \int_{\Omega} w(\mathbf{x}) \delta Q(\mathbf{x}) \, d\Omega. \quad (3.63)$$

We parameterize \tilde{v} to be piece-wise uniform over the finite element mesh, i.e. each finite element

in Ω is assigned a distinct volume fraction \tilde{v}_i . As such

$$\frac{D\theta_{vt}}{D\tilde{v}_i} = - \int_{\Omega} \nabla w(\mathbf{x}) \cdot \frac{Dk(\mathbf{x})}{D\tilde{v}_i} \nabla T(x) \, d\Omega + \int_{\Omega} w(x) \frac{DQ(\mathbf{x})}{D\tilde{v}_i} \, d\Omega, \quad (3.64)$$

where we note that

$$\frac{Dk}{D\tilde{v}_i} = -q(1 - \tilde{v}_i)^{q-1} (k_0 - \varepsilon_e k_0) \quad (3.65)$$

and

$$\frac{DQ}{D\tilde{v}_i} = \begin{cases} (-c_1 q (1 - \tilde{v}_i)^{r-1} - c_2 (r+1) (1 - \tilde{v}_i)^r) Q_0 & \tilde{v}_i \geq \tilde{v}_U \\ -Q_0 & \tilde{v}_i < \tilde{v}_U \end{cases} \quad (3.66)$$

when using the interpolation schemes in Equations (3.48) and (3.49), i.e. when restricting EVS.

Similarly,

$$\frac{Dk}{D\tilde{v}_i} = q\tilde{v}_i^{q-1} (k_0 - \varepsilon_e k_0) \quad (3.67)$$

and

$$\frac{DQ}{D\tilde{v}_i} = \begin{cases} (c_1 r \tilde{v}_i^{r-1} + c_2 (q+1) \tilde{v}_i^r) Q_0 & \tilde{v}_i \leq \tilde{v}_L \\ Q_0 & \tilde{v}_i > \tilde{v}_L \end{cases} \quad (3.68)$$

when using the interpolation schemes in Equations (3.54) and (3.55), i.e. when restricting ISM.

3.1.2 Mechanical eigenvalues

Another constraint that can be used to identify ISM is derived from an eigenvalue analysis that consists of solving for eigenpairs $(\lambda_j, \mathbf{u}_j)$ ordered such that $\lambda_1 \leq \lambda_2 \leq \dots \leq \lambda_n$ and satisfy

$$\begin{aligned} \nabla \cdot \mathbb{C}(x) [\nabla \mathbf{u}_j(\mathbf{x})] &= \lambda_j \rho(\mathbf{x}) \mathbf{u}_j(\mathbf{x}) \quad \text{for } \mathbf{x} \in \Omega \\ \mathbf{u}_j(\mathbf{x}) &= \mathbf{u}_j(\mathbf{x} + n\mathbf{a}_k) \quad \text{for } n \in \mathbb{Z}, \end{aligned} \quad (3.69)$$

where \mathbb{C} is the fourth-order elasticity tensor, ρ is the mass density, \mathbf{u} is the displacement, Ω is a periodic domain, i.e. a unit cell, \mathbb{Z} is the set of all integers, and \mathbf{a}_k are the lattice vectors. Thus, we are employing periodic boundary conditions to appropriately model the response of our infinitely

periodic structure. We use the SIMP interpolation [91] for the constitutive tensor according to

$$\mathbb{C}(\tilde{v}) = \varepsilon_e \mathbb{C}_0 + \tilde{v}^q (\mathbb{C}_0 - \varepsilon_e \mathbb{C}_0), \quad (3.70)$$

so that we place a stiff material in the solid phase, i.e. $\mathbb{C}(1) = \mathbb{C}_0$ and a weak material in the void phase, i.e. $\mathbb{C}(0) = \varepsilon_e \mathbb{C}_0$, where \mathbb{C}_0 is the elasticity tensor of the solid material. We use the modified SIMP [97] to interpolate the mass density according to

$$\rho(\tilde{v}) = \begin{cases} (c_1 \tilde{v}^r + c_2 \tilde{v}^{r+1}) \rho_0 & \tilde{v} \leq \tilde{v}_L \\ \tilde{v} \rho_0 & \tilde{v} > \tilde{v}_L \end{cases}, \quad (3.71)$$

wherein c_1 and c_2 are given in Equations (3.56) and (3.57), respectively.

We know that $\lambda_j \geq 0$ since the left-hand side operator in Equation (3.69) is positive semi-definite, and we expect 3 zero-valued eigenvalues corresponding to rigid translation, i.e. $\lambda_1 = \lambda_2 = \lambda_3 = 0$. We show in Section 3.2 that we can identify ISM by observing the magnitude of the fourth-smallest eigenvalue. There will be nearly zero-valued eigenvalues λ_j for $j = 4, 5, \dots, n$ when ISM are present, where the lower limit of λ_4 is determined by the selection of ε_e . As such, we estimate the fourth-smallest eigenvalue using a p -norm function

$$\theta_{\text{eig}} = \left(\sum_{i=4}^n \lambda_i^{-p} \right)^{-\frac{1}{p}}, \quad (3.72)$$

and subsequently enforce the optimization constraint

$$\theta_{\text{eig}} \geq \mu_{\text{eig}} \bar{\theta}_{\text{eig}}, \quad (3.73)$$

where $\bar{\theta}_{\text{eig}}$ is computed from Equation (3.72) with the entire domain set to $\tilde{v} = 1$. We use Equation (3.72) rather than $\theta_{\text{eig}} = \lambda_4$ since Equation (3.72) is differentiable even if λ_4 is a degenerate eigenvalue, i.e. even if $\lambda_4 = \lambda_5 \leq \dots \leq \lambda_n$. We necessarily have $\lambda_3 < \lambda_4$ due to the ersatz material

usage and therefore Equation (3.72) is a symmetric polynomial of a distinct set of eigenvalues and hence differentiable [52].

We compute the sensitivity of the eigenvalues λ^j according to

$$\delta\lambda_j = \left(\int_{\Omega} \mathbf{u}_j(\mathbf{x}) \cdot \rho(\mathbf{x}) \mathbf{u}_j(\mathbf{x}) \, d\Omega \right)^{-1} \left(\int_{\Omega} \nabla \mathbf{u}_j(\mathbf{x}) \cdot \delta\mathbb{C}(\mathbf{x}) [\nabla \mathbf{u}_j(\mathbf{x})] \, d\Omega - \lambda_j \int_{\Omega} \mathbf{u}_j(\mathbf{x}) \cdot \delta\rho(\mathbf{x}) \mathbf{u}_j(\mathbf{x}) \, d\Omega \right). \quad (3.74)$$

For our discretization this gives

$$\frac{D\lambda_j}{D\tilde{v}_i} = \left(\int_{\Omega} \mathbf{u}_j(\mathbf{x}) \cdot \rho(\mathbf{x}) \mathbf{u}_j(\mathbf{x}) \, d\Omega \right)^{-1} \left(\int_{\Omega} \nabla \mathbf{u}_j(\mathbf{x}) \cdot \frac{D\mathbb{C}(\mathbf{x})}{D\tilde{v}_i} [\nabla \mathbf{u}_j(\mathbf{x})] \, d\Omega - \lambda_j \int_{\Omega} \mathbf{u}_j(\mathbf{x}) \cdot \frac{D\rho(\mathbf{x})}{D\tilde{v}_i} \mathbf{u}_j(\mathbf{x}) \, d\Omega \right). \quad (3.75)$$

where

$$\frac{D\mathbb{C}}{D\tilde{v}_i} = q\tilde{v}_i^{q-1} (\mathbb{C}_0 - \varepsilon_e \mathbb{C}_0) \quad (3.76)$$

and

$$\frac{D\rho}{D\tilde{v}_i} = \begin{cases} (c_1 r \tilde{v}_i^{r-1} + c_2 (r+1) \tilde{v}_i^r) \rho_0 & \tilde{v}_i \leq \tilde{v}_L \\ \rho_0 & \tilde{v}_i > \tilde{v}_L \end{cases}. \quad (3.77)$$

The derivative of Equation (3.72) is computed as

$$\frac{D\theta_{\text{eig}}}{D\lambda_j} = \left(\sum_{i=4}^M \lambda_i^{-p} \right)^{-\frac{1}{p}-1} (\lambda_j^{-p-1}). \quad (3.78)$$

and the derivative $\frac{D\theta_{\text{eig}}}{D\tilde{v}_i}$ follows from an application of the chain rule.

3.1.3 Self-weight compliance

The periodic VTM presented above is very effective at identifying ISM and EVS. We will see in Section 3.2, however, a lack of ISM does not guarantee a structure is self-supporting. Thus, we propose a self-weight compliance constraint to ensure the unit cell is adequately supported. To do

this we solve for the displacements \mathbf{u}_i resulting from design-dependent body loads in each spatial dimension e_i according to

$$\begin{aligned} \nabla \cdot \mathbb{C}(\mathbf{x}) [\nabla \mathbf{u}_i(\mathbf{x})] + \rho(\mathbf{x}) \mathbf{e}_i &= 0 \quad \text{for } \mathbf{x} \in \Omega \\ \mathbf{u}_i(\mathbf{x}) &= 0 \quad \text{for } \mathbf{x} \in \Gamma_i, \end{aligned} \quad (3.79)$$

where the domain Ω is a single unit cell without periodicity considered and Γ_i the face that is “below” the unit cell, i.e. the face with an outward normal vector of $-\mathbf{e}_i$ where \mathbf{e}_i is a canonical basis vector, cf. Figure 3.4. We again use SIMP [91] to interpolate the constitutive tensor from Equation (3.70) and the modified SIMP [97] to interpolate the mass density from Equation (3.71). After evaluating the displacements \mathbf{u}_i , we evaluate the mean compliance

$$\theta_{\text{swc}} = - \sum_{i=1}^3 \int_{\Omega} \rho(\mathbf{x}) \mathbf{e}_i \cdot \mathbf{u}_i(\mathbf{x}) \, d\Omega. \quad (3.80)$$

The value of θ_{swc} will be small when the structure is fully supported, otherwise it will be very large. Knowing this we enforce the self-weight compliance constraint

$$\theta_{\text{swc}} \leq \mu_{\text{swc}} \bar{\theta}_{\text{swc}}, \quad (3.81)$$

where μ_{swc} is a user-selected constant and $\bar{\theta}_{\text{swc}}$ is computed by Equation (3.80) with $\tilde{\nu} = 1$ prescribed on the entire domain.

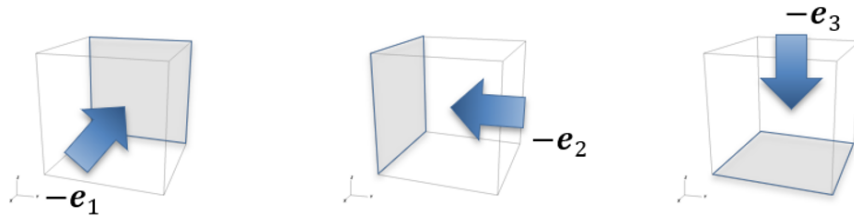


Figure 3.4 Locations (in gray) of essential boundary conditions when computing θ_{swc}

The sensitivity of θ_{swc} is obtained via the adjoint method [19] as

$$\delta\theta_{\text{swc}} = -2 \sum_{i=1}^3 \int_{\Omega} \delta\rho(\mathbf{x}) \mathbf{e}_i \cdot \mathbf{u}_i(\mathbf{x}) \, d\Omega - \sum_{i=1}^3 \int_{\Omega} \nabla \mathbf{u}_i(\mathbf{x}) \cdot \delta\mathbb{C}(\mathbf{x}) [\nabla \mathbf{u}_i(\mathbf{x})] \, d\Omega, \quad (3.82)$$

from which we obtain

$$\frac{D\theta_{\text{swc}}}{D\tilde{\nu}_i} = -2 \sum_{i=1}^3 \int_{\Omega} \frac{D\rho(\mathbf{x})}{D\tilde{\nu}_i} \mathbf{e}_i \cdot \mathbf{u}_i(\mathbf{x}) \, d\Omega - \sum_{i=1}^3 \int_{\Omega} \nabla \mathbf{u}_i(\mathbf{x}) \cdot \frac{D\mathbb{C}(\mathbf{x})}{D\tilde{\nu}_i} [\nabla \mathbf{u}_i(\mathbf{x})] \, d\Omega. \quad (3.83)$$

where $\frac{D\mathbb{C}}{D\tilde{\nu}_i}$ and $\frac{D\rho}{D\tilde{\nu}_i}$ follow from Equations (3.76) and (3.77).

Note that we must again consider an array of 2^d unit cells to ensure that our choice of unit cell does not affect the intent of the constraint function, cf. Figure 3.3. In our numerical examples, however, we will only consider a single unit cell due to the imposed orthorhombic symmetry on the unit cell which eliminates the constraint's dependence on the cell.

3.1.4 Effective stiffness constraints

In addition to the previously discussed EVS, ISM, and self-supporting constraints, we investigate constraints derived from the effective stiffness of our assumed infinite, periodic microstructures. Following classical homogenization theory[17], we first solve a series of cell problems for the characteristic displacements χ^{ij}

$$\begin{aligned} \nabla \cdot \mathbb{C}(\mathbf{x}) \left[\mathbf{E}^{ij} + \nabla \chi^{ij}(\mathbf{x}) \right] &= 0 \quad \text{for } \mathbf{x} \in \Omega \\ \mathbf{u}_j(\mathbf{x}) &= \mathbf{u}_j(\mathbf{x} + n\mathbf{a}_k) \quad \text{for } n \in \mathbb{Z}, \end{aligned} \quad (3.84)$$

where $\mathbf{E}^{ij} \equiv \mathbf{e}^i \otimes \mathbf{e}^j$ is a unit ‘‘test’’ strain defined by basis vectors \mathbf{e}_i and Ω is the periodic unit cell. Akin to Section 3.1.2, we employ periodic boundary conditions. Upon obtaining each unique χ^{ij} , i.e. 6 displacement solutions in 3D, the components of the homogenized stiffness tensor \mathbb{C}^h

are computed according to

$$\mathbb{C}_{ijkl}^h = \frac{1}{|\Omega|} \int_{\Omega} \mathbf{E}^{ij} \cdot \mathbb{C}(\mathbf{x}) \left[\mathbf{E}^{kl} + \nabla \chi^{kl}(\mathbf{x}) \right] d\Omega, \quad (3.85)$$

where $|\Omega|$ is the volume of the unit cell. We evaluate the design sensitivity of \mathbb{C}^h using the adjoint technique[17, 100] according to

$$\delta \mathbb{C}_{ijkl}^h = \frac{1}{|\Omega|} \int_{\Omega} \left(\mathbf{E}^{ij} + \nabla \chi^{ij}(\mathbf{x}) \right) \cdot \delta \mathbb{C}(\mathbf{x}) \left[\mathbf{E}^{kl} + \nabla \chi^{kl}(\mathbf{x}) \right] d\Omega. \quad (3.86)$$

The interpolation of \mathbb{C} from Equation (3.70), and therefore the derivative in Equation (3.76), will be used again here. We will investigate a number of constraint functions that depend explicitly on the components of \mathbb{C}^h .

Bulk modulus

The bulk modulus measures the volume change due to a uniform pressure loading. We express the bulk modulus as a function of the homogenized stiffness tensor according to

$$\kappa(\mathbb{C}) = \frac{1}{\mathbf{I} \cdot \mathbb{C}^{-1} [\mathbf{I}]}, \quad (3.87)$$

noting that we drop the superscript h for brevity and \mathbf{I} is the identity 2-tensor that represents a hydrostatic pressure. The derivative of the bulk modulus with respect to a component of \mathbb{C} is computed as

$$\frac{D\kappa(\mathbb{C})}{D\mathbb{C}_{ijkl}} = \frac{1}{(\mathbf{I} \cdot \mathbb{C}^{-1} [\mathbf{I}])^2} \left(\mathbb{C}^{-1} \frac{D\mathbb{C}}{D\mathbb{C}_{ijkl}} \mathbb{C}^{-1} \right). \quad (3.88)$$

Following our previous conventions we define the bulk modulus constraint

$$\kappa \geq \mu_{\kappa} \bar{\kappa}, \quad (3.89)$$

where $\mu_{\bar{\kappa}}$ is a user-selected constant and $\bar{\kappa}$ is computed by prescribing $\bar{\nu} = 1$ throughout the domain, or equivalently computed for an isotropic solid constituent material from its Young's modulus E and Poisson's ratio ν as $\bar{\kappa} = \frac{E}{3(1-2\nu)}$.

Shear modulus

We will define a shear modulus that is analogous to our bulk modulus definition in Equation (3.87).

To quantify shear stiffness we define a shear stress tensor

$$\mathbf{S} = \frac{1}{\sqrt{3}} \begin{bmatrix} 0 & 1 & 1 \\ 1 & 0 & 1 \\ 1 & 1 & 0 \end{bmatrix} \quad (3.90)$$

and express a “mean” shear modulus

$$\gamma(\mathbb{C}) = \frac{1}{\mathbf{S} \cdot \mathbb{C}^{-1} [\mathbf{S}]}. \quad (3.91)$$

The derivative of the shear modulus with respect to a component of \mathbb{C} is computed from Equation (3.89) with \mathbf{S} replacing \mathbf{I} , i.e.

$$\frac{D\gamma(\mathbb{C})}{D\mathbb{C}_{ijkl}} = \frac{1}{(\mathbf{S} \cdot \mathbb{C}^{-1} [\mathbf{S}])^2} \left(\mathbb{C}^{-1} \frac{D\mathbb{C}}{D\mathbb{C}_{ijkl}} \mathbb{C}^{-1} \right). \quad (3.92)$$

Using the above, we define the shear modulus constraint

$$\gamma \geq \mu_{\bar{\gamma}} \bar{\gamma}, \quad (3.93)$$

where $\mu_{\bar{\gamma}}$ is a user-selected constant and $\bar{\gamma}$ is computed by prescribing $\bar{\nu} = 1$ throughout the domain, or equivalently computed for an isotropic solid constituent material as $\bar{\gamma} = \frac{E}{2(1+\nu)}$.

Anisotropy

We also require our periodic structures to exhibit some degree of isotropy. A number of anisotropy indices have been presented in the literature, including the universal elastic anisotropy index [101] defined by

$$A^U = \frac{k^V}{k^R} + 5 \frac{\gamma^V}{\gamma^R} - 6, \quad (3.94)$$

where the superscripts V and R denote Voigt and Reuss estimates, respectively. These estimates are computed directly from the components of \mathbb{C} [102], and so the sensitivity analysis of A^U is a simple matter of arithmetic that is omitted here. The universal elastic anisotropy index is motivated from the fact that the Voigt and Reuss estimates of bulk and shear modulus are equal when a material is isotropic, thus by measuring the ratio between these estimates it is possible to quantify how close a material is to isotropic. The universal elastic anisotropy index was later extended to compute the distance between the Voigt and Reuss estimates in log-Euclidean space [103] as

$$A^L = \sqrt{\log^2\left(\frac{k^V}{k^R}\right) + 5 \log^2\left(\frac{\gamma^V}{\gamma^R}\right)} \quad (3.95)$$

as an attempt to describe the level of anisotropy more physically. We again omit its trivial sensitivity analysis. Similarly, the distance between a stiffness tensor \mathbb{C} and the closest isotropic tensor [104] can be computed by

$$A^D = \|\log(\mathbb{C}^{\text{iso}}) - \log(\mathbb{C})\|, \quad (3.96)$$

where \mathbb{C}^{iso} is the closest isotropic stiffness tensor to \mathbb{C} in log-Euclidean space. It was proven that

$$\log(\mathbb{C}^{\text{iso}}) = \mathbf{P}^{\text{iso}} \log(\mathbb{C}), \quad (3.97)$$

where the projection \mathbf{P}^{iso} is defined in the original reference [104] and hence we can compute the anisotropy measure as

$$A^{\text{D}} = \|\mathbf{P}^{\text{iso}} \log(\mathbb{C}) - \log(\mathbb{C})\|. \quad (3.98)$$

To use A^{D} in a constraint we must compute its sensitivity with respect to \mathbb{C} . We will define $\mathbb{D} = \mathbf{P}^{\text{iso}} \log(\mathbb{C}) - \log(\mathbb{C})$ and derive the sensitivity as

$$\begin{aligned} \frac{\text{D}A_{\log}}{\text{D}\mathbb{C}} \cdot \mathbb{U} &= \frac{1}{2\|\mathbb{D}\|} \left(\frac{\text{D}}{\text{D}\mathbb{C}} (\mathbb{D} \cdot \mathbb{D}) \right) \cdot \mathbb{U} \\ &= \frac{1}{2\|\mathbb{D}\|} 2\mathbb{D} \cdot \frac{\text{D}\mathbb{D}}{\text{D}\mathbb{C}} [\mathbb{U}] \\ &= \frac{1}{\|\mathbb{D}\|} \left(\left(\frac{\text{D}\mathbb{D}}{\text{D}\mathbb{C}} \right)^T [\mathbb{D}] \right) \cdot \mathbb{U} \end{aligned} \quad (3.99)$$

for an arbitrary 4th-order tensor \mathbb{U} . Using the arbitrariness of \mathbb{U} we obtain

$$\frac{\text{D}A_{\log}}{\text{D}\mathbb{C}} = \frac{1}{\|\mathbb{D}\|} \left(\frac{\text{D}\mathbb{D}}{\text{D}\mathbb{C}} \right)^T [\mathbb{D}]. \quad (3.100)$$

Note that we obtain the simplification using the projection properties

$$\begin{aligned} \left(\frac{\text{D}\mathbb{D}}{\text{D}\mathbb{C}} \right)^T [\mathbb{D}] &= \left(\mathbf{P}^{\text{iso}} \frac{\text{D} \log(\mathbb{C})}{\text{D}\mathbb{C}} - \frac{\text{D} \log(\mathbb{C})}{\text{D}\mathbb{C}} \right)^T [\mathbb{D}] \\ &= - \left(\frac{\text{D} \log(\mathbb{C})}{\text{D}\mathbb{C}} \right)^T [\mathbb{D}] \end{aligned} \quad (3.101)$$

since

$$\begin{aligned} (\mathbf{P}^{\text{iso}})^T [\mathbb{D}] &= (\mathbf{P}^{\text{iso}})^T [\mathbf{P}^{\text{iso}} \log(\mathbb{C}) - \log(\mathbb{C})] \\ &= \mathbf{P}^{\text{iso}} \log(\mathbb{C}) - \mathbf{P}^{\text{iso}} \log(\mathbb{C}) \\ &= \mathbf{0}. \end{aligned} \quad (3.102)$$

Finally, we obtain

$$\frac{\text{D}A_{\log}}{\text{D}\mathbb{C}} = \frac{-1}{\|\mathbb{D}\|} \left(\frac{\text{D} \log(\mathbb{C})}{\text{D}\mathbb{C}} \right)^T [\mathbb{D}]. \quad (3.103)$$

3.2 Constraint capability comparison

A series of example unit cells are presented in Figure 3.5 which highlight the capabilities and limitations of the proposed optimization constraints. Each image displays the solid phase volume fractions of the example unit cell, using the threshold $\tilde{\nu} = 0.5$ for visualization purposes. Additionally, an octant has been clipped from each unit cell to illustrate internal features. Table 3.1 denotes each scalar metric defined in Section 3.1 evaluated on a mesh of 60^3 uniform hexahedral elements. The isotropic base material has a Young's modulus of $E = 1$ and a Poisson's ratio of $\nu = 0.3$. The ersatz void space uses $\varepsilon_e = 10^{-8}$. All PDE's were solved using the open-source, modular finite element method (MFEM) [82] library developed by Lawrence Livermore National Laboratory.

First we consider the uniform, solid microstructure ($\tilde{\nu} = 1$), i.e. unit cell #0. The evaluations of θ_{vt} , θ_{eig} , and θ_{swc} serve as our baseline values, i.e. $\bar{\theta}_{vt}$, $\bar{\theta}_{eig}$, and $\bar{\theta}_{swc}$, respectively. The homogenized κ and γ are verified by comparing them to the analytical expressions $\kappa = \frac{E}{3(1-2\nu)}$ and $\gamma = \frac{E}{2(1+\nu)}$, which is valid since our microstructure is isotropic. Finally, we notice that all 3 anisotropy measures are 0 (within numerical precision), which is expected.

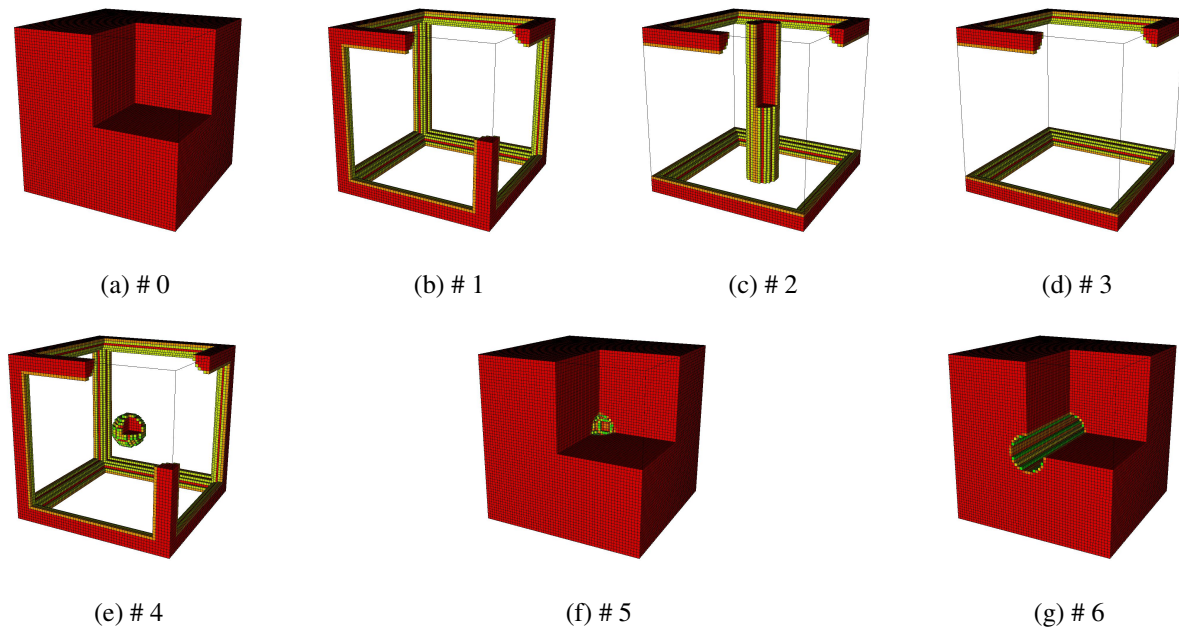


Figure 3.5 Example unit cells for constraint evaluation comparison

Unit cell	θ_{vtv}	θ_{vts}	θ_{eig}	θ_{swc}	κ	γ	A^U	A^L	A^D
# 0	0.0e+00	3.1e-01	1.4e+01	9.2e-01	8.3e-01	3.9e-01	7.8e-16	5.1e-16	9.6e-16
# 1	3.2e-01	5.5e-01	1.4e+00	4.9e-01	1.3e-02	7.1e-04	2.5e+01	4.0e+00	3.4e+00
# 2	3.2e-01	6.9e-01	8.1e-07	1.3e+05	1.1e-02	7.4e-09	2.7e+06	3.0e+01	1.6e+01
# 3	3.2e-01	5.9e-01	1.1e+00	7.3e+04	1.5e-08	6.8e-09	2.9e+06	3.2e+01	1.7e+01
# 4	3.2e-01	3.2e+05	2.2e-06	5.7e+03	1.3e-02	7.1e-04	2.5e+01	4.0e+00	3.4e+00
# 5	3.4e+05	3.1e-01	1.4e+01	9.2e-01	8.2e-01	3.8e-01	2.0e-08	8.8e-09	1.4e-04
# 6	6.9e-01	3.1e-01	1.2e+01	9.2e-01	7.6e-01	3.6e-01	2.6e-03	1.1e-03	5.0e-02

Table 3.1 Constraint Evaluations

Next, we consider a microstructure consisting of orthogonal beams aligned with the Cartesian axes, denoted as unit cell #1. This unit cell is presented as an example of an acceptable design; it is self-supporting, exhibits reasonable stiffness in all directions, and does not have EVS or ISM. Moving left to right across Table 3.1 we see that $\theta_{\text{vtv}} = 1.03 \bar{\theta}_{\text{vt}}$, while $\theta_{\text{vts}} = 1.77 \bar{\theta}_{\text{vt}}$. Both of these values would be acceptable if μ_{vt} was selected in the range of 4-10 as recommended [74]. Thus, the VTM constraints would correctly indicate that neither ISM nor EVS exist in the microstructure. We notice that $\theta_{\text{eig}} \approx 10^{-1} \bar{\theta}_{\text{eig}}$ and we actually see a smaller self-weight compliance than our baseline structure. The homogenized κ and γ are slightly lower than the baseline microstructure, but nonetheless we have non-zero bulk and shear stiffness. The anisotropy measures all predict a moderate amount of anisotropy. In summary, all of the constraints behave exactly as we desire.

If we consider the effect of moving the vertical rods from unit cell #1 so they do not intersect with the horizontal sets of rods, we arrive at unit cell #2. Table 3.1 reveals that $\theta_{\text{vtv}} = 1.03 \bar{\theta}_{\text{vt}}$, correctly communicating a lack of EVS. It would be fair at this point to suspect that θ_{vts} could rise dramatically since the vertical rods are not in contact with the horizontal rods. However, we see that $\theta_{\text{vts}} = 2.23 \bar{\theta}_{\text{vt}}$. This can be understood by recognizing that the rods are infinitely long, under the infinite periodicity assumption. Thus, we have our first constraint limitation; the VTM identifies only those ISM enclosed by the unit cell, i.e. it does not ensure self-supporting structures. Fortunately, we have constraints that can identify these circumstances. Namely, the two functions $\theta_{\text{eig}} \approx 10^{-7} \bar{\theta}_{\text{eig}}$ and $\theta_{\text{swc}} \approx 10^5 \bar{\theta}_{\text{swc}}$ both identify that unit cell # 2 is not self-supporting. Interestingly, we see that κ from unit cell #2 is similar to that of unit cell #1 demonstrating that disconnected rods do not adversely affect the ability to support a pressure load. However, $\gamma \approx 10^{-8} \bar{\gamma}$ demonstrating

almost no resistance to a shear load. As expected, all anisotropy indices show stark increases, but A^L and A^D show much smaller increases than A^U due to their dependencies on the logarithm.

Unit cell #3 is similar to #1 and #2, however the vertical rods have been removed. This example was contrived to illustrate a potential pitfall of θ_{eig} . We notice that $\theta_{\text{eig}} \approx 10^{-1}\bar{\theta}_{\text{eig}}$ even though it is clear that the structure is disconnected. This behavior is due to the fact that all of the solid phase material in the unit cell is connected, thus we have only 3 zero-valued eigenvalues. This non self-supporting structure is identified, however, by noting that $\theta_{\text{swc}} \approx 10^5\bar{\theta}_{\text{swc}}$. Alternatively, it is identified by noting that $\kappa \approx 0$ and $\gamma \approx 0$, while the isotropy indices increase significantly. As seen here, a constraint on bulk stiffness, shear stiffness, or anisotropy could be used in conjunction with θ_{eig} to ensure a self-supporting structure.

The strengths of our ISM constraints are demonstrated with unit cell #4. The small sphere of floating material is easily identified as $\theta_{\text{vts}} \approx 10^6\bar{\theta}_{\text{vt}}$, $\theta_{\text{eig}} \approx 10^{-7}\bar{\theta}_{\text{eig}}$, and $\theta_{\text{swc}} \approx 10^3\bar{\theta}_{\text{swc}}$. Each of these metrics provides a clear signal that an ISM exists. As expected, κ , μ , and all of the anisotropy indices return the same values as their corresponding evaluations on unit cell #1, since the floating sphere has no effect on the homogenized constitutive tensor.

Finally, the effectiveness of θ_{vtv} is demonstrated with unit cells #5 and #6. The void space in unit cell #6 is acceptable since support material or pre-sintered powder could be removed, whereas the void space in unit cell #5 is unacceptable. The VTM is able to distinguish these cases as $\theta_{\text{vtv}} \approx 10^6\bar{\theta}_{\text{vt}}$ for unit cell #5 whereas $\theta_{\text{vtv}} = 2.23\bar{\theta}_{\text{vt}}$ for unit cell #6.

The results presented in Table 3.1 elucidate the capabilities and limitations of our constraints such that guidelines can be proposed for combinations of constraints employed in a TO framework to ensure manufacturable designs. Most directly, if the manufacturing process cannot handle EVS, then a θ_{vtv} constraint should be enforced. The simplest technique to ensure self-supporting structures is to enforce the θ_{swc} constraint. The downside, however, is that the stiffness cannot be explicitly tuned via θ_{swc} . If the designer seeks to tune the level of bulk or shear stiffness, then κ or γ constraints, respectively, are required. In many cases these stiffness constraints are sufficient to remove unsupported material since ISM do not add stiffness to the structure, however, ISM are not

explicitly forbidden. Because of this the κ or γ constraints should be augmented with either a θ_{vts} , θ_{eig} , or θ_{swc} constraint. Finally, if isotropy is required for a particular application, then any of the proposed anisotropy constraints should be enforced.

The choice of which combination of constraints to enforce may also be dictated by computational expense. The VTM and self-weight compliance problems require an array of 2^d unit cells, although the VTM governing PDE is a scalar problem whereas the self-weight compliance PDE is a vector problem. If the unit cell exhibits orthorhombic symmetry, the self-weight compliance computations can be performed over a single unit cell whereas the VTM always requires an array of 2^d unit cells. The mechanical eigenvalue problem in general requires a single unit cell domain, but the mesh can be reduced to an octant for cells with orthorhombic symmetry [105]. Also, κ , γ , and the anisotropy measures are derived from the same homogenized stiffness tensor, thus only one homogenization computation is required over a single unit cell, or over an octant when unit cells exhibit orthorhombic symmetry [105]. To conclude, a designer should select a combination of constraints that ensures designs are viable based on the desired manufacturing process, whether stiffness tuning is required, and whether isotropy is desired. Then, the computational cost should be considered based on the symmetry of the unit cell. The computational cost of the constraints may be somewhat mitigated if the PDE solutions, e.g. the eigenvalues or the homogenized stiffness tensor, are required for other aspects of the TO framework since the scalar quantities are much cheaper to compute than the PDE solutions.

3.3 Optimization test problem

We now demonstrate the effectiveness of the proposed constraints and point out their capabilities and limitations on a simple test problem. Consider a cubic unit cell of side length a centered at the origin with imposed orthorhombic symmetry, uniformly discretized by 60^3 voxels. The 30^3 voxel volume fractions in the octant symmetry cell serve as the design parameters. The length scale is controlled by applying the symmetric, periodic cone filter described in Section 2.1.5 with a filter radius of $0.05a$. In all cases, the initial design is uniform with $\tilde{\nu} = 0.5$. A SIMP exponent of

$q = 3$ and a modified SIMP exponent of $r = 6$ are used for the VTM, eigenvalue, and self-weight compliance constraints. A SIMP exponent of $q = 4$ is used for the homogenized-based constraints, i.e. bulk modulus, shear modulus, and isotropy constraints. The modified SIMP volume fraction boundaries are $\tilde{v}_L = 0.2$ and $\tilde{v}_U = 0.8$, and the ersatz void phase uses $\varepsilon_e = 10^{-8}$. All optimization problems were solved with the open-source, interior point optimizer (IPOPT) [95].

3.3.1 Virtual temperature method for EVS identification

Consider the optimization problem

$$\min_{\tilde{v}} \quad \theta_{\text{EVS}} = \sum_{i=1}^{N_{\text{voxel}}} \begin{cases} 1 - \tilde{v}_i & r_i \geq r_0 \\ \tilde{v}_i & r_i < r_0 \end{cases} \quad (3.104)$$

subject to $0 \leq \tilde{v}_i \leq 1$,

where r_i is the distance from the voxel i centroid to the origin. The solution is a solid unit cell with a hollow sphere removed from the center, cf. Fig. 3.6. The resulting structure is problematic due to the region of EVS. To address this issue we again solve Equation (3.104) with the Equation (3.53) constraint using the material interpolations from Equations (3.48) and (3.49). A series of optimal designs for various values of μ_{vTV} are presented in Figure 3.7. We see that for $\mu_{\text{vTV}} = 25.0$, a channel of void space is formed effectively eliminating the EVS. For $\mu_{\text{vTV}} = 12.0$, a channel with two forks appears, and finally for $\mu_{\text{vTV}} = 6.0$, channels are created in all 3 dimensions. Thus, any of the

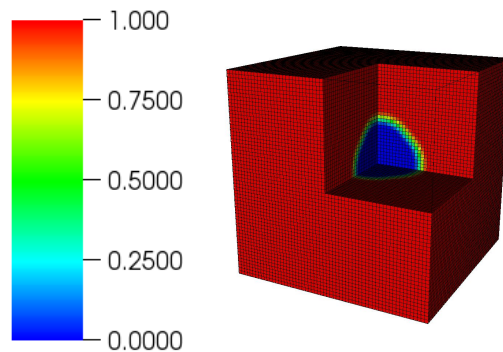


Figure 3.6 Optimal \tilde{v} solutions for θ_{EVS}

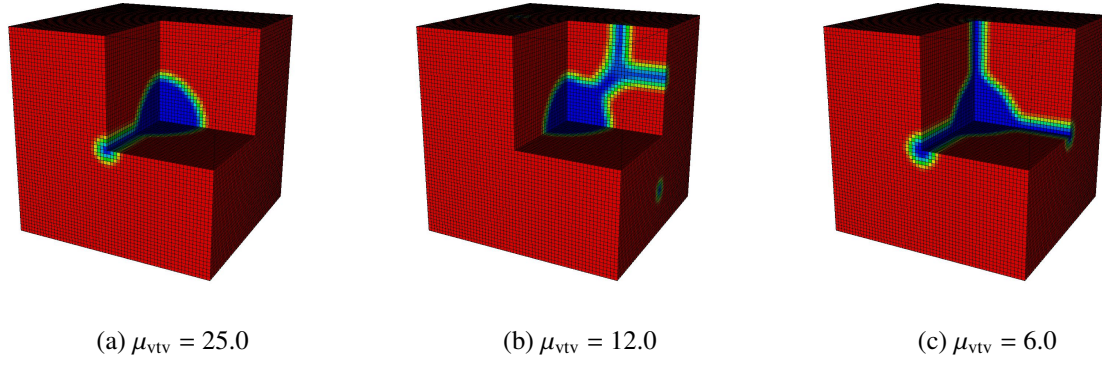


Figure 3.7 Optimal \tilde{v} solutions for θ_{EVS} with θ_{vTV} constraint

selected values of μ_{vTV} eliminate the EVS. A trade-off exists between “how enclosed” the sphere is and the optimal value of the objective function, thus proper selection of μ_{vTV} will certainly be problem specific.

3.3.2 Virtual temperature method for ISM identification

Now we consider the optimization problem

$$\min_{\tilde{v}} \quad \theta_{\text{ISM}} = \sum_{i=1}^{N_{\text{voxel}}} \begin{cases} 1 - \tilde{v}_i & r_i \leq r_0 \\ \tilde{v}_i & r_i > r_0 \end{cases} \quad (3.105)$$

subject to $0 \leq \tilde{v}_i \leq 1$.

The result is a unit cell consisting of a floating sphere at the origin, cf. Fig. 3.8. Throughout Section 3.3.2 only volume fractions satisfying $\tilde{v} > 0.5$ are plotted for visualization purposes. The

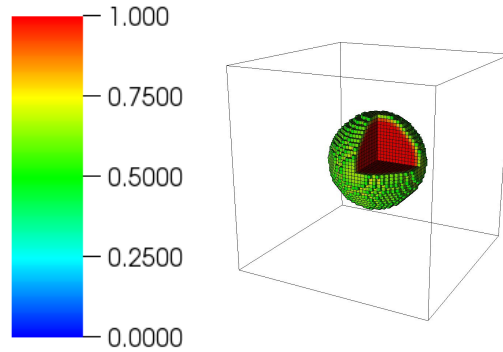


Figure 3.8 Optimal \tilde{v} solutions for θ_{ISM}

resulting structure is problematic due to the ISM. To address this issue we again solve Equation (3.105) with the Equation (3.53) constraint using the material interpolations from Equations (3.54) and (3.55). A series of optimal designs for various values of μ_{vts} are presented in Figure 3.9. We see very similar results to those in Section 3.3.1. For $\mu_{\text{vts}} = 25.0$, a beam of solid material is formed effectively eliminating the ISM. For $\mu_{\text{vts}} = 12.0$, a beam with two forks appears, and finally for $\mu_{\text{vts}} = 6.0$, beams are created in all 3 dimensions. Thus, any of the selected values of μ_{vts} eliminate ISM and adjusting the choice of what μ_{vts} value to use is problem dependent. A notable downside to this constraint is that we cannot guarantee the periodic structure is self-supporting, as evidenced by the $\mu_{\text{vts}} = 25.0$ and 12.0 designs, which do not have stiffness in all directions.

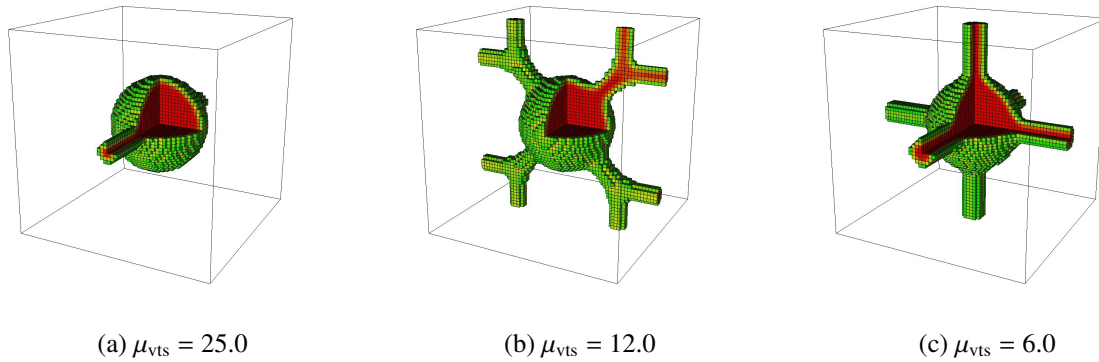


Figure 3.9 Optimal $\tilde{\nu}$ solutions for θ_{ISM} with θ_{vts} constraint

3.3.3 Eigenvalue constraint for ISM identification

To demonstrate the eigenvalue constraint we solve the optimization problem in Equation (3.105) subject to the Equation (3.73) constraint. Optimal structures are presented in Figure 3.10 for various values of μ_{eig} . For $\mu_{\text{eig}} = 0.03$, the ISM is effectively removed by adding thin rod-like features, which become slightly larger for $\mu_{\text{eig}} = 0.10$. However, neither of these designs are self-supporting. If we increase to $\mu_{\text{eig}} = 0.15$, we remove the ISM and obtain a self-supporting structure. In summary, we observe similar behavior between the mechanical eigenvalue constraint and the ISM constraint in Section 3.3.2. For certain values of μ_{eig} we can remove the ISM without generating

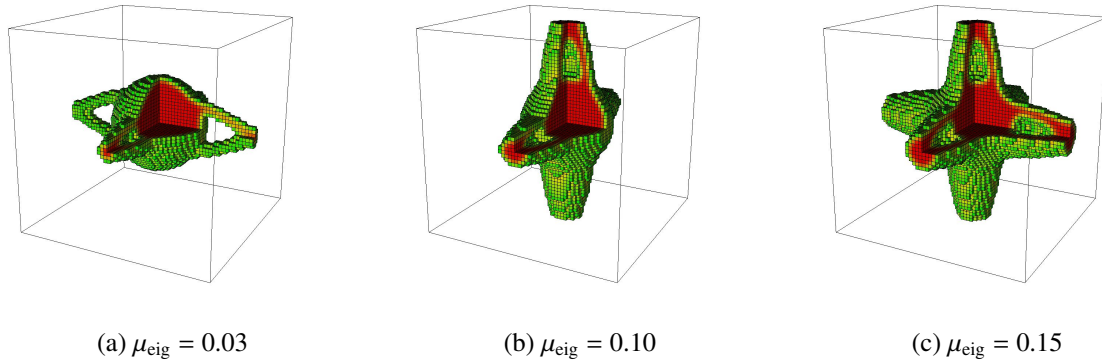


Figure 3.10 Optimal \tilde{v} solutions for θ_{ISM} with θ_{eig} constraint

self-supporting structures. The appropriate value of μ_{eig} is again problem dependent.

3.3.4 Self-weight compliance constraint for ISM identification

We demonstrate the self-weight compliance constraint by solving the optimization problem in Equation (3.105) subject to the Equation (3.81) constraint. Optimal structures are presented in Figure 3.11 for various values of μ_{swc} . We immediately notice that this constraint yields similar results for the three presented values of μ_{swc} . A slight difference appears in the thickness of the supporting beams, but the topology is identical in all cases. Most importantly, all three designs are fully self-supporting. Thus, we expect that the appropriate μ_{swc} value is less problem dependent. The downsides of this constraint are its computational expense and its inability to tune stiffness. The latter concern is addressed in the next section.

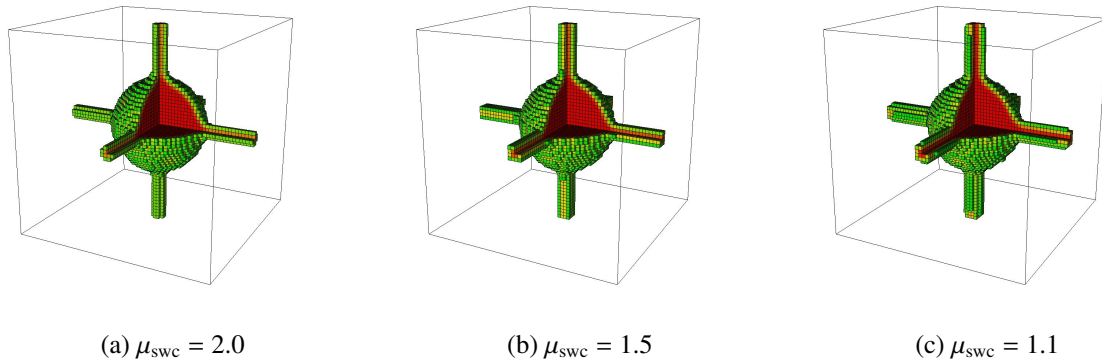


Figure 3.11 Optimal \tilde{v} solutions for θ_{ISM} with θ_{swc} constraint

3.3.5 Effective property constraints

If a design requires a particular level of stiffness or isotropy, effective property constraints derived from a homogenization analysis may be employed. We investigate a few possibilities here. First, we solve the Equation (3.105) optimization problem subject to the Equation (3.89) constraint. Optimal structures for various values of μ_κ are presented in Figure 3.12. As expected, the features become larger as μ_κ is increased, and in all cases we have stiffness in all directions. The optimal structures are fairly intuitive considering that bulk modulus measures resistance to pressure loads.

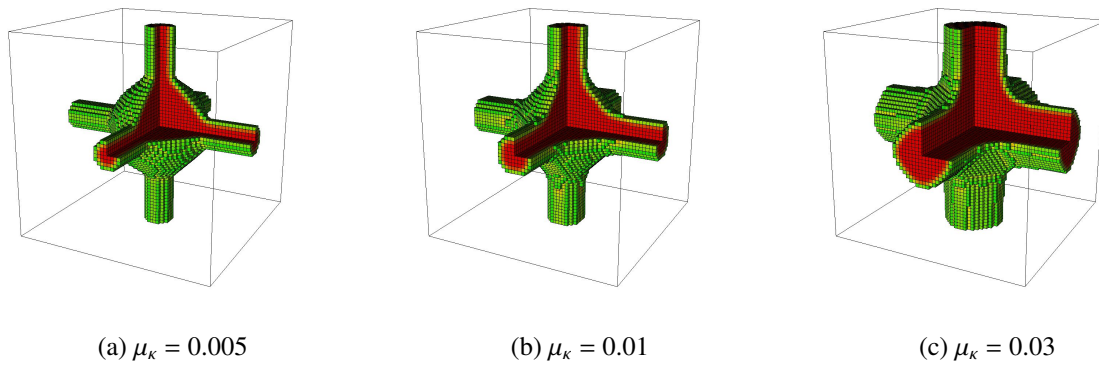


Figure 3.12 Optimal $\tilde{\nu}$ solutions for θ_{ISM} with θ_κ constraint

Similarly, we solved the Equation (3.105) optimization problem subject to the Equation (3.93) constraint. Again, the features become larger as μ_γ is increased, and in all cases we have stiffness in all directions. The structures in Figure 3.13 are slightly more complicated than the structures in Figure 3.12, which is apparently needed to resist shear loads.

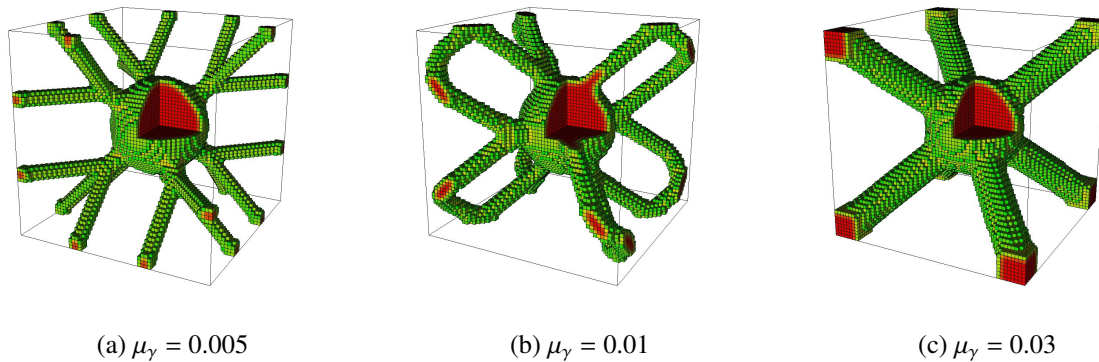


Figure 3.13 Optimal $\tilde{\nu}$ solutions for θ_{ISM} with θ_γ constraint

We have guaranteed through our definitions of κ and γ that enforcement of Equation (3.89) or (3.93) constraints yields structures with stiffness in all directions. However, no consideration is made with respect to isotropy. If isotropy is desired we, e.g., augment the bulk modulus constraint with a constraint on A^U , A^L , or A^D , cf. Figures 3.14, 3.15, and 3.16. We obtain very similar structures when constraining A^U and A^L , which is not surprising since they are both derived from Voigt and Reuss stiffness estimates.

It is expected that these three constraints yield similar results since they are measuring the same type of behavior. Thus, we do not give preference to any of the anisotropy measures, although ease of implementation may favor A^U or A^L over A^D .

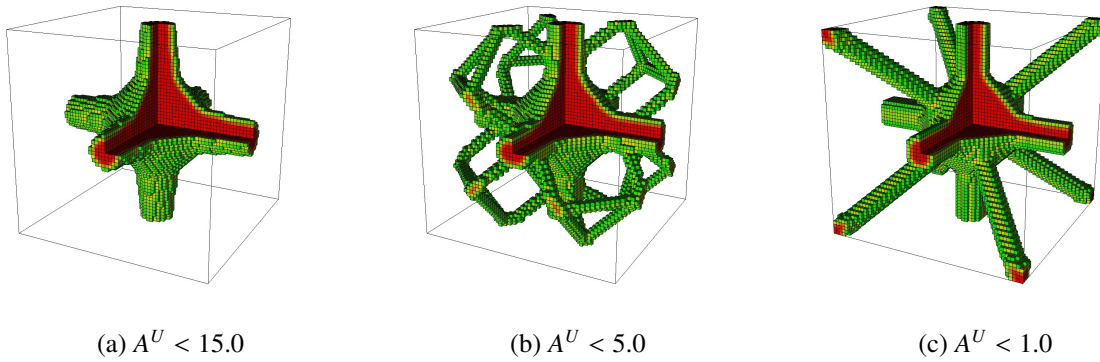


Figure 3.14 Optimal \tilde{v} solutions for θ_{ISM} with θ_κ ($\mu_\kappa=0.01$) and A^U constraints

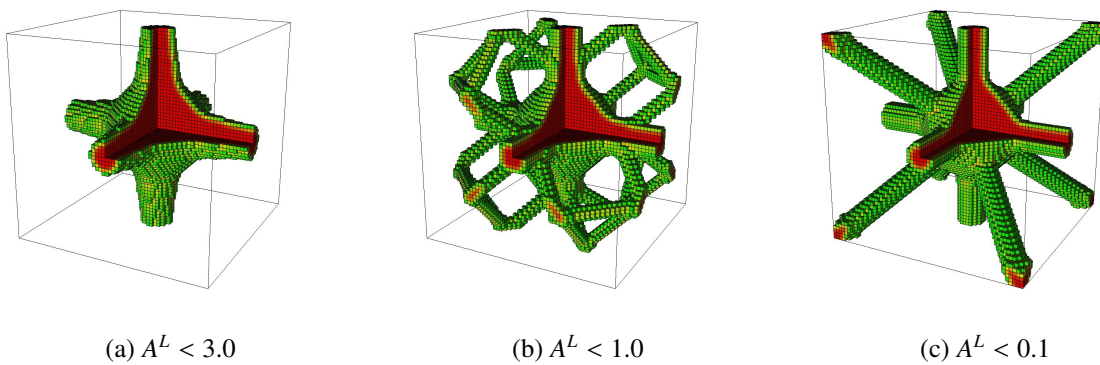


Figure 3.15 Optimal \tilde{v} solutions for θ_{ISM} with θ_κ ($\mu_\kappa=0.01$) and A^L constraints

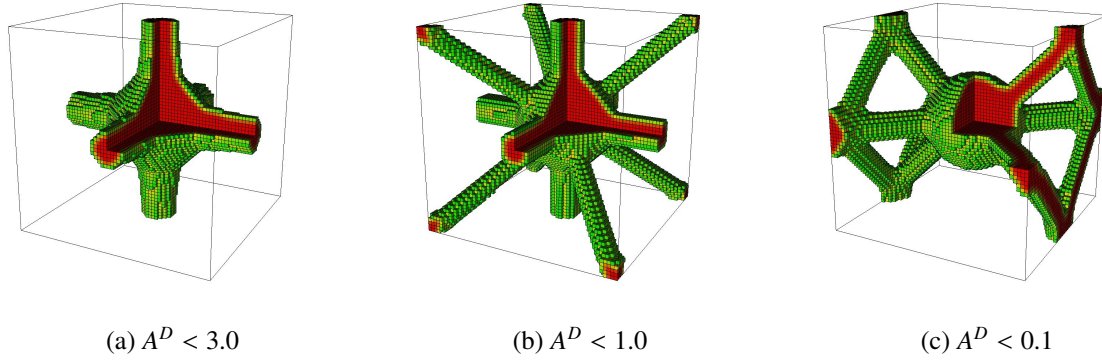


Figure 3.16 Optimal \tilde{v} solutions for θ_{ISM} with θ_κ ($\mu_\kappa=0.01$) and A^D constraints

3.4 Photonic crystal design with manufacturing constraints

The constraints formulated in Section 3.1 are used to design photonic crystals for complete bandgaps. The topology optimization capability from Chapter 2 is augmented here by imposing design constraints to resolve deficiencies in our previous photonic crystal designs that were not manufacturable or self-supporting. Note that throughout Section 3.4 the volume fractions have been thresholded such that $\tilde{v} \geq 0.5$ is considered solid material, whereas $\tilde{v} < 0.5$ is considered void space in the dispersion analyses.

3.4.1 Removal of EVS

Two designs from Chapter 2 with complete 3D bandgaps displayed EVS. We resolve this design flaw via the VTM. Figure 3.17a displays the unconstrained optimal bandgap structure; the left-most image displays the solid material, while the middle image displays the complement, i.e. the void space. We immediately notice a disconnected void space region causing EVS. The dispersion plot reveals a 17.40% bandgap-midgap ratio. We re-solve the optimization problem enforcing the Equation (3.53) constraint with $\mu_{vTV} = 6.0$ to obtain the design depicted in Figure 3.17b. The constrained design is quite similar to the unconstrained design, however, small channels have formed causing the void space to be simply connected. Thus, support material or pre-sintered powder could be removed from the design [74]. There is a slight reduction in the bandgap-midgap ratio, i.e. 16.18% vs. 17.40%, but this difference is small considering that the previous design was not

manufacturable.

Another problematic 3D bandgap design from Chapter 2 is pictured in Figure 3.18. The design exhibited a bandgap-midgap ratio of 12.73%, however a region of EVS is present. Enforcing the Equation (3.53) constraint with $\mu_{\text{vIV}} = 4.0$ produces the design depicted in Figure 3.18b. Again, we see the formation of small channels causing the void space to be simply connected. The bandgap-midgap ratio is reduced to 12.07%, but we again have produced a manufacturable structure.

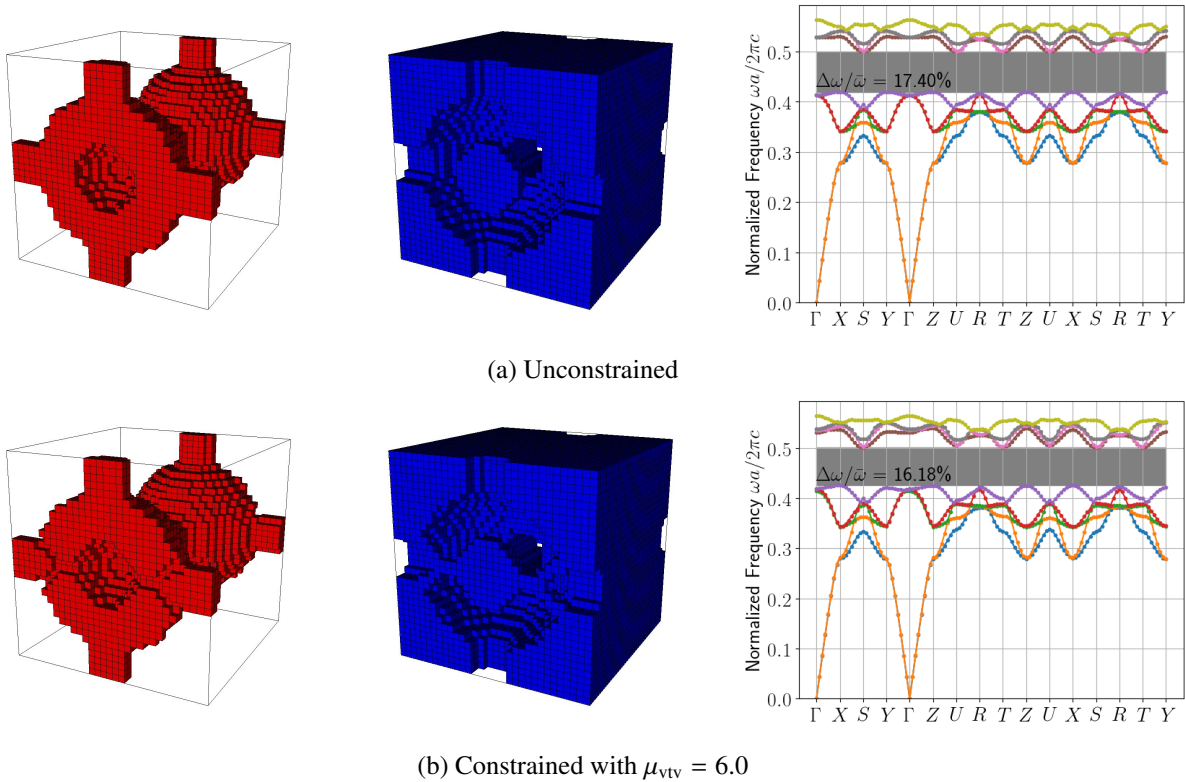


Figure 3.17 Applying θ_{vIV} constraint to remove EVS from mode 5-6 bandgap structure

3.4.2 Removal of ISM

The bandgap structure depicted in Figure 3.19a from Chapter 2, exhibits ISM. The optimization problem is re-solved with a variety of constraints to prevent ISM. First, the VTM Equation (3.53) constraint is enforced. The resulting structure depicted in Figure 3.19b has a slightly smaller bandgap, however, something interesting has occurred. The topology of the structure has changed such that both the ISM and EVS present in the original design are removed. Interestingly, the

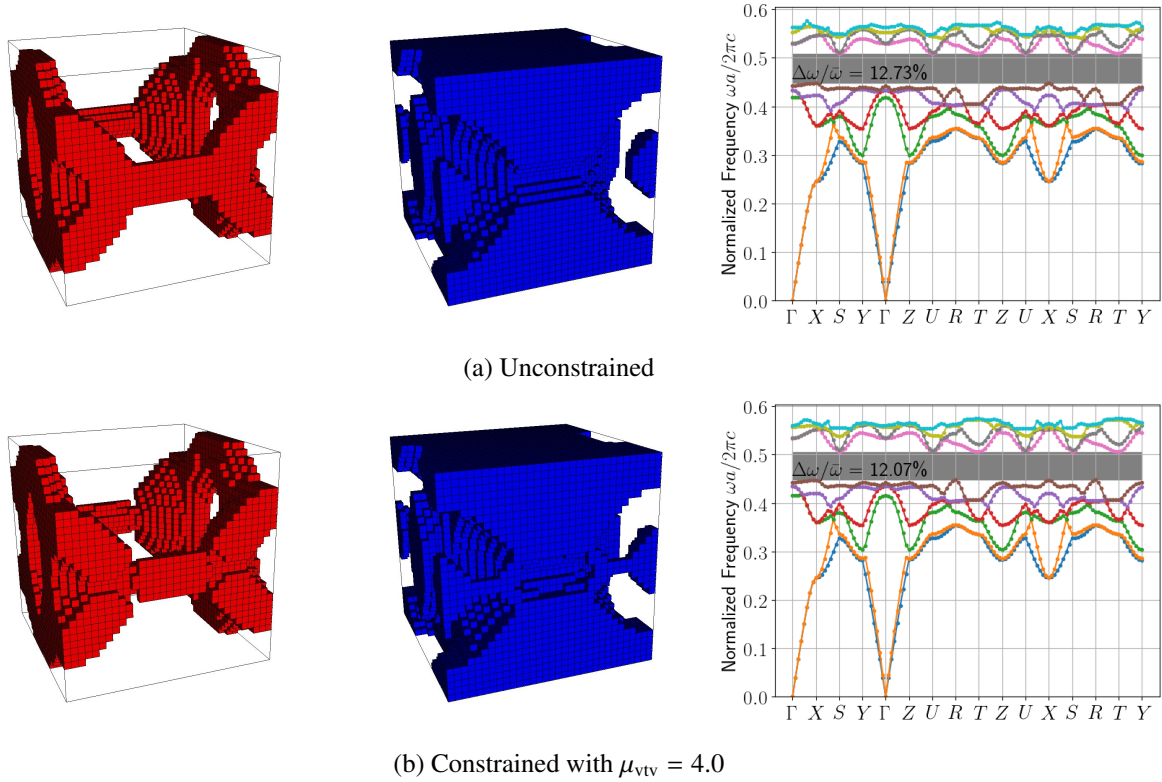


Figure 3.18 Applying θ_{vtv} constraint to remove EVS from mode 6-7 bandgap structure

designs illustrated in Figures 3.19c and 3.19d, obtained via enforcement of the self-weight compliance and shear modulus constraints, respectively, outperform the unconstrained design. It appears that the constrained optimizations found a better local minima than the unconstrained. This behavior should not be expected in general, but it is an important finding nonetheless. The downside to the designs pictured in Figures 3.19c and 3.19d is that EVS remains, which is not surprising since EVS is not strictly forbidden in the optimization formulations. This point is further addressed in Section 3.4.4.

3.4.3 Requirement of self-supporting structure

An optimized structure from Chapter 2 with a complete 2D bandgap is not self-supporting. Specifically, the design, pictured in Figure 3.20a, is not self-supporting as it consists of two separate solid regions. To alleviate this issue we first re-solved the problem while enforcing the Equation (3.73) mechanical eigenvalue constraint. The optimized design shown in Figure 3.20b is similar to the

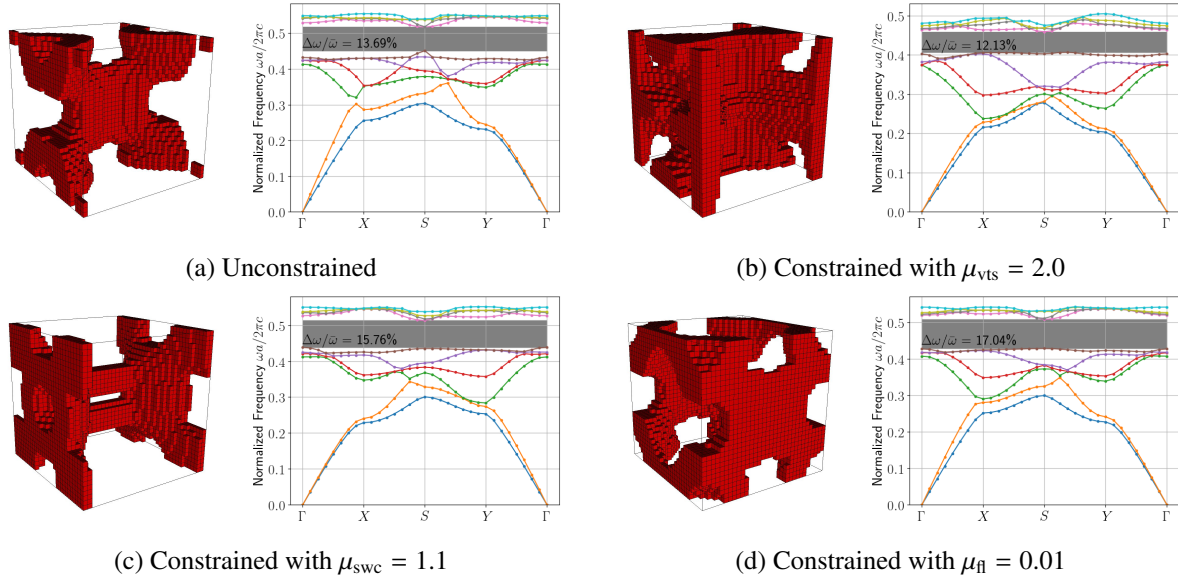


Figure 3.19 Applying various constraints to remove ISM

unconstrained version, but additional features have been added so that the structure is fully self-supporting. The bandgap performance decreases slightly, but the design is now manufacturable. We next enforced the Equation (3.81) self-weight compliance constraint. The optimal structure seen in Figure 3.20c is quite different from the unconstrained design, and the bandgap performance is significantly reduced. All is not lost, however, as the structure is fully self-supporting and still exhibits a complete bandgap. Finally, we enforced the Equation (3.93) shear modulus constraint. The resulting optimal structure appearing in Figure 3.20d is similar to the Figure 3.20b design in that additional features have been added, however, the performance is better. It appears the shear modulus constrained design is the best choice of the presented designs as it results in the highest-performing manufacturable structure. We want to emphasize that these results are just examples proving the effectiveness of the constraints and that more exhaustive studies may lead to different conclusions.

3.4.4 Manufacturable photonic crystals

In order to manufacture our photonic crystals they must neither exhibit EVS nor ISM, i.e. it is not enough to consider them separately. To this end, we reconsidered the design problems addressed in

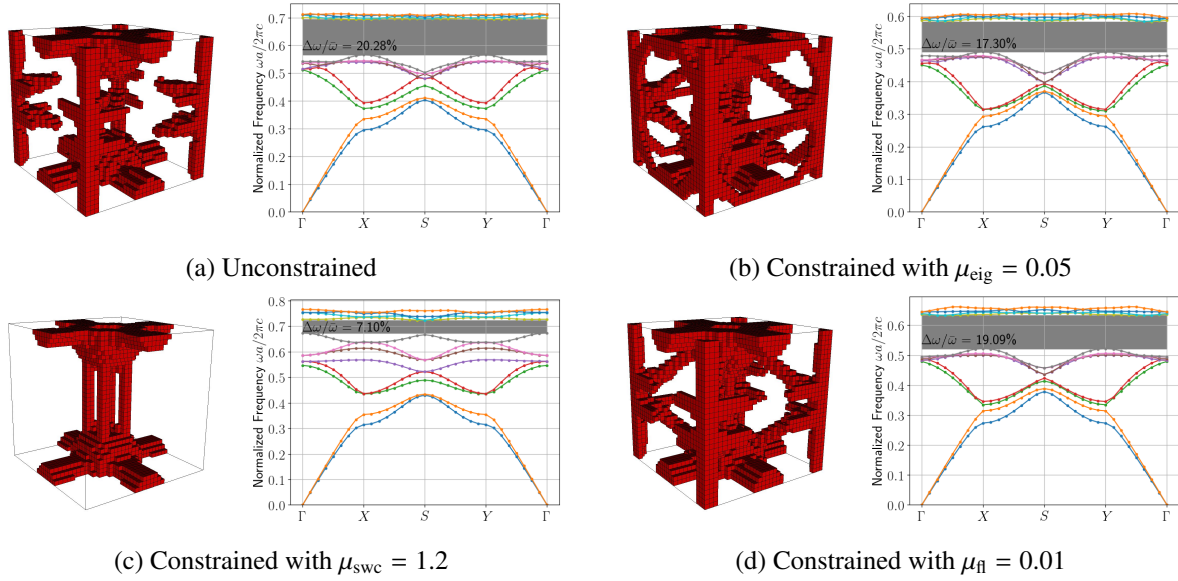


Figure 3.20 Applying various constraints to ensure structures are self-supporting

Sections 3.4.2 and 3.4.3. We began by optimizing the 2D bandgap-midgap ratio between modes 6 and 7 with a bulk modulus constraint to ensure stiffness and a VTM constraint to remove EVS. The resulting constrained structure is compared to the original unconstrained structure in Figure 3.21. Notice that both the ISM and EVS have been removed from the design, while simultaneously improving the bandgap performance.

Similarly, we optimized the 2D bandgap-midgap ratio between modes 8 and 9 with a shear modulus constraint to ensure stiffness and a VTM constraint to remove EVS. The resulting design, pictured in Figure 3.22b, is quite different from its unconstrained counterpart illustrated in Figure 3.22a. Both ISM and EVS have been eliminated in the constrained design which is also self-supporting. Again we emphasize that although the bandgap-midgap ratio is reduced from 20.28% to 19.28%, the new design is manufacturable.

3.5 Photonic bandgap design with tunable bulk modulus

If a designer seeks a photonic crystal with a desired stiffness, the bulk modulus and shear modulus constraints should be considered. To demonstrate this capability, a series of bandgap optimizations are performed with various minimum bulk modulus constraints. At each constraint value, 20

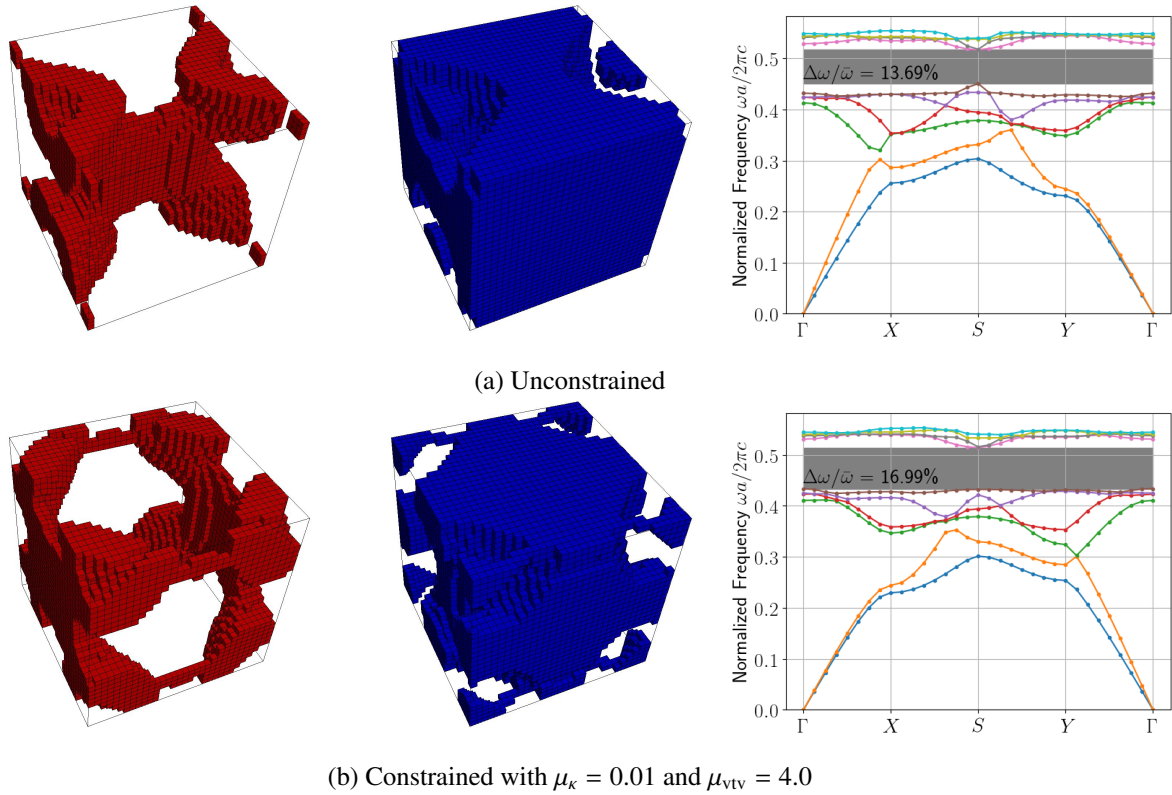


Figure 3.21 Applying κ and VTM constraints to ensure structures are manufacturable

random initial designs were used from which the best resulting optimized design is selected.

Figure 3.23 plots the optimal bandgap-midgap ratio for a complete 2D bandgap between modes 5 and 6 against the minimum bulk modulus.

The best of the 20 optimized designs is pictured near its corresponding data point; the shaded region under the curve indicates the feasible design space. We see a roughly inverse linear relationship between our two quantities of interest and note that $\kappa \approx 0.2$ is the largest bulk stiffness we can generate with a complete bandgap. This plot allows designers to visualize the trade-off between bandgap and bulk stiffness performance. It is interesting to note that enforcing a minimum bulk modulus of $\kappa \geq 0.025$ actually produced a better performing bandgap structure than optimizing for bandgap without considering κ ; evidenced by the non-monotonicity of the plot in Figure 3.23. Since there are many local minima in the designs space we cannot hope to capture the global minimum with only 20 initial designs and thus we should interpret the shaded region as an approximation of the feasible design space.

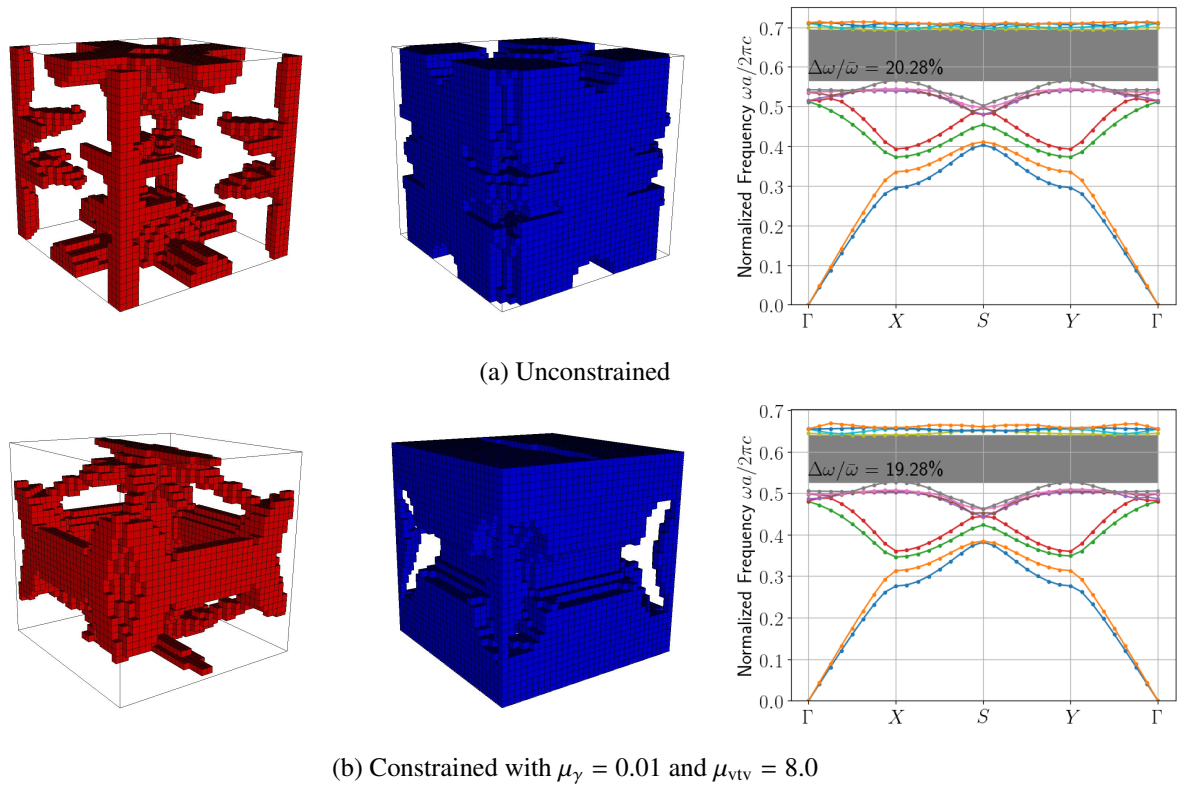


Figure 3.22 Applying γ and VTM constraints to ensure structures are manufacturable

We repeat the Figure 3.23 study, but now design for complete 3D bandgaps between modes 5 and 6. The results, pictured in Figure 3.24, present a roughly inverse linear relationship between the two quantities of interest and note that $\kappa \approx 0.12$ is the largest bulk stiffness we can generate with a complete bandgap. As expected, the volume fraction increases with κ in Figure 3.24, but the topology does not change in contrast to the Figure 3.23 designs.

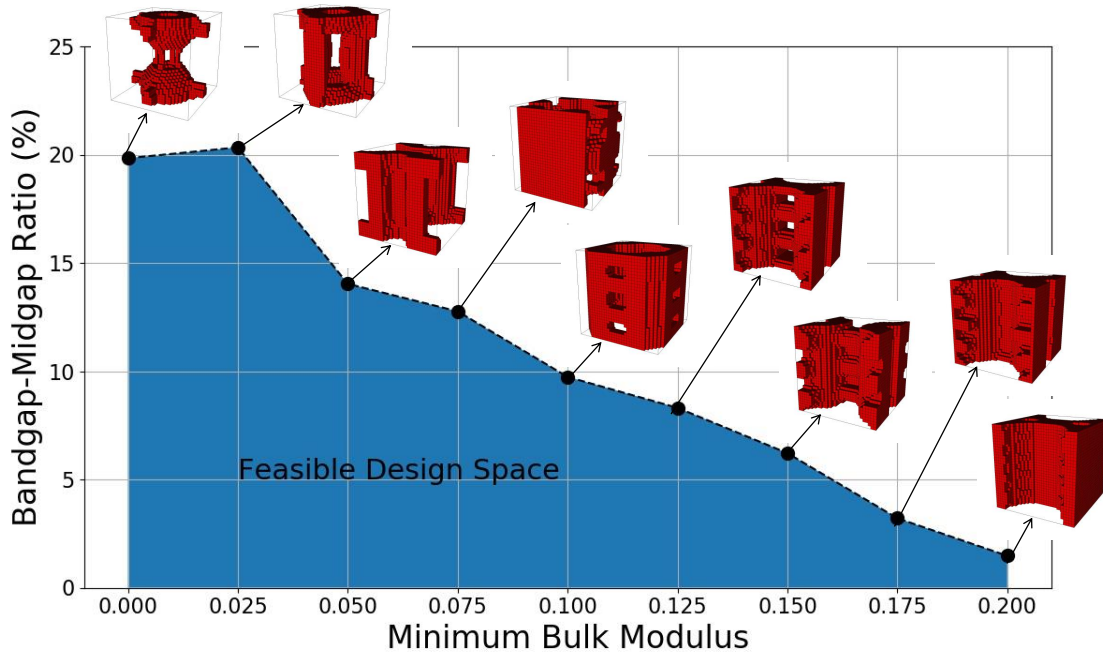


Figure 3.23 2D Bandgap-midgap ratio θ_ω vs. bulk modulus κ

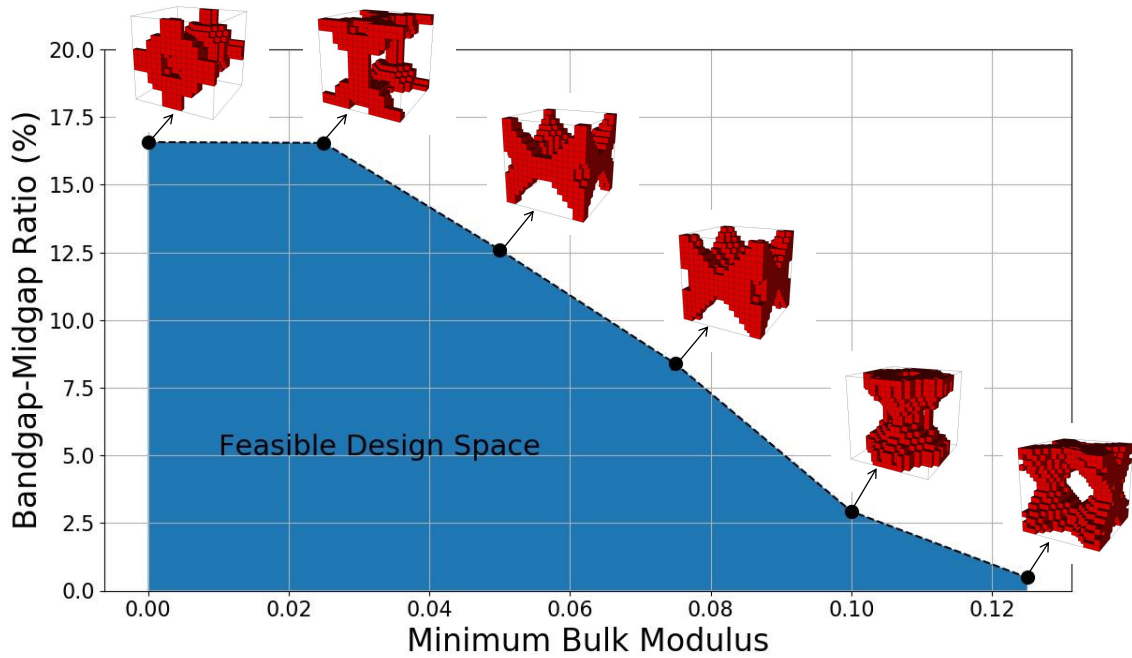


Figure 3.24 3D Bandgap-midgap ratio θ_ω vs. bulk modulus κ

3.6 Conclusions

Topology optimization of phononic/photonic crystals often generates structures that are not manufacturable due to EVS and ISM. Additionally, they often exhibit poor stiffness. We have suggested a series of constraints which can be used to enforce fully-connected, manufacturable structures.

The virtual temperature method is used to prevent EVS and extended to prevent ISM. Further, we adapted the VTM to periodic structures such that constraint behavior is invariant with respect to unit cell selection. A mechanical eigenvalue constraint has been proposed to ensure fully-connected structures while the proposed self-weight compliance constraint ensures self-supporting structures. We also studied the effect of homogenization-based constraints on the bulk and shear moduli to ensure desired stiffness and remove ISM, although the latter claim is not guaranteed. Finally, the efficacy of three proposed isotropy constraints have been demonstrated.

The performance of each constraints was demonstrated on contrived test cases and on the design of photonic crystals. We generated 3D structures with complete 2D and 3D bandgaps that were self-supporting and had required levels of stiffness. The trade-off between photonic bandgap and bulk modulus was investigated to generate an approximation of the feasible design space.

It is imperative to use the VTM to prevent EVS if the AM process used to manufacture the designs requires support material or powder. We suggest employing a bulk and/or modulus constraint to ensure a desired degree of stiffness. Augmenting a stiffness constrained formulation with a mechanical eigenvalue constraint or the VTM will eliminate ISM. Alternatively, a self-weight compliance constraint is sufficient if a fully-connected structure is the only design requirement beyond the desired objective. The proposed bulk and shear stiffness constraints require at least some stiffness in all directions. Thus, the isotropic constraints may not be necessary unless, of course, some degree of isotropy is required. There was no discernible difference between the three studied isotropy constraints, although the ease of differentiating and implementing the universal or log-universal isotropy constraints give them a slight advantage over the log-distance constraint.

CHAPTER 4: ADDITIVE MANUFACTURING OF BANDGAP STRUCTURES

The rise of additive manufacturing (AM) has considerably opened the design space for engineering applications. Notably, AM is an excellent choice to produce bandgap structures due to their complexity and proclivity for rounded features. This chapter describes initial work related to manufacturing and testing bandgap structures using resources available at Lawrence Livermore National Laboratory (LLNL).

4.1 Photonic bandgap validation

It would be very useful to experimentally validate the photonic bandgap performance predicted by the simulations in Chapter 2. Thus, initial work was performed to prepare for future bandgap validation experiments. Namely, the unit cell size and material selection was considered. As previously noted, the bandgap-midgap ratio is preferred as an objective function in design optimization so that the unit cell can be scaled without changing the performance of the photonic crystal. The first step in setting up a bandgap validation experiment is choosing the unit cell so that the bandgap occurs at a frequency that can be measured by the available experimental equipment. Then, a constituent material must be selected which exhibits a bandgap for the proposed unit cell design. A final consideration when designing a bandgap validation experiment is the effect of a finite lattice on bandgap performance; we note that simulations assume infinite periodicity.

4.1.1 Experimental design

It is helpful to first understand how the unit cell size of a photonic crystal relates to bandgap frequencies for typical designs. Examine Figure 4.1, which displays the frequency ranges of the electromagnetic spectrum. Additionally, normalized frequency contours $\frac{\omega a}{2\pi c} = \frac{a}{l}$ for $l = \frac{2\pi c}{\omega}$ are plotted at values of 0.1 and 2.0. These values give an approximate range where bandgaps could

lie for photonic crystals, although it should be noted that bandgaps optimized in this work were typically located at normalized frequency values in the range $\frac{a}{\lambda} \in [0.3 - 0.7]$. Nonetheless, we get a picture of the required unit cell size to generate a bandgap structure anywhere along the electromagnetic spectrum. Notably, we see that to create a bandgap for radiowaves the unit cell is on the order of meters, which is clearly possible. However, on the other end of the spectrum, we would need a unit cell on the order of picometers to create a bandgap in the gamma ray regime; this is obviously not possible with modern manufacturing technology. There is great interest in obtaining bandgaps that work in the visible regime, however, this requires sub-micron unit cells which pushes the edge of manufacturing capabilities for 3D structures. In this section, we will consider bandgaps in the microwave regime which require feasible unit cells on the order of millimeters.

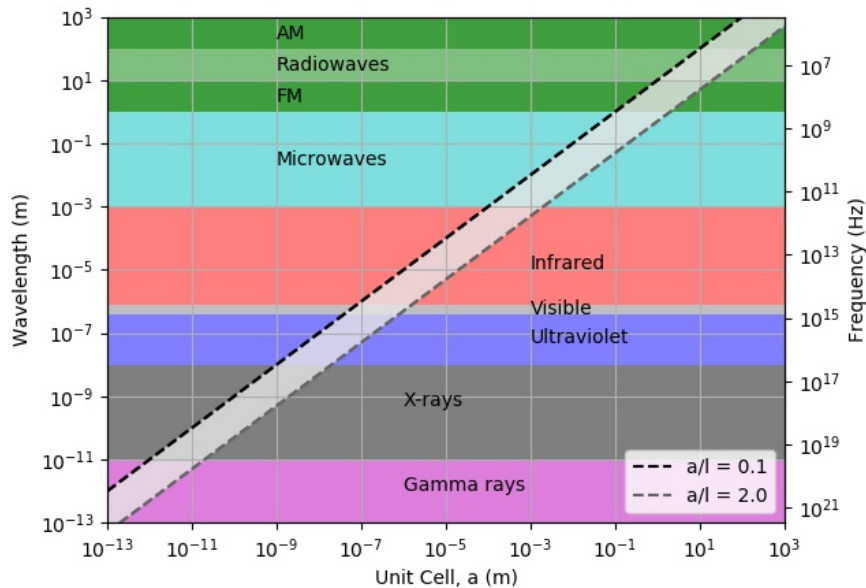


Figure 4.1 Relationship between unit cell size and electromagnetic frequency

Collaborators at LLNL were identified who possessed the equipment to perform bandgap validation tests in the gigahertz (GHz) regime. The 3D bandgap structure in Figure 2.9 was selected for validation and so a normalized frequency scan of $\frac{a}{\lambda} \in [0.3, 0.6]$ was determined to be appropriate. It is straightforward to compute that $\frac{a}{\lambda} \in [0.3, 0.6]$ corresponds to a frequency range $f \in [6, 12]$ GHz for a unit cell size of 15 mm, cf. Figure 3.16 which plots $f = \frac{\omega a}{2\pi c}$. Fortunately, a unit cell size of

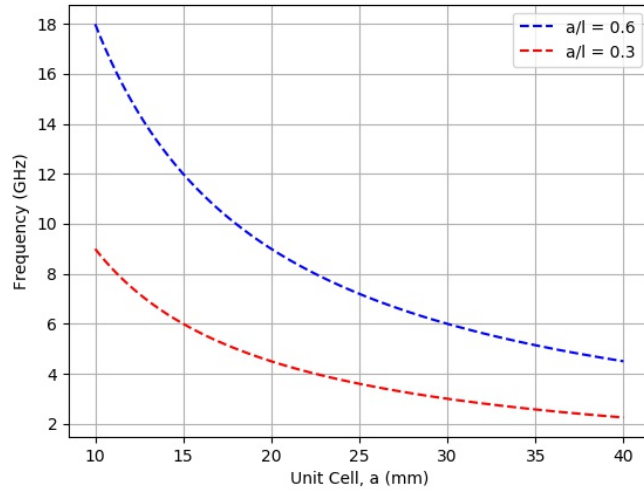


Figure 4.2 Frequency vs. unit cell size

15 mm was appropriate for the selected 3D printer as it could accommodate the feature size of the unit cell while printing an array of 10^3 unit cells. Figure 4.3 presents a screenshot of the 3D printer pre-processing software which pictures the proposed array of unit cells placed on the build tray. The boundary box represents the limits of the build domain. Unfortunately, the additive manufacturing process was not straightforward and the first batch of prints was not successful. The failed specimens are pictured in Figure 4.4. An important lesson learned was that only the top half of the

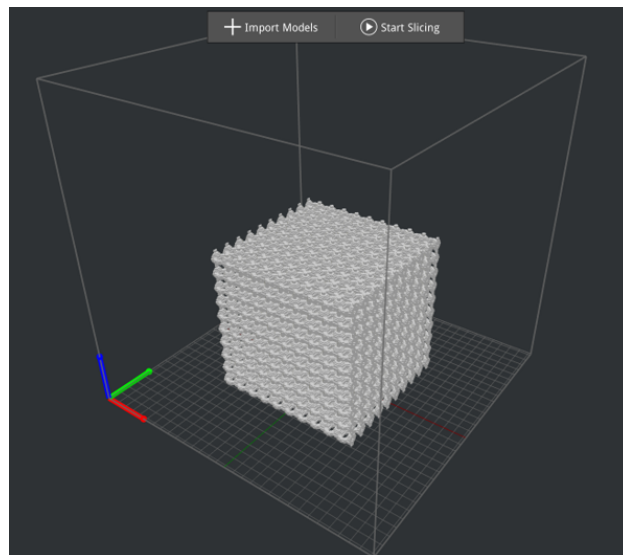


Figure 4.3 3D printing preview of photonic crystal



Figure 4.4 Failed attempt at 3D printing photonic crystals

spheres (relative to the build tray) could be successfully printed using the available printer. Thus, large arrays would have to be manually assembled after printing was completed; this is an arduous process. At the present time, techniques are being developed to better print this structure. The main issue was the printing of materials with a high relative permittivity; this point is expanded upon in the next section.

4.1.2 Material selection

In general, a larger permittivity, ϵ_r , contrast between the solid and void phase allows for a larger bandgap [1]. Unfortunately, there are few widely available 3D printing materials with large permittivity, e.g. $\epsilon_r > 6$. All of the designs in this work were optimized for $\epsilon_r = 13$ based on previous studies [35]. Needless to say, we were unable to find a 3D printer capable of matching this.

A 3D printer at LLNL is able to use commercially produced materials with quoted properties of $\epsilon_r = 6, 8, \text{ or } 10$. It is advantageous to use the highest ϵ_r material possible so that the bandgap is as large as possible, but unfortunately the higher ϵ_r material suffers from poor printing behavior.

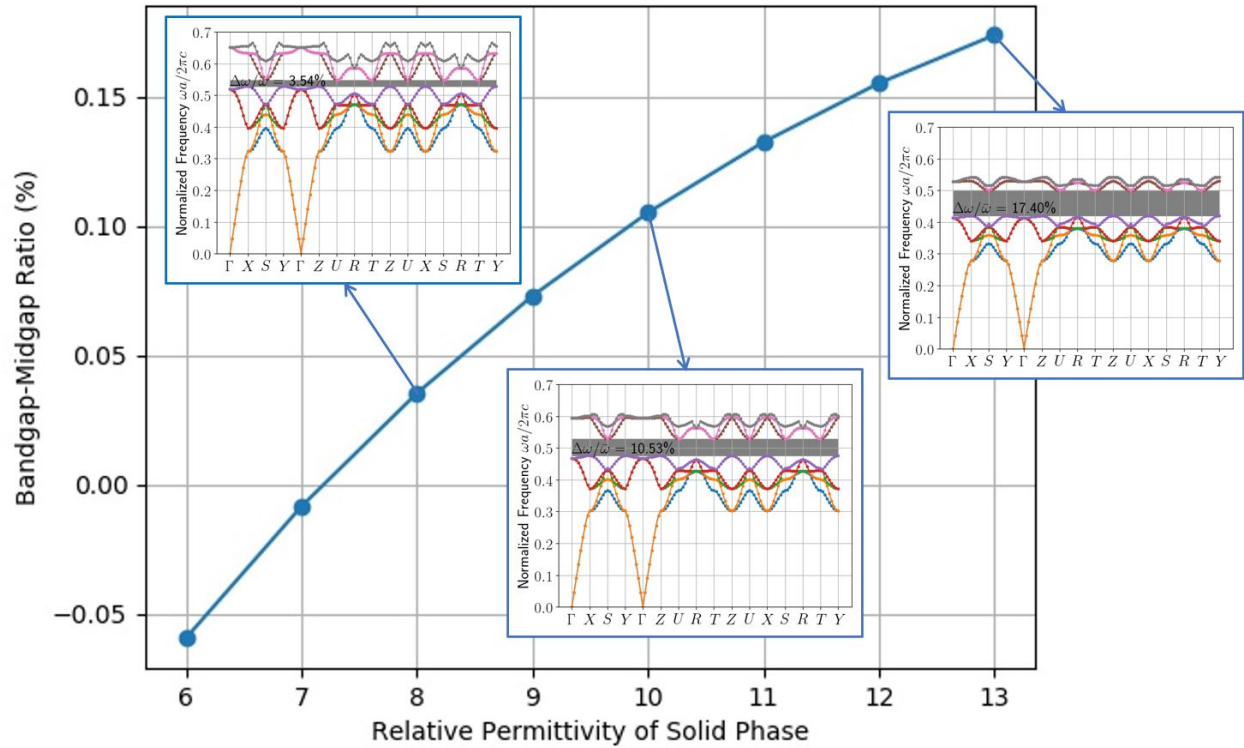


Figure 4.5 Performance of structure from Figure 2.9 vs. ϵ_r of base material

The $\epsilon_r = 10$ material produced very poor quality parts, while the $\epsilon_r = 6$ material produced much higher quality. As expected, $\epsilon_r = 8$ was somewhere in between. We should note that optimal photonic crystal geometry is unique to the value of ϵ_r selected [1], so ideally a crystal should be optimized specifically for the ϵ_r of the constituent material. However, in this case we will not change the geometry so as to reduce simulation time since our main goal is to validate the numerical predictions. Figure 4.5 presents the predicted bandgap-midgap ratio for the design in Figure 2.9 for various values of ϵ_r . We see that any constituent material with $\epsilon_r < 7.2$ will not exhibit a bandgap. Thus, the $\epsilon_r = 8$ printing material is our only viable option. Hopefully, this material can be used to print parts for bandgap validation in the future. Alternatively, further advancement of printing technology or the development of printable materials with larger ϵ_r will aid in this experimental endeavor. The bandgap validation experiments are further addressed in Section 5.1.

4.2 Testing additive manufacturing constraints

The constraints in Chapter 3 were developed to ensure designs are manufacturable. Thus, we aim to test this claim by prototyping our photonic crystals. A few different techniques are used here to highlight the applicability of the proposed virtual temperature method (VTM) constraint. In Chapter 2 we designed a number of bandgap structures. The design from Figure 2.10 will be considered here since it has regions of enclosed void space (EVS). In Chapter 3, we re-visited this design problem by applying the VTM to prohibit enclosed void space. A new design, depicted in Figure 3.18b, was produced with small channels such that the void space became simply connected.

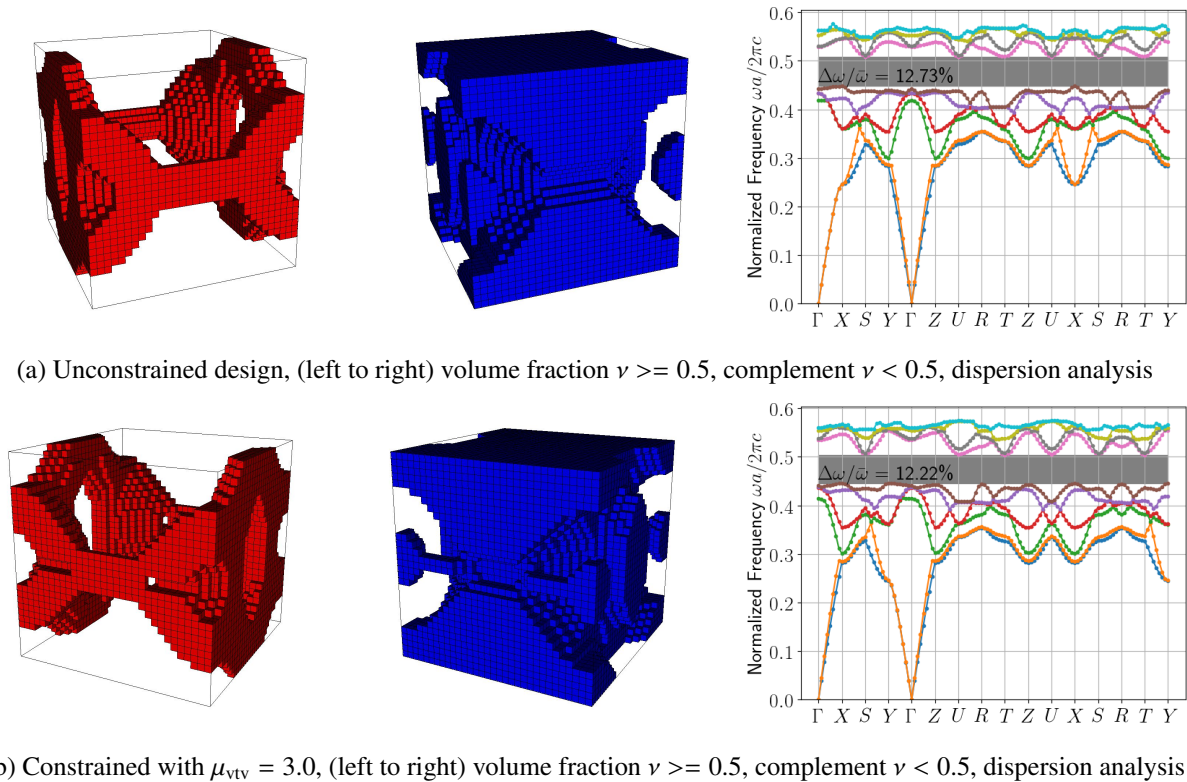


Figure 4.6 Applying θ_{vtv} constraint to remove EVS from mode 6-7 bandgap structure

To ease manufacturing, the VTM was further leveraged by lowering μ_{vtv} and re-solving the optimization problem to maximize the size of the void channels. The results are presented in Figure 4.6; the unconstrained version is presented again in Figure 4.6a whereas the constrained design is presented in Figure 4.6b. It is clear that EVS has been successfully avoided while only

slightly reducing bandgap performance.

An array of 3^3 unit cells was selected to test additive manufacturing techniques [106] on the two designs in Figure 4.6. The corresponding stereolithography (.stl) files are pictured in Figure 4.7. Note that the materials used in this section are not suitable for use in photonic crystals; the intent is only to consider the usefulness of the constraint for removing EVS presented in Chapter 3.

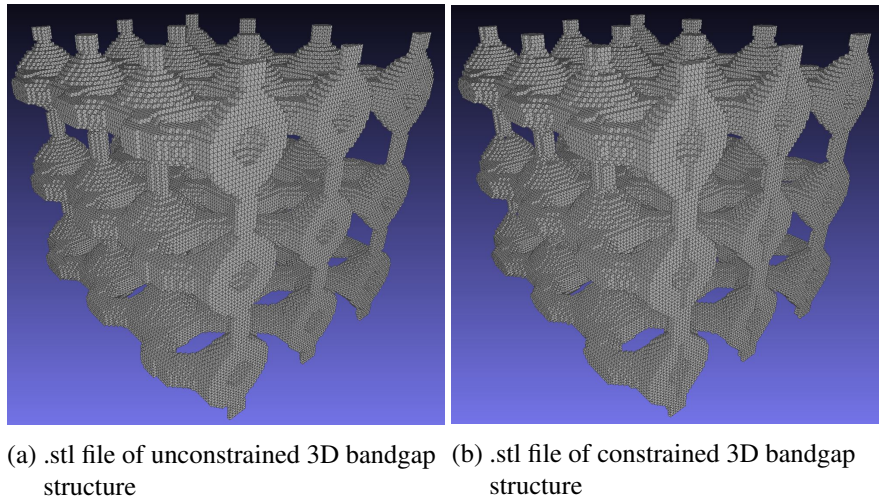


Figure 4.7 .stl files used for 3D printing

4.2.1 Stereolithography

The first 3D printing technique studied was stereolithography (SLA) [106]. As with almost all 3D printing techniques, the design is first sliced into 2D cross sections. Each layer is then built sequentially upon the last layer until the entire prescribed volume has been produced. SLA printers direct light to cure a photo-resin such that each layer is properly solidified to build up the part. The Form 2 printer produced by Formlabs was used to demonstrate this process. The design from Figure 4.6a was 3D printed and the resulting prototype is pictured in Figure 4.8. Although it is difficult to capture in a photograph, careful inspection of the part reveals that un-cured resin was able to escape from the EVS so that the part was manufactured according to the designs. An innovative printing process wherein the light source is placed below the resin bath was the key; since the part rises up out of the liquid bath, all of the un-cured resin can escape the EVS. Thus, the VTM constraint for prohibiting EVS is not required for this SLA printer.

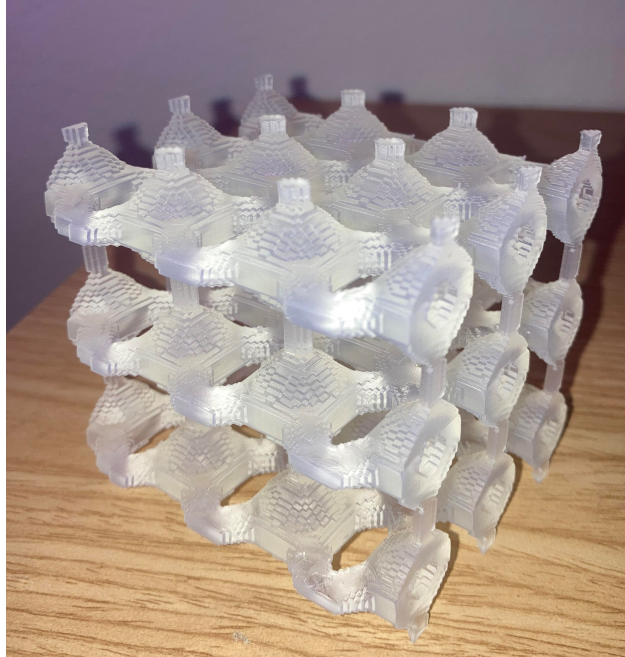


Figure 4.8 Successful 3D bandgap prototype printed with FormLabs SLA machine

4.2.2 Fused deposition modeling

A popular printing method known as fused deposition modeling (FDM) [106] deposits plastic material in a layer by layer process to build 3D parts. The image in Figure 4.9 shows the Prusa i3 MK3S+ printer depositing blue constituent material onto a build tray. A primary concern when using FDM printing is the requirement for support material. Since each layer is placed on top of the previous layers, there must be material underneath to adequately support the features. However, if support material is placed in EVS it will be impossible to remove. We printed the design from Figure 4.6b without support material since it would be almost impossible to remove though the small channels discussed earlier. The resulting prototype is pictured in Figure 4.10. Very poor print quality was observed; plastic strands hung all over the part and many features were damaged or missing. Thus, we can conclude that this part cannot be printed via FDM since it requires support material yet we cannot easily remove it after printing. It is worth noting that some FDM machines use support material that is water soluble and so it may be possible to remove the supports from hard to reach areas by soaking in a water bath. Unfortunately, the printer used here did not have this ability rendering it unable to print our bandgap designs.

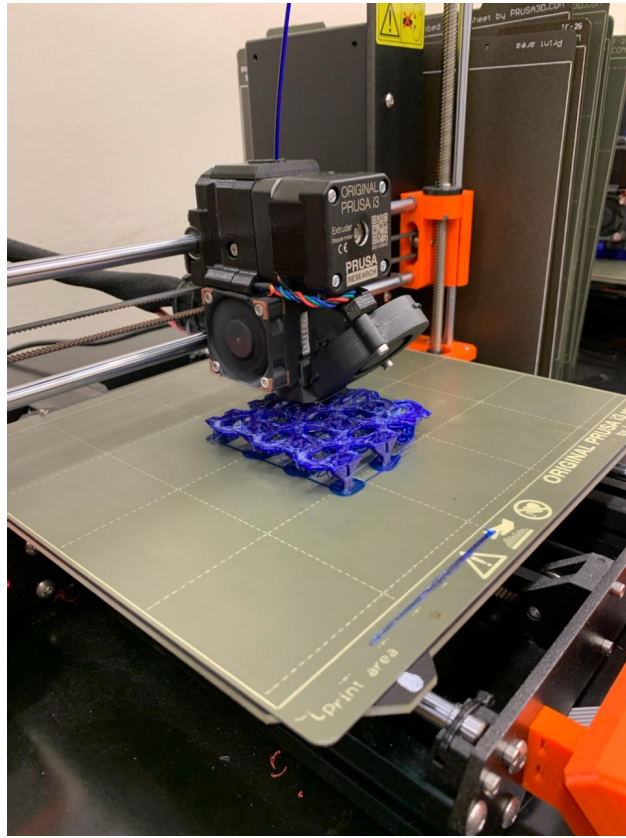


Figure 4.9 FDM 3D Printer

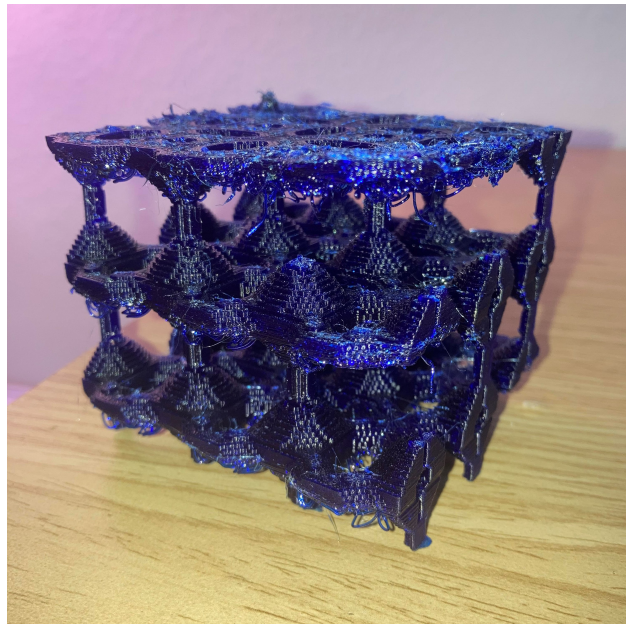
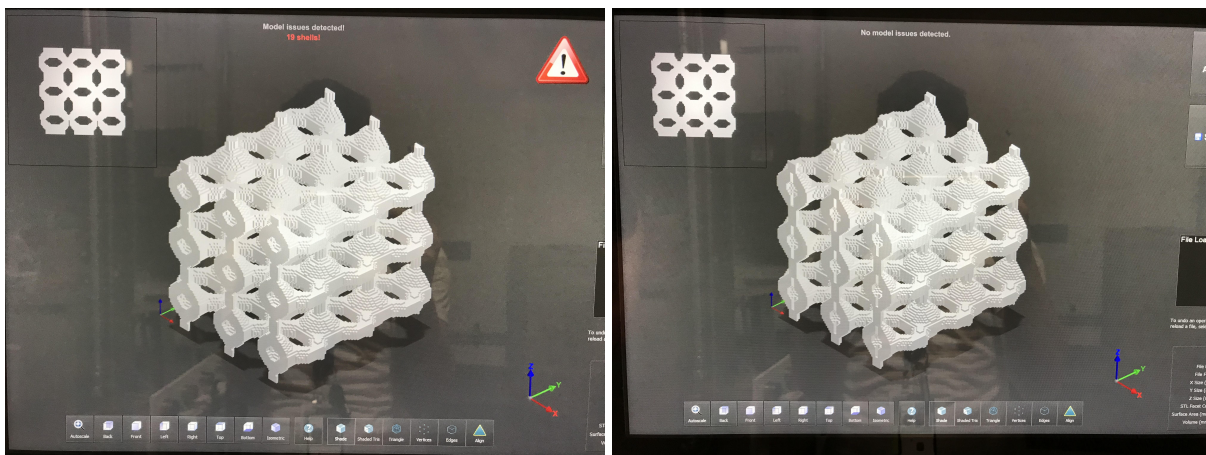


Figure 4.10 Failed 3D bandgap prototype printed with FDM machine

4.2.3 Powder bed fusion

The most successful manufacturing experiment used powder bed fusion (PBF), which is a type of binder printing [106]. This manufacturing technique sequentially builds a 3D part by depositing thin layers of powder and then placing an aqueous binder material such that powder within the prescribed volume of the design is held together, while powder outside the design remains loose. After the powder deposition is completed, the loose powder is carefully removed from the powder that is bound together, i.e. the desired part. At this point the prototype is quite fragile as the powder is only held together by the aqueous binder. The part is then sintered to fully fuse the powder and obtain a final, durable prototype. This printing technique is an excellent application of our VTM constraint to prohibit EVS. Loose powder in EVS will be impossible to remove and will become part of the design upon sintering. Thus, EVS will inadvertently become solid material. We demonstrate this drawback by attempting to print both of the designs in Figure 4.6.

The ExOne M-flex printer was used with 50 micron copper powder to demonstrate PBF printing with and without EVS. First, we loaded the .stl files into the printer software. The screenshots of the pre-processing software in Figure 4.11 immediately warn us of an issue. The image in Figure 4.11a warns us of “shells”, i.e. regions with EVS, when the unconstrained design was loaded, while the image in Figure 4.11b displays no such warning when the constrained design was loaded.



(a) With EVS

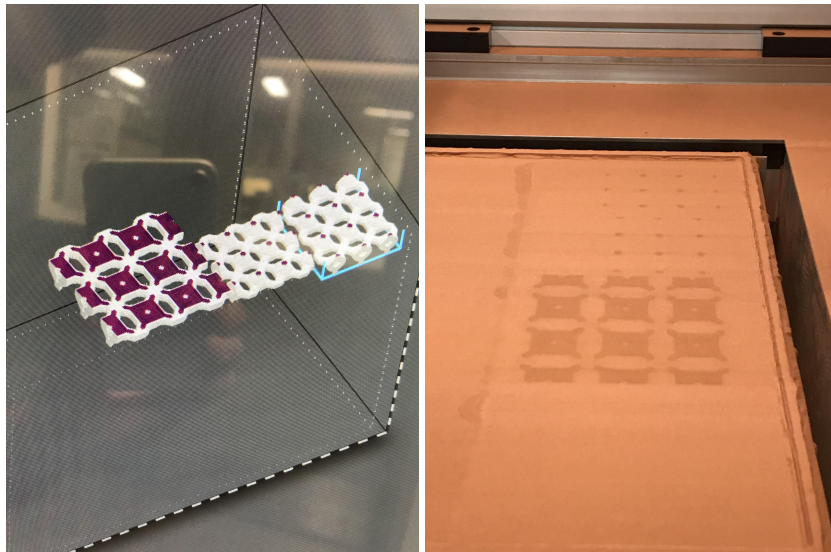
(b) Without EVS

Figure 4.11 Software preview of bandgap designs



Figure 4.12 Bed of copper powder

Before the printing process begins, a bed of powder is carefully placed and leveled as pictured in Figure 4.12. Then, the aqueous binder is placed such that each layer is appropriately held together. An example layer is depicted in Figure 4.13; the digital preview is compared with a photograph of the corresponding layer wherein the location of the binder is apparent. Note that each of the designs in Figure 4.6 were printed at a smaller size in addition to a larger version of the design in Figure 4.6b. After each pass of binder application, a new layer of loose powder is deposited on top so that the next layer can be formed.



(a) Digital preview of design layer (b) Picture of actual design layer

Figure 4.13 Example binder application layer

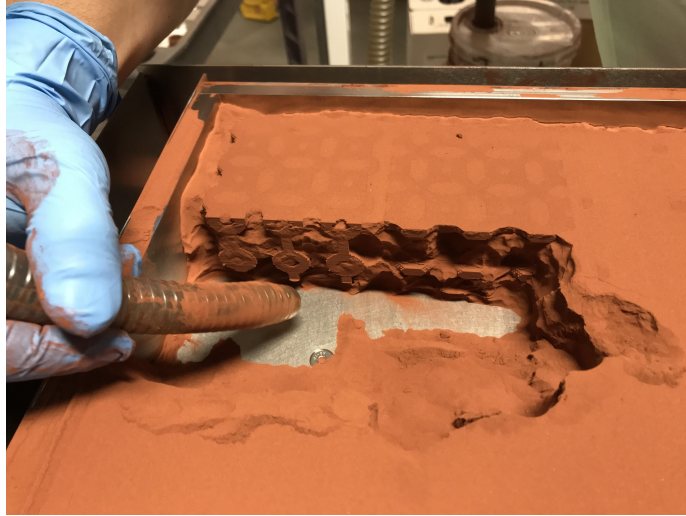
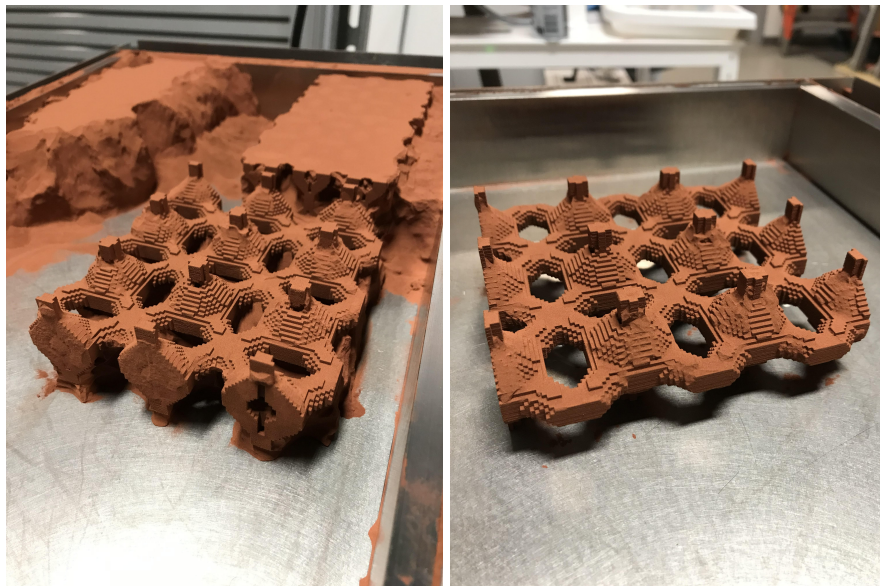


Figure 4.14 Removing loose powder with vacuum

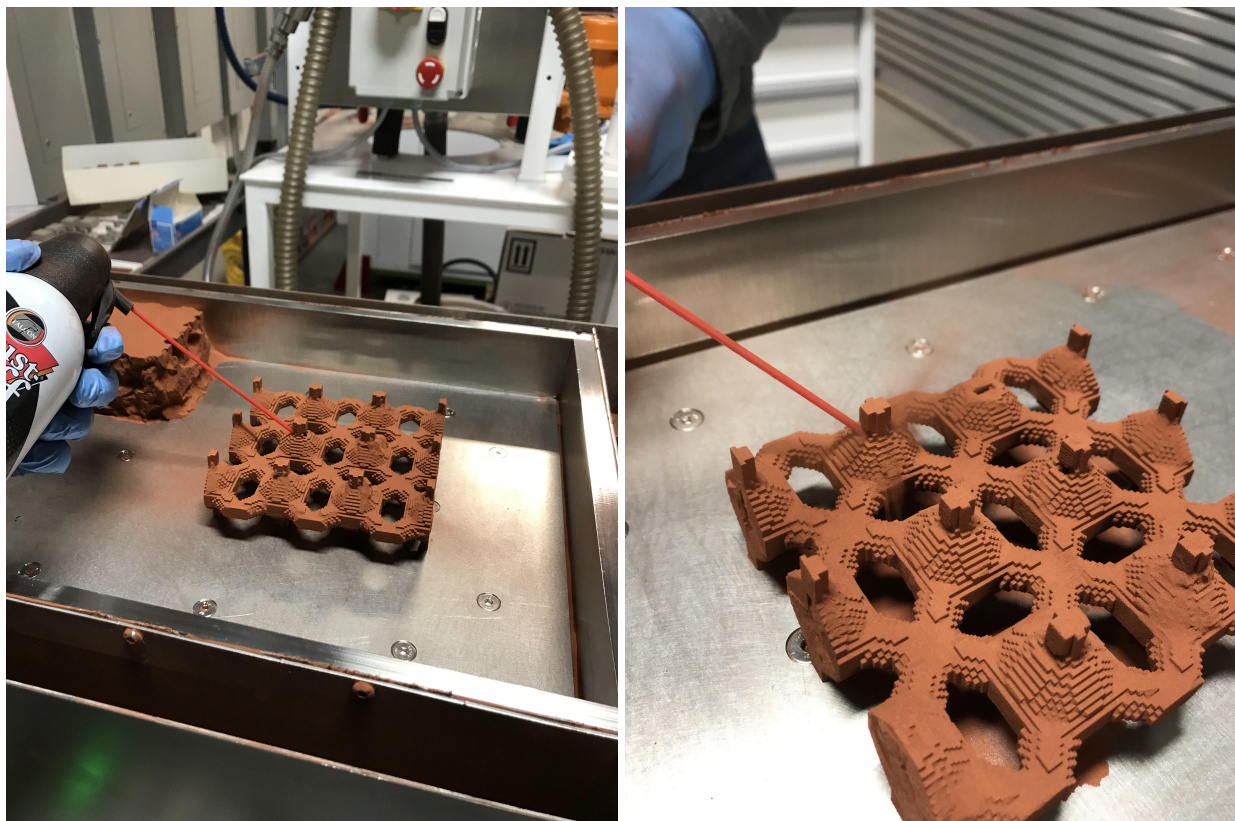
After the binder has been deposited to form each layer of the part, a tedious post-processing task remains. All of the loose powder must be carefully removed from the fragile parts. First, a vacuum is used to remove the majority of the powder, as pictured in Figure 4.14. Then, the vacuum is used more carefully and in unison with a light brush to remove powder from the surface of the prototype. The images in Figure 4.15 show the larger prototype as it is progressively cleaned.



(a) Intermediate condition of part during powder removal (b) Near final condition of part after powder removal

Figure 4.15 Snapshots of powder removal post-processing

The most relevant step in the manufacturing process occurs after the excess powder has been removed from the exterior of the part. It is clear that any powder located in EVS would be impossible to remove therefore this manufacturing process would fail. However, even small access routes to internal features allow powder removal. As evidence, we used a canister of compressed air to remove powder from the partially enclosed features of our design from Figure 4.6b. Figure 4.16 demonstrates this process wherein pressurized air was used to effectively blow loose powder out of the hard-to-reach areas. In fact, loose powder from inside one of these hard-to-reach void regions can actually be seen flying away in Figure 4.16b, just above and to the right of where the red nozzle meets the prototype. These images demonstrate the ability to remove loose powder from nearly any internal void feature which has an access point such that upon final sintering the desired part is obtained. We can conclude that a VTM constraint for prohibiting EVS can be effectively employed to ensure designs are manufacturable via PBF processes.



(a) Placing nozzle near partially enclosed feature (b) Loose powder ejecting from partially enclosed feature

Figure 4.16 Removing powder with pressurized air

CHAPTER 5: CONCLUSIONS

Topology optimization serves as an effective tool for the design of photonic crystals with complete bandgaps. These periodic structures are highly sought after due to their exciting applications including sharp-corner waveguides, fiber optics, antennas, and other optical devices. Most studies in the past, however, struggled to overcome the large computational burden and objective function non-smoothness caused by degenerate eigenmodes. Further, the few previously proposed techniques that were capable of generating 3D bandgap structures were not able to use standard gradient-based nonlinear programming algorithms, limiting their portability.

The planewave expansion technique was used to efficiently compute the required dispersion analysis to numerically predict photonic bandgaps. An iterative eigenvalue solver is crucial for bandgap optimization, since the number of degrees of freedom is very large, yet only the smallest few eigenvalues are required. A popular method from the literature was employed here which leveraged an efficient matrix-free, iterative eigenvalue solver.

A novel design framework is presented that is capable of efficiently generating 3D microstructures of photonic crystals with complete 3D bandgaps. The key contributions of this work to the bandgap engineering field include the objective smoothing via p -norm approximation, efficient sensitivity analysis for locally-supported design variables, and a successive mesh refinement strategy. The p -norm smoothing allows traditional gradient-based nonlinear programming algorithms to be utilized, which is crucial when adding further design constraints, e.g. manufacturing constraints. The sensitivity analysis makes it feasible to use the classical “density” method for topology optimization which offers immense design flexibility. Finally, the mesh refinement strategy greatly relieved the computational burden by performing early iterations of the design process on a very coarse grid and only refining the small-scale features on the finer grids.

The framework was tested on the design of crystals with complete 2D bandgap, i.e. structures

with total reflection for waves with an angle of incidence limited to a particular plane. The first 8 possible mode pairs were split to form complete bandgaps, demonstrating a robustness of the method to converge to bandgap structures under many different conditions. More importantly, the framework was able to generate 3 structures with complete 3D bandgaps. A previous result from the literature was reproduced lending confidence to the proposed design technique, and a novel photonic crystal was presented as well.

It was observed, in this work and in previous literature studies, that structures with photonic bandgaps often exhibit poor stiffness. In some cases the designs cannot be physically realized due to “islands” of material floating in void space. A series of design constraints were formulated and studied to improve the stiffness properties of photonic crystals and ensure their manufacturability.

The virtual temperature method was presented in the literature as a physics-based constraint capable of identifying regions of enclosed void space, which are problematic for manufacturing. This work extended the virtual temperature method to periodic structures by ensuring that consistent behavior would be achieved regardless of the unit cell’s periodic shift. Further, the method was used with alternative material interpolation schemes to identify “islands” of solid material. A disadvantage was that self-supported structures were not guaranteed. Additionally, a mechanical eigenvalue constraint was developed to identify unsupported material by considering the fourth-smallest eigenvalue. This constraint was effective at identify regions of unsupported material in general, however, an important counter-example arose when a microstructure which was simply connected within the unit cell satisfied the constraint but was not self-supporting. The pitfalls of the virtual temperature method and mechanical eigenvalue constraints were alleviated with the self-weight compliance constraint. Computing the compliance resulting from design-dependent gravity loads acting in all dimensions easily identified unsupported structures due to their large increase in resulting displacement.

The abilities and limitations of the proposed physics-based design constraints were demonstrated on example unit cell designs. Additionally, a simple void-producing or island-producing objective function served as a test problem to investigate appropriate constraint limits. It was de-

terminated from this test problem that a modified linear material interpolation scheme was required for problems with design-dependent loads, e.g. heat source or self-weight. Originally formulated to handle spurious eigenvalue solutions caused by low-density elements in topology optimization, this low-density penalizing interpolation proved invaluable for optimizations using the virtual temperature method, mechanical eigenvalue, or self-weight compliance constraints.

The proposed design constraints were applied to photonic bandgap optimization to ensure that the photonic crystals were manufacturable. The virtual temperature method was employed to remove enclosed void space from two designs with complete 3D bandgaps. Further, the virtual temperature method, mechanical eigenvalue, and self-weight compliance constraints were used to redesign crystals with complete 2D bandgaps to ensure they were self-supporting and therefore physically realizable. Design performance was generally decreased only slightly, and in some cases it actually increased when design constraints were introduced.

In addition to the manufacturing constraints, a series of effective property constraints were also considered. Linear homogenization theory was utilized to compute the effective constitutive tensor so that the periodic microstructures could be modeled as a homogeneous material. Adding design constraints of minimum bulk or shear modulus ensured that structures could support external loads. As evidence, 2D bandgap structures were generated with bulk and shear stiffness in all directions. To show the constraint abilities in tandem, the virtual temperature method was then added in such that photonic crystals were designed with effective stiffness while avoiding any enclosed void space. Finally, The trade-off between bulk stiffness and photonic bandgap was investigated by solving a series of optimization problems with progressively larger minimum bulk moduli requirement. The optimal designs for each constraint were plotted to elucidate the feasible design space when bandgap and bulk stiffness are desired in a periodic structure.

To conclude, a powerful topology optimization technique was developed for the design of photonic crystals with complete bandgaps. Further, a series of physics-based constraints were presented to ensure structures were multi-functional and manufacturable. All of the proposed techniques were successfully demonstrated by designing photonic crystals with complete bandgaps.

5.1 Future work

There is still much work to be done in the bandgap engineering field. This work enabled designers to leverage gradient-based optimization to design photonic crystals. Orthorhombic symmetry was used as a proof of concept, however, this work should be extended to other symmetry groups. For example, many of the largest bandgap structures known to date exhibit diamond symmetry [1]. Additionally, more elegant design parameterizations could increase the efficiency of the design optimization by reducing the number of parameters and better representing the material interface. Early in the research project implicit parameterizations, such as geometric primitives [98] combined with R-functions [107, 108], were investigated, but bandgap structures were unable to be located in the design space. A more general parameterization, such as a shape optimization technique with the ability to nucleate holes [109], might alleviate this issue by allowing the required design flexibility to generate bandgap structures.

Nearly all of the bandgap literature assumes that structures are infinitely periodic. One notable exception [110] did consider the finite lattice effect on density of states, however, much is left to learn. A better understanding of edge effects [1] would help integrate photonic crystals into engineering designs. For example, it is unclear how many unit cells are required to achieve acceptable bandgap performance. Further, the effect of manufacturing defects on bandgap performance is not well understood. These considerations should be studied both experimentally and numerically. Ideally, the finite lattice and manufacturing uncertainties could be modeled in optimizations when designing photonic crystals for specific applications, and the predictions could be validated experimentally. A recent study probed a complete 3D bandgap structure experimentally [111]; this work could serve as a useful guide in future bandgap experiments.

Design process specific constraints should be integrated into the optimization process. The constraints presented in Chapter 3 are a good starting point, but more detailed constraints, such as maximum overhang angle, minimum/maximum solid feature size, and minimum/maximum void feature size should be directly constrained to streamline the design and manufacturing processes.

Funding

This work was performed under the auspices of the U.S. Department of Energy by LLNL under Contract DE-AC52-07NA27344. Funding from the Graduate Research Scholar Program and LDRD number 20-ERD-020 through LLNL is gratefully acknowledged. LLNL-TH-827842.

Research acknowledgements

This project began in earnest during my summer 2019 internship at LLNL when I started working with Dan White and Mark Stowell to continue their work on bandgap optimization. They were both very helpful and their previous write-ups and source code were extremely beneficial. Mark was kind enough to repeatedly meet with me to make sure I understood his previously developed code and explain the necessary bandgap theory. Dan White was a great help learning LLNL tools such as MFEM and Cubit, and he served as my LLNL advisor while I was funded through the Graduate Research Scholars Program. Many other LLNL employees helped me along the way; Cosmin Petra provided great insight into appropriate optimization algorithms, Jun Kudo helped me learn the Livermore computing tools as well as C++, and Seth Watts occasionally listened to me ramble about research questions I was struggling with and provided helpful outside perspective.

Mark Converse was an excellent resource regarding experimental bandgap validation. He was very knowledgeable on the subject and introduced me to Tammy Chang and Abigail Gilmore who started working on the high-permittivity bandgap prints pictured in Figure 4.4.

Cameron Cornell coordinated all of the 3D printing featured in Section 4.2. He provided great insight into the additive manufacturing capabilities at LLNL and produced prototypes very rapidly.

My research advisors, Professors Kai James and Dan Tortorelli, were instrumental to the progress made here. We discussed the project during bi-weekly meetings along with Dan White. This collaboration was crucial to maintaining progress through difficult times. Additionally, the electromagnetics courses I took from Professor Jin before starting this project were imperative to understanding the required theory and numerical techniques.

REFERENCES

- [1] J.D. Joannopoulos, S.G. Johnson, J.N. Winn, and R.D. Meade. *Photonic Crystals: Molding the Flow of Light*. Princeton University, 2 edition, 2008.
- [2] Lord Rayleigh Sec. R. S. Xvii. on the maintenance of vibrations by forces of double frequency, and on the propagation of waves through a medium endowed with a periodic structure. *The London, Edinburgh, and Dublin Philosophical Magazine and Journal of Science*, 24(147):145–159, 1887.
- [3] E. Yablonovitch. Inhibited spontaneous emission in solid-state physics and electronics. *Physical Review Letters*, 58(20):2059–2062, 1987.
- [4] Sajeev John. Strong localization of photons in certain disordered dielectric superlattices. *Physical Review Letters*, 58(23):2486–2489, 1987.
- [5] E. Yablonovitch and T.J. Gmitter. Photonic band structure: the face-centered-cubic case. *Physical Review Letters*, 63(18):1950–1953, 1989.
- [6] E. Yablonovitch. Photonic band-gap structures. *Journal of the Optical Society of America B: Optical Physics*, 10(2):283–295, 1993.
- [7] E. Özbay, A. Abeyta, G. Tuttle, M. Tringides, R. Biswas, C. T. Chan, C. M. Soukoulis, and K. M. Ho. Measurement of a three-dimensional photonic band gap in a crystal structure made of dielectric rods. *Physical Review B*, 50(3):1945–1948, 1994.
- [8] K.M. Ho, C.T. Chan, and C.M. Soukoulis. Existence of a photonic gap in periodic dielectric structures. *Physical Review Letters*, 65(25):3152–3155, 1990.
- [9] J. Smajic, C. Hafner, and D. Erni. Design and optimization of an achromatic photonic crystal bend. *Optics Express*, 11(12):1378–1384, 2003.
- [10] J. Jensen and O. Sigmund. Systematic design of photonic crystal structures using topology optimization: low-loss waveguide bends. *Applied Physics Letters*, 84:2022, 2004.
- [11] Stephanie A. Rinne, Florencio García-Santamaría, and Paul V. Braun. Embedded cavities and waveguides in three-dimensional silicon photonic crystals. *Nature Photonics*, 2(1):52–56, 2008.
- [12] Tzuhsuan Ma, Alexander B. Khanikaev, S. Hossein Mousavi, and Gennady Shvets. Guiding electromagnetic waves around sharp corners: Topologically protected photonic transport in metawaveguides. *Physical Review Letters*, 114(12):127401–1–6, 2015.

- [13] Talabattula Srinivas. Photonic integrated circuits based on photonic bandgap structures. In *13th International Conference on Fiber Optics and Photonics*, page Tu5F.1. Optical Society of America, 2016.
- [14] J.D. Joannopoulos. The almost magical world of photonic crystals. In *1999 IEEE LEOS Annual Meeting Conference Proceedings. LEOS'99. 12th Annual Meeting. IEEE Lasers and Electro-Optics Society 1999 Annual Meeting (Cat. No.99CH37009)*, volume 1, pages 232–233, 1999.
- [15] J.M. Geremia, J. Williams, and H. Mabuchi. Inverse-problem approach to designing photonic crystals for cavity qed experiments. *Physical review. E, Statistical, nonlinear, and soft matter physics*, 66(6 Pt 2):066606, 2002.
- [16] M. B. Dühring, O. Sigmund, and T. Feurer. Design of photonic bandgap fibers by topology optimization. *Journal of the Optical Society of America B: Optical Physics*, 27(1):51–58, 2010.
- [17] G. Allaire. *Shape Optimization by the Homogenization Method*. Springer-Verlag New York, Inc., 2002.
- [18] M.P. Bendsøe and N. Kikuchi. Generating optimal topologies in structural design using a homogenization method. *Computer Methods in Applied Mechanics and Engineering*, 71(2):197–224, 1988.
- [19] M. P. Bendsøe and O. Sigmund. *Topology Optimization: Theory, Methods, and Applications*. Springer, 2 edition, 2004.
- [20] O. Sigmund. Materials with prescribed constitutive parameters: an inverse homogenization problem. *International Journal of Solids and Structures*, 31(17):2313–2329, 1994.
- [21] M. Osanov and J.K. Guest. Topology optimization for architected materials design. *Annual Review of Materials Research*, 46:211–233, 2016.
- [22] Y. Ding, Z. Liu, C. Qiu, and J. Shi. Matamaterial with simultaneously negative bulk modulus and mass density. *Physical Review Letters*, 99(9):093904, 2007.
- [23] K.W. Wojciechowski. Two-dimensional isotropic system with a negative poisson ratio. *Physics Letters A*, 137(1):60 – 64, 1989.
- [24] D.R. Smith, W.J. Padilla, D.c. Vier, S.C. Nemat-Nasser, and S. Schultz. Composite medium with simultaneously negative permeability and permittivity. *Physical Review Letters*, 84(18):4184–4187, 2000.
- [25] D. A. Pawlak. Metamaterials and photonic crystals – potential applications for self-organized eutectic micro- and nanostructures. *Scientia Plena*, 4(1):014801, 2008.
- [26] Martin Burger, Stanley Osher, and Eli Yablonovitch. Inverse problem techniques for the design of photonic crystals. *IEICE Transactions on Electronics*, E87C(3):258–265, 2004.

- [27] A.P. Seyranian, E. Lund, and N. Olhoff. Multiple eigenvalues in structural optimization problems. *Structural Optimization*, 8(4):207–227, 1994.
- [28] Marcel Doosje, Bernhard J. Hoenders, and Jasper Knoester. Photonic bandgap optimization in inverted fcc photonic crystals. *Journal of the Optical Society of America B*, 17(4):600–606, 2000,.
- [29] Steven J. Cox and David C. Dobson. Maximizing band gaps in two-dimensional photonic crystals. *SIAM Journal on Applied Mathematics*, 59(6):2108–2120, 1999.
- [30] Steven J. Cox and David C. Dobson. Band structure optimization of two-dimensional photonic crystals in h-polarization. *Journal of Computational Physics*, 158(2):214 – 224, 2000.
- [31] S.J. Cox. The generalized gradient at a multiple eigenvalue. *Journal of Functional Analysis*, 133(1):30 – 40, 1995.
- [32] C.Y. Kao, S. Osher, and E. Yablonovitch. Maximizing band gaps in two-dimensional photonic crystals using level set methods. *Applied Physics B*, 81(2):235–244, 2005.
- [33] Thomas Felici and Heinz W Engl. On shape optimization of optical waveguides using inverse problem techniques. *Inverse Problems*, 17(4):1141–1162, 2001.
- [34] H. Men, N.C. Nguyen, R.M. Freund, P.A. Parrilo, and J. Peraire. Bandgap optimization of two-dimensional photonic crystals using semidefinite programming and subspace methods. *Journal of Computational Physics*, 229(10):3706–3725, 2010.
- [35] H. Men, K.Y.K. Lee, R.M. Freund, J. Peraire, and S.G. Johnson. Robust topology optimization of three-dimensional photonic-crystal band-gap structures. *Optics Express*, 22(19):22632–22648, 2014.
- [36] O. Sigmund and J.S. Jensen. Systematic design of phononic band-gap materials and structures by topology optimization. *Philosophical Transactions: Mathematical, Physical and Engineering Sciences*, 361(1806):1001–1019, 2003.
- [37] H. Dong, Y. Wang, T. Ma, and X Su. Topology optimization of simultaneous photonic and phononic bandgaps and highly effective phoxonic cavity. *Journal of the Optical Society of America B: Optical Physics*, 31(12):2946–2955, 2014.
- [38] Linfang Shen, Zhuo Ye, and Sailing He. Design of two-dimensional photonic crystals with large absolute band gaps using a genetic algorithm. *Physical Review B*, 68(3):035109, 2003.
- [39] F. Meng, B. Jia, and X. Huang. Topology-optimized 3d photonic structures with maximal omnidirectional bandgaps. *Advanced Theory and Simulations*, 1(12), 2018.
- [40] Ole Sigmund. On the usefulness of non-gradient approaches in topology optimization. *Structural and Multidisciplinary Optimization*, 42:589–596, 2011.

- [41] Ole Sigmund and Kristian Hougaard. Geometric properties of optimal photonic crystals. *Physical Review Letters*, 100(15):153904, 2008.
- [42] S. Li, H. Lin, F. Meng, D. Moss, X. Huang, and V. Jia. On-demand design of tunable complete photonic band gaps based on bloch mode analysis. *Scientific Reports*, 8(1):14283, 2018.
- [43] J. Jensen and O. Sigmund. Topology optimization for nano-photonics. *Laser Photonics Review*, 5(2):308–321, 2011.
- [44] Sean Molesky, Zin Lin, Alexander Y. Piggott, Weiliang Jin, Jelena Vucković, and Alejandro W. Rodriguez. Inverse design in nanophotonics. *Nature Photonics*, 12(11):659–670, 2018.
- [45] I L Lyubchanskii, N N Dadoenkova, M I Lyubchanskii, E A Shapovalov, and Th Rasing. Magnetic photonic crystals. *Journal of Physics D: Applied Physics*, 36(18):R277–R287, 2003.
- [46] V. I. Belotelov and A. K. Zvezdin. Magneto-optical properties of photonic crystals. *J. Opt. Soc. Am. B*, 22(1):286–292, 2005.
- [47] M. Inoue, R. Fujikawa, A. Baryshev, A. Khanikaev, P. B. Lim, H. Uchida, O. Aktsipetrov, A. Fedyanin, T. Murzina, and A. Granovsky. Magnetophotonic crystals. *Journal of Physics D: Applied Physics*, 39(8):R151–R161, 2006.
- [48] Mohammad Nur-E-Alam, Mikhail Vasiliev, and Kamal Alameh. ano-structured magnetic photonic crystals for magneto-optic polarization controllers at the communication-band wavelengths. *Optical and Quantum Electronics*, 41(9):661–669, 2009.
- [49] V.A. Kotov, V.G. Shavrov, M. Vasiliev, K. Alameh, M. Nur-E-Alam, and D.E. Balabanov. Properties of magnetic photonic crystals in the visible spectral region and their performance limitations. *Photonics and Nanostructures - Fundamentals and Applications*, 28:12–19, 2018.
- [50] K. C. Huang, E. Lidorikis, X. Jiang, J. D. Joannopoulos, K. A. Nelson, P. Bienstman, and S. Fan. Nature of lossy bloch states in polaritonic photonic crystals. *Physical Review B - Condensed Matter and Materials Physics*, 69(19):195111–1–195111–10, 2004.
- [51] A. Raman and S. Fan. Photonic band structure of dispersive metamaterials formulated as a hermitian eigenvalue problem. *Physical Review Letters*, 104(8):087401, 2010.
- [52] Jens Gravesen, Anton Evgrafov, and Dang Manh Nguyen. On the sensitivities of multiple eigenvalues. *Structural and Multidisciplinary Optimization*, 44(4):583–587, 2011.
- [53] Frank H. Clarke. *Optimization and Nonsmooth Analysis*. Society for Industrial and Applied Mathematics, 1990.
- [54] U.D. Larsen, O. Sigmund, and S. Bouwsta. Design and fabrication of compliant micromechanisms and structures with negative poisson’s ratio. *Journal of Microelectromechanical Systems*, 6(2):99–106, 1997.

- [55] S. Babae, J. Shim, J.C. Weaver, E.R. Chen, N. Patel, and K. Bertoldi. 3d soft metamaterials with negative poisson's ratio. *Advanced Materials*, 25(36):5044–5049, 2013.
- [56] E. Andreassen, B.S. Lazarov, and O. Sigmund. Design of manufacturable 3d extremal elastic microstructure. *Mechanics of Materials*, 69(1):1–10, 2014.
- [57] O. Sigmund. Tailoring materials with prescribed elastic properties. *Mechanics of Materials*, 20(4):351–368, 1995.
- [58] O. Sigmund. New class of extremal composites. *Journal of the Mechanics and Physics of Solids*, 48(2):397–428, 2000.
- [59] M. Messner. Optimal lattice-structured materials. *Journal of the Mechanics and Physics of Solids*, 96:162–183, 2016.
- [60] O. Sigmund and S. Torquato. Composites with extremal thermal expansion coefficients. *Applied Physics Letters*, 69(21):3203–3205, 1996.
- [61] N. de Kruijf, S. Zhou, Q. Li, and Y.-W. Mai. Topological design of structures and composite materials with multiobjectives. *International Journal of Solids and Structures*, 44(22-23):7092–7109, 2007.
- [62] J. K. Guest and J. H. Prévost. Design of maximum permeability material structures. *Computer Methods in Applied Mechanics and Engineering*, 196(4-6):1006–1017, 2007.
- [63] A. Diaz and Sigmund O. A topology optimization method for design of negative permeability metamaterials. *Structural and Multidisciplinary Optimization*, 41(2):163–177, 2010.
- [64] J.K. Guest and J.H. Prevost. Optimizing multifunctional materials: design of microstructures for maximized stiffness and fluid permeability. *International Journal of Solids and Structures*, 43:028–7047, 2006.
- [65] W. Li, F. Meng, Y. Chen, Y. Li, and X. Huang. Topology optimization of photonic and phononic crystals and metamaterials: A review. *Advanced Theory and Simulations*, 2(7):1900017, 2019.
- [66] Boyan S. Lazarov, Fengwen Wang, and Ole Sigmund. Length scale and manufacturability in density-based topology optimization. *Archive of Applied Mechanics*, 86(1):189–218, 2016.
- [67] János Plocher and Ajit Panesar. Review on design and structural optimisation in additive manufacturing: Towards next-generation lightweight structures. *Materials & Design*, 183:108164, 2019.
- [68] Martin Leary, Luigi Merli, Federico Torti, Maciej Mazur, and Milan Brandt. Optimal topology for additive manufacture: A method for enabling additive manufacture of support-free optimal structures. *Materials & Design*, 63:678–690, 2014.

- [69] A. Gaynor and J.K. Guest. Topology optimization considering overhang constraints: Eliminating sacrificial support material in additive manufacturing through design. *Structural and Multidisciplinary Optimization*, 54(5):1157–1172, 2016.
- [70] X Qian. Undercut and overhang angle control in topology optimization: A density gradient based integral approach. *International Journal for Numerical Methods in Engineering*, 111(3):247–272, 2016.
- [71] G. Allaire, C. Dapogny, R. Estevez, A. Faure, and G. Michailidis. Structural optimization under overhang constraints imposed by additive manufacturing technologies. *Journal of Computational Physics*, 351:295–328, 2017.
- [72] Jikai Liu and Albert C. To. Deposition path planning-integrated structural topology optimization for 3d additive manufacturing subject to self-support constraint. *Computer-Aided Design*, 91:27–45, 2017.
- [73] Kaiqing Zhang, Gengdong Cheng, and Liang Xu. Topology optimization considering overhang constraint in additive manufacturing. *Computers & Structures*, 212:86–100, 2019.
- [74] Shutian Liu, Quhao Li, Wenjiong Chen, Liyong Tong, and Gengdong Cheng. An identification method for enclosed voids restriction in manufacturability design for additive manufacturing structures. *Frontiers of Mechanical Engineering*, 10(2):126–137, 2015.
- [75] Kenneth E. Swartz, Daniel A. White, Daniel A. Tortorelli, and Kai A. James. Topology optimization of 3d photonic crystals with complete bandgaps. *Optics Express*, 29(14):22170–22191, 2021.
- [76] J. Jin. *Theory and Computation of Electromagnetic Fields*. John Wiley & Sons, Inc., 2 edition, 2015.
- [77] F. Bloch. Über die quantenmechanik der elektronen in kristallgittern. *Zeitschrift für Physik*, 52(7):555–600, 1929.
- [78] Peter Kuchment. *Floquet theory for partial differential equations*. Springer, 1993.
- [79] Steven G. Johnson and J. D. Joannopoulos. Block-iterative frequency-domain methods for maxwell’s equations in a planewave basis. *Optics Express*, 8(3):173–190, 2001.
- [80] J. Jin. *The Finite Element Method in Electromagnetics*. John Wiley & Sons, Inc., 3 edition, 2014.
- [81] J.C. Nédélec. Mixed finite elements in \mathbb{R}^3 . *Numerische Mathematik*, 35(3):315–341, 1980.
- [82] Robert Anderson, Julian Andrej, Andrew Barker, Jamie Bramwell, Jean-Sylvain Camier, Jakub Cerveny, Veselin Dobrev, Yohann Dudouit, Aaron Fisher, Tzanio Kolev, Will Pazner, Mark Stowell, Vladimir Tomov, Ido Akkerman, Johann Dahm, David Medina, and Stefano Zampini. Mfem: A modular finite element methods library. *Computers & Mathematics with Applications*, 81:42–74, 2021.

- [83] A.V. Knyazev. Toward the optimal preconditioned eigensolver: locally optimal block preconditioned conjugate gradient method. *SIAM Journal on Scientific Computing*, 23(2):517–541, 2001.
- [84] F. Bloch. Frigo, matteo and johnson, steven g. *Proceedings of the IEEE*, 93(2):216–231, 2005.
- [85] W. Setyawan and S. Curtarolo. High-throughput electronic band structure calculations: challenges and tools. *Computational Materials Science*, 49(2):299–312, 2010.
- [86] Florian Maurin, Claus Claeys, Elke Deckers, and Wim Desmet. Probability that a band-gap extremum is located on the irreducible brillouin-zone contour for the 17 different plane crystallographic lattices. *International Journal of Solids and Structures*, 135:26–36, 2018.
- [87] O. Sigmund and J. Petersson. Numerical instabilities in topology optimization: A survey on procedures dealing with checkerboards, mesh-dependencies and local minima. *Structural optimization*, 16(1):68–75, 1998.
- [88] R. B. Haber, C. S. Jog, and M. P. Bendsøe. A new approach to variable-topology shape design using a constraint on perimeter. *Structural optimization*, 11(1):1–12, 1996.
- [89] J. Petersson and O. Sigmund. Slope constrained topology optimization. *Numerical Methods in Engineering*, 41(8):1417–1434, 1998.
- [90] T. E. Bruns and D.A. Tortorelli. Topology optimization of non-linear elastic structures and compliant mechanisms. *Computer Methods in Applied Mechanics and Engineering*, 190(26-27):3443–3459, 2001.
- [91] M. P. Bendsøe. Optimal shape design as a material distribution problem. *Structural optimization*, 1(4):193–202, 1989.
- [92] M. Stolpe and K. Svanberg. An alternative interpolation scheme for minimum compliance topology optimization. *Structural and Multidisciplinary Optimization*, 22(2):116–124, 2001.
- [93] M. P. Bendsøe and O. Sigmund. Material interpolation schemes in topology optimization. *Archive of Applied Mechanics*, 69(9):635–654, 1999.
- [94] Krister Svanberg. The method of moving asymptotes—a new method for structural optimization. *International Journal for Numerical Methods in Engineering*, 24(2):359–373, 1987.
- [95] A. Wächter and L.T. Biegler. On the implementation of a primal-dual interior point filter line search algorithm for large-scale nonlinear programming. *Mathematical Programming*, 106(1):25–57, 2006.
- [96] Quhao Li, Wenjiong Chen, Shutian Liu, and Liyong Tong. Structural topology optimization considering connectivity constraint. *Structural and Multidisciplinary Optimization*, 54(4):971–984, 2016.

- [97] Jianbin Du and Niels Olhoff. Topological design of freely vibrating continuum structures for maximum values of simple and multiple eigenfrequencies and frequency gaps. *Structural and Multidisciplinary Optimization*, 34(2):91–110, 2007.
- [98] S.E. Watts and D.A. Tortorelli. A geometric projection method for designing three dimensional open lattices with inverse homogenization. *International Journal for Numerical Methods in Engineering*, 112(11):1564–1588, 2017.
- [99] X. Qian. Topology optimization in b-spline space. *Computer Methods in Applied Mechanics and Engineering*, 265:15–35, 2013.
- [100] Seth Watts and Daniel A. Tortorelli. An n -material thresholding method for improving integerness of solutions in topology optimization. *International Journal for Numerical Methods in Engineering*, 108(12), 2016.
- [101] Shivakumar I. Ranganathan and Martin Ostoja-Starzewski. Universal elastic anisotropy index. *Phys. Rev. Lett.*, 101(5):055504, 2008.
- [102] R. Hill. The elastic behaviour of a crystalline aggregate. *Proceedings of the Physical Society Section A*, 65(5):349, 1952.
- [103] Christopher Kube. Elastic anisotropy of crystals. *AIP Advances*, 6:095209, 2016.
- [104] Maher Moakher and Andrew N. Norris. The closest elastic tensor of arbitrary symmetry to an elasticity tensor of lower symmetry. *Journal of Elasticity*, 85(3):215–263, 2006.
- [105] Cristian Barbarosie, Daniel A. Tortorelli, and Seth Watts. On domain symmetry and its use in homogenization. *Computer Methods in Applied Mechanics and Engineering*, 320:1–45, 2017.
- [106] Bharat Bhushan and Matt Caspers. An overview of additive manufacturing (3d printing) for microfabrication. *Microsystem Technologies*, 23(4):1117–1124, 2017.
- [107] Y.D. Fougerolle, A. Gribok, S. Foufou, F. Truchetet, and M.A. Abidi. Boolean operations with implicit and parametric representation of primitives using r-functions. *IEEE Transactions on Visualization and Computer Graphics*, 11(5):529–539, 2005.
- [108] A. Pasko, O. Fryazinov, T. Vilbrandt, P. Fayolle, and V. Adzhiev. Procedural function-based modelling of volumetric microstructures. *Graphical Models*, 73(5):165–181, 2011.
- [109] Jorge L. Barrera, Markus J. Geiss, and Kurt Maute. Hole seeding in level set topology optimization via density fields. *Structural and Multidisciplinary Optimization*, 61(4):1319–1343, 2020.
- [110] Shakeeb Bin Hasan, Allard P. Mosk, Willem L. Vos, and Ad Lagendijk. Finite-size scaling of the density of states in photonic band gap crystals. *Phys. Rev. Lett.*, 120(23):237402, 2018.
- [111] Manashee Adhikary, Ravitej Uppu, Cornelis A. M. Hartevelde, Diana A. Grishina, and Willem L. Vos. Experimental probe of a complete 3d photonic band gap. *Optics Express*, 28(3):2683–2698, 2020.